ROLE OF VISCOPLASTICITY IN DEFORMATION AND IGNITION RESPONSE OF POLYMER BONDED EXPLOSIVES

A Dissertation
Presented to
The Academic Faculty

By

David Barrett Hardin

In Partial Fulfillment
Of the Requirements for the Degree
Doctor of Philosophy in Mechanical Engineering

Georgia Institute of Technology

May, 2015

ROLE OF VISCOPLASTICITY IN DEFORMATION AND IGNITION RESPONSE OF POLYMER BONDED EXPLOSIVES

Approved By:

Dr. Min Zhou, Advisor
School of Mechanical Engineering
Georgia Institute of Technology

Dr. Michael Lindsay
Air Force Research Laboratory
Eglin Air Force Base

Dr. Julian J. Rimoli
School of Aerospace Engineering
Georgia Institute of Technology

Dr. Richard Neu
School of Mechanical Engineering
Georgia Institute of Technology

Dr. Naresh Thadhani
School of Materials Science and Engineering
Georgia Institute of Technology

Date Approved: 15 January 2015

ACKNOWLEDGEMENTS

I would like to gratefully acknowledge those without whom this dissertation would not have been completed. First, my family, Kate and Arthur have kept me grounded while in the midst of a seemingly endless journey. My friends and colleagues Matthew and Lauren Priddy have been a constant source of support and shared struggles. I want to thank all of my labmates during my time at Georgia Tech: Ananda Barua, Seokpum Kim, Siddharth Avachat, Chris Lammi, Yan Li, Yifan Gao, and Chris Miller. You all have aided me along the journey with both technical and personal support. I am grateful for the many rotating member of Dr. McDowell’s lab who shared their lab with me during lunch and added greatly to the community at Georgia Tech: Brett Ellis, Jeff Lloyd, and Bill Musinski to name a few. Finally, I want to acknowledge the financial support that I have had throughout my time here, the Defense Threat Reduction Agency, the SMART Scholarship for Service program, and the Air Force Research Lab.

TABLE OF CONTENTS

LIST OF TABLES

LIST OF FIGURES

SUMMARY

The effect of the viscoplasticity of the energetic component (HMX) on the mechanical, thermal, and ignition response of a two-phase (HMX and Estane) polymer bonded explosive (PBX) is analyzed. Specific attention is given to the high strain rate response of the composite during the first passage of a stress wave when impacted by a constant velocity piston. A methodology for computationally generating idealized microstructures with highly-controlled grain volume fraction and particle size distribution is utilized to create specimens with HMX grain fractions ranging from 0.72 to 0.90. The resulting microstructures are analyzed for impact loading from a constant velocity piston traveling at 50 to 200 m/s using a 2D cohesive finite element framework. The computational framework used employs an explicit and fully dynamic cohesive or fracture element framework to explicitly track the fracture and subsequent contact and frictional processes in the material. This framework accounts for finite deformation, thermo-mechanical coupling, semi-arbitrary crack initiation and growth, friction along crack faces, plastic heating, and thermal diffusion.

The initial focus of this work is to fully quantify the effect of the viscoplasticity of the HMX component on the behavior of the overall PBX composite. Results show that, relative to the case with the viscoplasticity turned off, the viscoplasticity of HMX causes a significant reduction in the magnitude of the von Mises equivalent stress and an increase in the hydrostatic stress in the HMX grains. PBX specimens with viscoplastic HMX show significantly less overall heating, lower peak temperatures, and lower numbers of hotspots or fractions of material experiencing localized heating relative to samples without viscoplasticity. This reduction in heating is found to be due to greatly reduced density of fracture sites. Specifically, the density of intragranular fracture, debonding, and binder fracture are significantly reduced.

The ignition sensitivity of the materials is evaluated to determine the effect, if any, of the viscoplasticity of HMX. An ignition threshold derived from chemical kinetics analysis is used to analyze the temperature distributions from the cohesive finite element method (CFEM) simulations and determine the load duration required to generate a hotspot of sufficient size and temperature to initiate a self-sustaining reaction or thermal runaway. For specimens in which ignition occurs, results show that the volume fraction of HMX has no significant effect on the load duration required to cause ignition. The viscoplasticity of HMX, however, is shown to increase the minimum loading duration required for ignition by as much as 25%, depending on the rate of loading. Analysis of the ignition sensitivity across the full range of load intensities yields a critical threshold velocity of 88 m/s required for ignition of a PBX due to a single pass of the stress wave. It is found that the Hugh James relation provides a poor fit for the results of the sensitivity analysis. Possible reasons for this discrepancy are discussed.

Finally, the 2D CFEM framework is also used to study the response of composites with HMX grains in an aluminum binder called aluminum-bonded explosives or ABX. This investigation represents the first effort in the design of a new, novel material system guided by our computational micromechanics framework. The materials basically are formed by replacing the polymer in PBX with aluminum. This investigation focuses on assessing the advantages of such materials over PBX from a mechanical and ignition sensitivity standpoint. The results indicate that replacing the Estane matrix in PBX with an aluminum matrix can decrease the ignition sensitivity of the composite in terms of time required to ignition by as much as 295%.

.

CHAPTER 1: INTRODUCTION

1.1 Motivation

Polymer bonded explosives (PBXs) are a broad class of energetic particulate composites that are used in applications including being the explosive charge in munitions and solid rocket propellants. In general, PBXs are typically composed of two types of components, explosive crystals and a soft binder, although, they can also contain additives such as an oxidizer, like ammonium perchlorate, or an additional fuel source such as aluminum. Due to the nature of these materials, it is of significant concern to formulators to actively minimize the risk of accidental initiation during manufacture, transport, or handling [1].

The binder phase in PBXs serves dual purposes: it provides structural integrity to the composite, and it serves to desensitize the mix as compared to granular energetic material systems. Common binder systems used in PBXs include flouropolymers (e.g., Kel-F), elastomers (e.g.,rubber, Estane, hydroxyl-terminated polybutadiene (HTPB)), flouroelastomers (e.g., Viton), and energetic polymers (e.g., polyglycidyl nitrate, polyvinyl nitrate). The formulator's choice of binder is a complex decision dependent upon the mechanical, thermal, and surface properties [1]. The primary explosive material in PBXs is commonly HMX, RDX, TATB, or PETN and is used in the form of small, hard crystals. Each of these explosive materials have different mechanical properties, sensitivity, and energetic output that must be taken into account during formulation. The bulk mechanical properties of PBXs are significantly influenced by the binder, whose elastic modulus is several orders of magnitude lower than the energetic crystals. This compliance in the binder allows for the binder to carry the majority of the deformation applied to a PBX, increasing the composite's compliance and decreasing the ignition sensitivity.

Over the life of a PBX component, it may be subjected to dynamic loads of up to several GPa applied for durations of nanoseconds to microseconds or more. In order to accommodate these loads, dissipation mechanisms acting on the grain scale lead to energy localization which results in small, intensely heated regions termed hotspots. At sufficient temperatures, these hotspots lead to the onset of highly exothermic chemical reactions. These hotspots are the initiation sites for both burning, called deflagration, and detonation phenomena in PBX composites. The dynamic loading events experienced by PBXs can be either shock or non-shock impact loading events. Significant work has gone into studying the shock initiation of explosive materials. However, initiation and eventual deflagration or detonation can occur in explosive materials even in the absence of shock [2]. Because initiation events occur across such a large spectrum of both shock and non-shock situations, it is crucial that the mechanisms leading to energy localization are well understood at the critical length and time scales for all loading types.

This work shows that plastic deformation in β-HMX particles significantly alters the hotspot evolution and ignition sensitivity in two-phase PBXs at impact velocities between 50 and 200 m/s. A Lagrangian cohesive finite element (CFEM) framework is employed that captures the pertinent dissipation mechanisms at the grain scale. The viscoelastic dissipation in the binder, viscoplastic dissipation in the HMX grains, semi-arbitrary fracture and crack growth in grains and along boundaries, binder tearing, friction, and thermal conduction are explicitly accounted for in the CFEM framework. Simultaneous account for each of these mechanisms provides an avenue for direct delineation of the effect of each mechanism and its influence on the other mechanisms. Specifically, this work is the first effort to couple HMX viscoplasticity with the other pertinent grain-scale dissipation mechanisms.

This work consists of seven main parts, each separated into its own chapter. Chapter 1 lays out the motivation for the current work and outlines the remainder of this dissertation. The remainder of the first chapter is dedicated to summarizing the current state of existing research in the various fields pertaining to the research performed herein.

Chapter 2 is focused on providing a detailed description of the 2D computational framework that is used in Chapters 3, 4, and 6. Included in the complete computational tool are the preprocessors, CFEM framework, and postprocessors. The preprocessors include microstructure generation and finite element meshing techniques used to prepare specimens for the CFEM analysis as well as a description of the microstructures used throughout Chapters 3, 4, and 6. The CFEM framework consists of an explicit numerical time integration scheme, the material models used to represent the various constituents, a description of cohesive finite elements, the contact algorithm, and a description of the loading configuration. The postprocessors discussed detail the methodology for determining the criticality of the individual specimens and the statistical approach used to consider the response of a large number of specimens.

Chapter 3 analyzes and quantifies the effect of HMX viscoplasticity on the mechanical, thermal, dissipative, and damage response of a two-phase PBX. The focus of this chapter is to obtain a thorough understanding of the dynamic material response of PBXs comprised of an Estane binder and HMX grains by isolating and understanding the role of plasticity, fracture, and friction as well as how these mechanisms interact with one another. The CFEM framework is used to predict the response of a systematically varying set of microstructures to loading by piston velocities ranging from 50 to 200 m/s. The mechanical, thermal, dissipative, and damage response of each set and the effect of viscoplastic HMX is extensively quantified as functions of imposed piston velocity, HMX packing fraction, and distance from the piston.

Chapter 4 focuses on the calculation, characterization, and analysis of the ignition and ignition sensitivity response pertaining to the impact loading events discussed in Chapter 3. For each specimen tested at all piston velocities, the temperature field resulting from the CFEM calculations are analyzed to determine if the specimen has ignited. This process involves the application of a chemically-derived criticality condition which acts as a material property of the HMX grains. In this analysis, specimens containing a critical hotspot are said to ignite. The time required to reach criticality is used to quantify the relative sensitivity of specimens that have ignited. The effect of viscoplastic HMX on the relative sensitivity of the PBX specimens is analyzed via a threshold velocity required to cause ignition and by means of two critical energy criteria.

Chapter 5 quantifies the contribution of the inherent anisotropy of the HMX grains to the heterogeneity of the resulting stress and temperature fields in a fully dense HMX polycrystal. Chapters 3 and 4 consider isotropic viscoplasticity in the HMX component of a PBX. This indicates that as the binder phase volume fraction decreases, the calculation containing the isotropic model should become more and more homogeneous in response to loading. However, it is known that HMX is an anisotropic crystalline solid. For high HMX fraction PBX compositions it is therefore advantageous to determine what the potential effect of the crystalline level anisotropy is on the localization response of the crystalline ensemble. Here, a 3D Lagrangian framework is utilized that focuses on the anisotropic crystalline response of HMX by accounting for both monoclinic elasticity and crystalline plasticity and by ignoring phenomena associated with fracture. Acknowledging that this is an idealization, this approach is utilized to systematically quantify the scale and extent of oscillations and localizations in the stress, deformation, and temperature fields in the materials resulting from the anisotropy of material response and microstructure heterogeneity.

Chapter 6 proposes and evaluates a hypothetical energetic composite composed of HMX grains suspended in an aluminum matrix. For convenience, these new composites are termed “aluminum bonded explosives” or “ABX. This investigation focuses not on the feasibility of producing and manufacturing such a composite, but rather on determining whether such an arrangement would be advantageous from a mechanical and ignition sensitivity standpoint. To that end, two ABX formulations are created using different aluminum alloys. The resulting microstructures are examined with the CFEM framework and the results are analyzed for ignition sensitivity. Finally, the increase in ignition sensitivity of the novel ABX formulations is quantified using a critical energy approach.

Finally, Chapter 7 summarizes the major contributions from this work and proposes several avenues for future research extending from the findings presented throughout this thesis.

1.2 Experimental investigation of PBXs

Understanding the mechanical properties and behavior of PBXs has been a topic of major interest to experimentalists for many years, in fact, Williamson et al. [3] has studied the mechanical response of PBX over eleven decades of strain rate and over a range of temperatures. The failure stress was demonstrated to be a monotonic function of strain rate and temperature. The aspect ratio of the specimen was also found to influence the strength of the material, with smaller specimens being stronger due to a high degree of confinement. Depending on the regime of interest, experiments have often been run at strain rates including quasi-static loading [3-9] high rate impact loading [10-16]. Depending on the composition and intensity of the loading, some experiments were able to perform a post-mortem analysis of the failure mechanisms observed during testing. During tests which include an ignition event, however, the pertinent mechanisms are often difficult to detect in situ due to the fast time scale and impossible to analyze afterwards due to explosion or ignition of the material. From the experiments exhibiting ignition behavior, the bulk material response is typically reported as well as the ignition sensitivity.

The quasi-static response of PBX has been studied using a variety of different methods and diagnostic techniques. Palmer and Field [9] studied the failure modes of HMX single crystals using Vickers indentations, finding that at these strain rates twinning leading to cleavage fracture are the dominant failure modes and that plastic deformation plays only a minor role due to the brittle nature of the HMX crystals. Later, Palmer et al. [1] and Rae et al. [6] perform Brazilian tensile tests on HMX based PBXs, finding that debonding of the crystals and cavitation are the primary modes of failure for rubbery elastomer binders. Twinning was seen to cause debonding and is proposed as a potential nucleation site for debonding. Cleavage fracture was seen to be relatively rare in these experiments, occurring only when the crack growth path was impeded. Following on this work, they compare the low strain rate tensile behavior of three different PBX formulations by utilizing pre- and post-failure optical and electron microscopy as well as real-time imaging using an environmental scanning electron microscope. They observed various degrees of debonding related to the size of the particles and binder composition. Wiegand and Reddingius [8] studied various PBX simulants at various confinement and found that as the level of confinement increases, the bulk PBX response transitions from a brittle fracture type response at low confinement to a plastic flow dominated deformation at high confinement pressures. This indicates that confinement pressure may provide for a mechanism shift in the failure mode of PBXs at elevated loading rates and pressures.

The high strain rate regime has probably received the most extensive attention in terms of experimental analysis. Experiments have been run on both single crystals and PBX composites. Dick et al. [16] has shock loaded single crystals of HMX. The wave profiles in the HMX showed characteristics of an elastic-viscoplastic material. This represents a significant change from the quasi-static experiments on single crystals that showed that plasticity did not influence the failure. Concerning plasticity, Menikoff and Sewell [17] calculate that the plastic work required to raise the temperature of HMX only 150 K (much lower than the initiation temperature) corresponds to plastic strains on the order of 1%. This result indicates that while plastic work may not be sufficient to generate hotspots when acting alone, it may still interact with other available dissipative mechanisms to affect the local temperature fields. The experiments on composite PBXs has consistently shown that the viscoelastic binder plays a vital role in the bulk mechanical response of PBXs. At temperatures below the glass transition temperature, the binder behaves as a brittle material, making the composite brittle. At temperatures above the glass transition temperature, the binder behaves as a ductile solid and accommodates significant shear deformation on the behalf of the composite. Gray et al. [11] measured stress-strain profiles for PBX 9501 at a strain rate of 2000 s^{-1} for temperatures ranging from -50 to 50 C. For this composition, the critical failure strain was shown to be independent of temperature and strain rate. However, Govier et al. [14] found that the strain to fracture of EDC37 exhibited significant dependence on temperature at high strain rates. These experiments, highlight the fact that slight variations in PBX composition can have significant effect on the mechanical response. As a result, it is critical that a model be capable of modeling the underlying mechanisms that affects these changes in behavior such as differences in grain morphology and constituent material behavior.

1.3 Numerical examination of PBXs

Numerical studies on the behavior of PBXs has been accomplished by many different researchers using many different approaches. Resnyansky and Gray [18] used a 1D viscoelastic constitutive model to describe the behavior of the bars and specimen in split Hopkinson pressure bar (SHPB) experiments. The authors studied the effect of loading pulse on the response of the specimen. Corley et al. [19] used experimental data from uniaxial compression tests to obtain macroscopic material model parameters. This approach removes the mesoscale effects from the macroscopic model and therefore cannot capture the localization behaviors that drive the mechanical behavior and initiation phenomena in PBXs. Mas et al. [20] introduced the method of cells to provide a means of accounting for the grain scale features in a coarse grained simulation of SHPB tests. It was found that fracture plays a significant role at this scale on the deformation of the PBXs due to large stress gradients between different phases. However, even with this level of grain detail, it is still not possible to isolate specific localization sites due to the interaction of mesostructural organization, friction, and plasticity. Subsequent numerical investigations show an increasing focus on the mesoscale behavior of PBXs. A summary of pertinent numerical studies on the mesoscale can be found here.

1.3.1 Research using Eulerian methods

The Eulerian finite element method (FEM) uses a mesh that is fixed in space and allows the underlying material to flow from one cell to another. This is very convenient when there is extremely large deformation because it removes the potential numerical complications involved in Lagrangian FEM simulations when mesh distortion becomes excessive. The Eulerian FEM framework is also particularly well suited when considering the shock compression of highly heterogeneous materials, like PBXs, where local regions of high deformation can occur due to jetting and pore collapse [21-23]. However, because multiple material phases can be contained by a single computational cell, the material interfaces cannot be explicitly modeled and contact between surfaces requires the use of a mixture theory.

The use of Eulerian codes has advanced the understanding of heterogeneous mesoscale processes in the shock regime by studying melting, void collapse, chemical reactions, and material mixing in high pressure shocks of PBXs and granular composites. Baer et al. [12, 24, 25] study the consolidation, deformation, and reaction of shocked porous HMX using a highly resolved mesh. Hotspots are formed by rapid deformation at material contact points as shock focusing and plastic work near grain boundaries cause significant energy localization as material flows into the intergranular regions. Imbedded chemical reactions cause multiple wave structures to be observed due to particle distribution effects. Benson and Conley [22] perform shock consolidation simulations on experimentally obtained microstructures of granular HMX. The authors found that material viscosity spread out the shock front and reduced the temperature extremes. Hotspots were found to form on particle boundaries and were generated by inelastic deformation due to the compaction of the HMX. Austin et al. [26] use the framework of Benson and Conley to study the shock compression of an aluminum-iron oxide thermite systems where the particles are suspended in an epoxy. Menikoff in [27] uses mesoscale calculations to evaluate the initiation and growth of hotspots and determines how the hotspot distribution can vary as a function of load. In [23], Menikoff studied the generation of hotspots due to the collapse of a single pore due to shock. It was found that shock dissipation alone was not sufficient to initiate the material and that the plastic work and viscous heating were needed as additional dissipation mechanisms. Because dissipation mechanisms scale differently with load intensity, it is essential to accurately model all salient mechanisms in order to predict initiation behavior over a range of stimuli. Eulerian codes can effectively model the propagation of shock and the hydrodynamic behavior of the rapidly deforming material, but they are limited by the inability to explicitly track fracture and contact between grains and along interfaces.

1.3.2 Research using Lagrangian methods

The Lagrangian FEM useds a mesh whose nodes and elements move with the material upon deformation. This imposes practical limits on the use of Lagrangian finite elements in the presence of very high deformation without needing to remap the nodes to form suitably shaped elements. Because the mesh explicitly defines the material, this method is very well suited to modeling the effect of material heterogeneities as well as fracture [28, 29], contact, and friction, which have been suggested as significant mechanisms in the mechanical response and leading to the initiation of PBXs.

Research using this type of FEM, frequently focuses on the interactions between adjacent grains and the behavior and influence of the interfaces between grain and binder. Banerjee [30] simulated circular soda lime glass beads embedded in a polymer matrix under both quasi-static and high strain rate loading. The importance of interfacial bonding on the bulk mechanical properties of the composite were demonstrated. With an increase in debonded particles, there is a significant decrease in the effective young's modulus of the material. The authors compare the debonded particles to put forward that pre-existing damage will have an analogous effect on PBXs. Wu and Huang [31] modeled a PBX by employing a viscoelastic cohesive zone model for the binder. They have simulated a Brazilian compression test and have compared their results concerning debonding and cracking in the PBX with the experimental results of Gray et al. [11]. Panchadhara and Gonthier [32] model wave compaction in granular HMX. This work focuses on the partitioning of dissipation between the surface dominated intergranular friction and bulk viscoplastic dissipation in the HMX particles. Plasticity was found to be a non-critical heat source and intergranular friction was found to be the source of intensely heated hotspots. In addition to traditional Lagrangian applications, Barton et al. [33] has implemented an arbitrary Lagrangian-Eulerian finite element code to simulate the strain localization behavior of HMX single crystals. Specifically, Barton evaluates the heating and melting of HMX due to pore collapse under shock loading according to crystalline slip mechanics. By utilizing Lagrangian frameworks, researchers have been able to investigate the influence of interfaces and grain-grain interactions on the bulk mechanical properties and energy localization behavior of PBXs and granular HMX ensembles.

1.4 Initiation of critical thermal events (hotspots)

The process of localizing energy into small, intensely heated regions termed hotspots is a crucial aspect in the failure of energetic composites such as PBXs. It is these hotspots which will initiate chemical reactions and can potentially transition into a deflagration wave or a full detonation of the material. There has been significant work done with the specific goal of identifying the local threshold conditions which will indicate that a material will transition from initial chemical reactions to a “thermal runaway” condition [34-38]. Thermal runaway means that there is sufficient energy in a hotspot to induce exothermic reactions generating more heat than thermal conduction can draw away from the hotspot.

The seminal work in developing an ignition threshold is by Semenov [35]. This criticality model was a solution to the heat diffusion equation in which chemical reactions directly informed the heat generation term. One major limitation to this model is that the hotspot temperature being considered must not vary over the area of the hotspot. This limitation was removed by the work of Frank-Kamenetskii [36], whose model also deals with the solution to the diffusion equation but allows for temperature variation in the region of interest. Later, Thomas [37] combined key elements of both the Semenov [35] and Frank-Kamenetskii [36] models into a unified model. In addition to ignition thresholds that are based solely on thermal diffusion, there are also a class of thresholds that are derived directly from the specific chemical kinetics effecting HMX. Both Tarver et al. [38] and Henson [34] , have proposed such models. Each utilizes a different three-step chemical kinetics calculation to determine the critical size and ignition time of hotspots as a function of temperature for spherical hotspots. Tarver also considers hotspots with other geometries such as planar and cylindrical hotspots for both HMX and TATB. These ignition thresholds provide a mechanism for inert meso-mechanical simulations to link physically based mechanical sources of energy localization to chemical ignition phenomena.

1.5 Assessment of Ignition Sensitivity

Energetic materials are frequently tested in a variety of methods to determine the conditions necessary for ignition or, contrastingly, the safe operation of the explosive. As data began to amass concerning the apparent threshold that exists between flyer impacts which lead to ignition of the explosive and events that do not, Walker and Wasley [15] proposed a threshold criterion based upon the concept of critical energy (E_c). The theory is built upon the idea that for a given explosive, there exists a critical input energy above which ignition will occur, regardless of the load duration or intensity. Longueville et al. [13] examine six explosive formulations using the Walker and Wasley criterion and found that only one always obeyed the criterion while three showed no adherence to the criterion and the other two formulations obeyed the criterion only over a limited pressure range. Experiments by Honodel et al. [39] on a wide range of TATB formulations using both thin flyer tests and gap tests indicate that the criterion is obeyed only over a limited pressure range. While initially the criterion was applicable only to the flyer impact experiments for which it was designed, the criterion was subsequently modified to accommodate impact by flat-noded rods [40], spherical impactors [2], shaped charge jets [41], and rod impacts with thin barriers [42]. In order to further extend the range of applicability of the critical energy criterion, James [11] proposes a modification to the criterion such that for high velocity impacts the data asymptotes to a constant value equal to the critical energy, and for low velocity impacts, the data asymptotes to a constant value of $\Sigma = {u^2}/{2}$, where *u* is the particle velocity. Using this modified criterion (referred to as the H-J relation), five of the six explosive formulations studied by Longueville et al. [13] correlate where only one showed agreement with the original criterion of Walker and Wasley. Recent work by Welle et al. [43] has successfully modified the H-J criterion to incorporate the microstructural characteristics of granular beds of pressed explosive powders.

CHAPTER 2: 2D COMPUTATIONAL FRAMEWORK

A 2D computational micromechanics framework, referred to as CODEX, is adopted in order to investigate the role of the mesostructure on the mechanical and thermal response of PBXs and their ignition sensitivity. The framework consists of three (3) parts: (1) a microstructure generation preprocessor, (2) a 2D Lagrangian cohesive finite element analysis program, and (3) a series of postprocessing techniques to determine the criticality of individual hotspots and the ignition sensitivity of sets of specimens. The formulation and theory behind the three parts are detailed in this chapter.

2.1 Preprocessors: Microstructure Creation

The microstructure of a PBX (or granular HMX) specimen is highly heterogeneous, irregular, and difficult to represent numerically. The HMX phase of the microstructure is typically present as a multi-modal (2+) grain size distribution spanning two orders of magnitude in diameter from 5 to 234 microns [44]. Because of the large disparity in grain sizes present in real PBX specimens, it is computationally difficult to sufficiently resolve HMX grains over the entire spectrum of grain sizes. Therefore, the PBX microstructures generated and analyzed consider only the largest grain size mode from the distribution. This effectively assumes that the grains smaller than those explicitly resolved are diffused throughout the binder (making the binder itself a composite material) and do not contribute to the mechanical behavior of the composite.

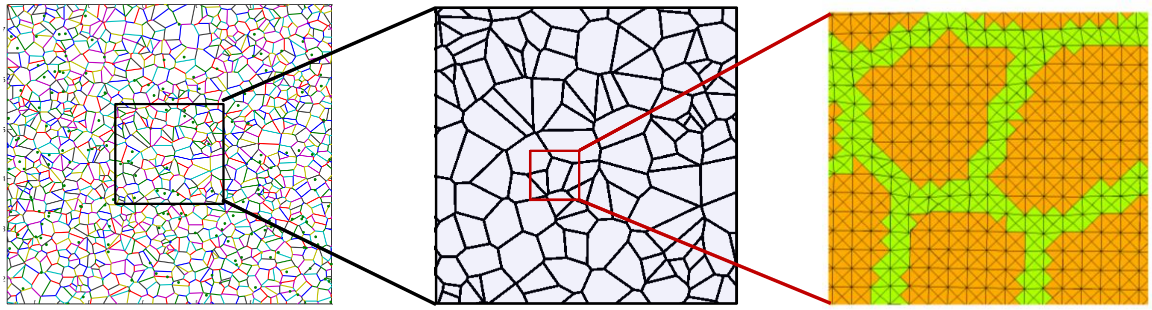

Figure 1. Methodology for microstructure and mesh generation.

Each microstructure is generated using a consistent methodology. Figure 1 is a step-by-step schematic of the processes employed. First (left), a Voronoi tessellation is created from randomly generated seeds within a large 2-dimensional box. The number of seeds in the box is chosen to control the mean grain size. According to the necessary dimensions of the microstructure, a region is chosen from the box that contains only Voronoi cells that are on the interior of the box. Next (center) the edges of each Voronoi cell are expanded to finite width and are identified as the binder phase of the PBX. This two-phase PBX is then converted into a regularly structured finite element mesh (right) utilizing a crossed triangle element arrangement to prevent volumetric locking in the event of deformation in the fully plastic regime [45]. Because the computational framework employs continuously distributed cohesive elements to explicitly account for damage, cohesive finite elements are then placed along every shared finite element edge. This general scheme is used for all of the 2D analysis found in Chapters 3, 4, and 6.

Creation of microstructures in this manner leads to several identifying characteristics present in each specimen. In terms of grain size, this method allows for the generation of microstructures having a monomodal Gaussian distribution around a well-controlled mean grain size. Because the binder is created by uniformly increasing the width of the Voronoi cell edges, the binder in the synthetic microstructures forms into a fully connected matrix with a constant binder thickness throughout. Such organization of the binder into equally sized laminas could potentially effect the behavior of the PBX specimens. Identifying and quantifying such an effect is the subject of an ongoing research initiative.

2.1.1 Microstructures Analyzed

In the analysis that follows, microstructural representations of PBX specimens are loaded by a massive, rigid piston. The specimens under consideration are generated to contain a grain area fraction of 0.72, 0.76, 0.81, or 0.90, which corresponds to grain fractions by weight of 0.81, 0.84, 0.87, and 0.94, respectively. For comparison, the commonly used explosive formulation PBX 9501 contains 0.95 by weight of HMX, with the balance being filled with binder. Figure 2 shows an example microstructures generated using the scheme outlined above with HMX packing fractions of 0.72 (top), 0.81 (middle), and 0.90 (bottom).

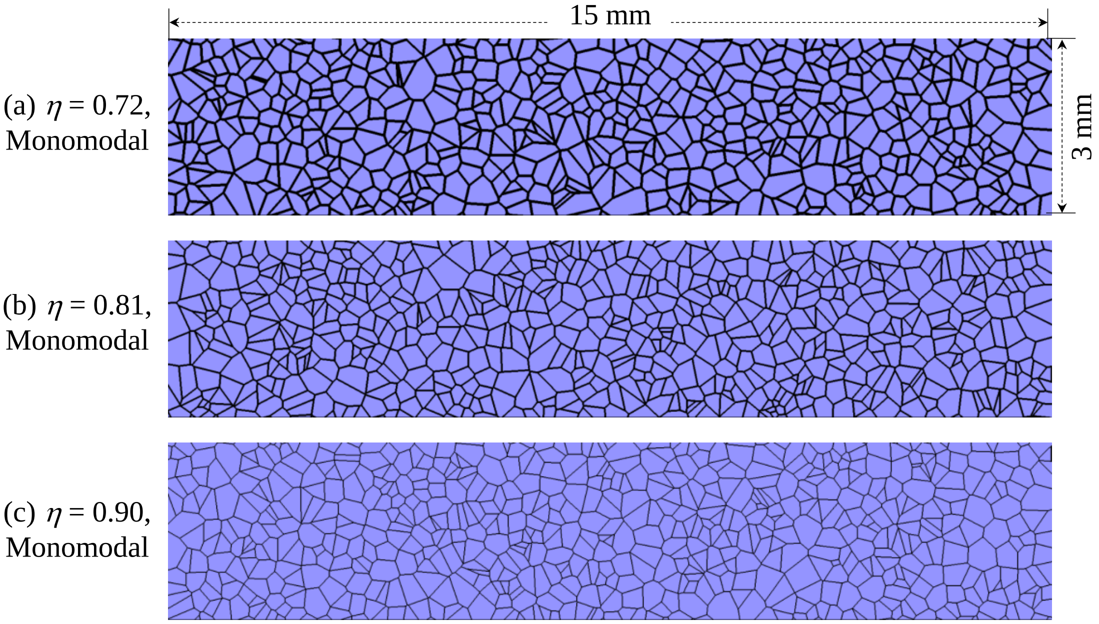

Figure 2. Sample of generated microstructures with HMX packing fractions of (a) 0.72, (b) 0.81, and (c) 0.90, by area.

One benefit of analyzing the behavior of a wide range of PBX specimens computationally is the ability to analyze a number of specimens with well characterized properties under highly controlled loading conditions. To take full advantage of this, twenty microstructural instantiations are generated of each HMX packing fraction to be studied. When generating these microstructure sets, the mean grain size and the total HMX grain fraction are used as control variables. The mean grain size and standard deviation of grain size for each of the microstructure sets is found in Table 1.

Table 1. Microstructural attributes for specimens analyzed in Chapters 3, 4, and 6.

HMX packing fraction (η)	Mean grain size (μm)	Standard deviation (μm)
0.72	235.1	87.4
0.76	241.8	88.6
0.81	250.1	90
0.9	264.3	92.1

Figure 3 provides the specific information concerning the distribution of total HMX fraction and grain size distribution for each set of microstructures. It is clear that the method used to generate these microstructural ensembles produces microstructures that vary slightly from one specimen to the next. Analyzing Figure 3 also indicates that the method employed produces less variation in HMX packing fraction when the amount of HMX in the specimens increases. For the least dense microstructure set ($\eta = 0.72$), the difference between the most and least dense microstructural instantiations is just less than 0.02. This difference steadily decreases to approximately 0.005 for the microstructures with an HMX packing fraction of 0.90. This difference in the spread of packing fractions within each statistically similar set could be eliminated by producing a very large set of microstructures and then choosing only those microstructures falling within some range of the specified HMX fraction. However, this option could potentially lead to some selection bias within the selected set of microstructures, and the effect of small changes in packing fraction is not a focus of this work.

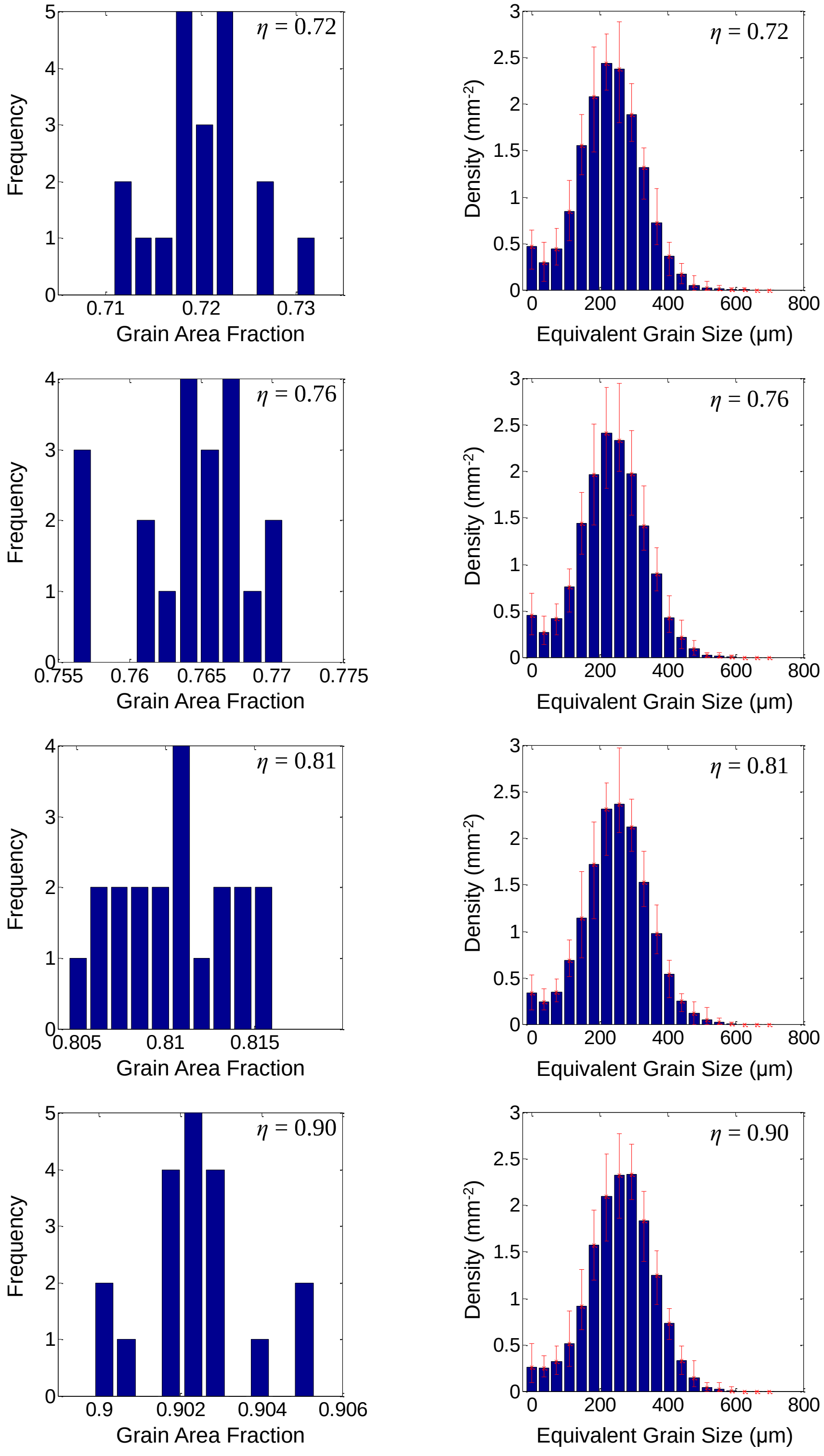

Figure 3. Grain area fraction distribution and associated grain size distribution for each microstructure set.

2.2 Cohesive Finite Element Analysis

The second and most crucial portion of the computational framework is the cohesive finite element method (CFEM). In general, the CFEM is a variation of the finite element method in which cohesive zone elements are distributed throughout the computational domain. Because each cohesive element represents a potential fracture site, crack nucleation and growth within a specimen is limited only by the resolution of the initial finite element mesh. In theory, this limitation could be further reduced by implementing adaptive remeshing to enable fully arbitrary crack propagation. This framework integrates explicit dynamics, large deformation mechanics, coupled thermomechanical behavior of the constituent materials, semi-arbitrary crack nucleation and propagation, thermal conduction, and frictional heating due to the contact between fractured surfaces. The principle parts of the CFEM framework include the governing integration scheme, material models used to describe each constituent, cohesive finite elements, contact algorithm, and the loading configurations applied to the specimens. Each of these parts will be discussed in detail in the sections that follow.

2.2.1 Integration Scheme

The explicit integration scheme presented here incorporates the effects of all of the other portions of the finite element framework to predict the displacement history of every node in the finite element mesh. This section presents an overview of how the various mathematical models in the CFEM framework act together on the global nodal displacements, velocities, and accelerations to model the behavior of dynamically loaded specimens.

The global nodal displacement vector is the variable that controls the motion of each node in the domain and is updated at the beginning of each iteration

$$D_i = D_{i-1} + V_{i-1}\Delta t + \tfrac{1}{2} A_{i-1}\Delta t^2 . \tag{1}$$

Any required displacement boundary conditions are applied directly to D_i. Next, the global nodal force vector is set to zero.

$$F_i = 0 \tag{2}$$

The forces on the nodes due to the bulk and cohesive elements are a functions of only the global nodal displacements. The first contribution to the global nodal force vector each iteration is due to the stress in the bulk finite elements. This stress is calculated according to the material model specified for each element. Each of the models used in CODEX are detailed in subsequent sections. Following the bulk material stress update, the global nodal forces are calculated as a function of stress in each element.

$$F_i = f\left(\sigma^{bulk}\left(D_i\right)\right) \tag{3}$$

Then, using the traction separation law for each unfailed cohesive element, the contribution to the nodal forces due to cohesive elements is added to the force vector using the relation

$$F_i = F_i + F_i^{cohesives} . \tag{4}$$

The nodal accelerations due to the stresses in the bulk and cohesive elements is calculated according to the relation

$$A_i' = -\frac{F_i}{m} . \tag{5}$$

This is an intermediate value used to calculate intermediate values for velocity and displacement in the contact detection, penalty, and friction algorithms. Using these intermediate quantities, all contact sites in the domain are determined using a contact detection algorithm detailed later, in its own section. When a contact site is found, the two surfaces (finite element edges) comprising the contact pair are then sent to the contact algorithm. Within the contact algorithm, the contribution to the nodal accelerations due to contact are split into forces normal (penalty) and tangent (friction) to the contact surface. The fully updated nodal acceleration (A_i) is found by adding the combined contribution to the global nodal acceleration vector due to contact to the intermediate acceleration A_i'.

$$A_i = A_i' + A_i^{contact} \tag{6}$$

Now, A_i contains the contributions from bulk element stress, cohesive element traction, contact, and friction. Finally, the fully updated nodal velocity is calculated.

$$V_i = V_{i-1} + \left[\left(1-\gamma\right) A_{i-1} + \gamma A_i \right] \Delta t \tag{7}$$

In this framework, γ is selected to be 0.5, making this integration scheme the central difference method within the Newmark-β family of methods. Following the velocity update, the time integration step is completed at the beginning of the next time step with the calculation of the nodal displacements.

2.2.2 Material Models

The PBX composition considered in Chapters 3 – 4 is a two-phase microstructure consisting of energetic HMX particles suspended in a soft binder made of Estane. The binder is modelled as a visco-elastic material which is highly sensitive to both temperature and strain rate. The HMX particles are modelled as a hyperelastic, an elastic-viscoplastic, and as an elastic-crystalline plastic material (this material model is described in detail in Chapter 5). The hyperelastic formulation for HMX is used primarily for the purpose of quantifying the effect of elastic-viscoplasticity in the behavior of the composite material. Chapter 6 explores the use of several types of aluminum as a binder material which is also modeled using the viscoplasticity model. The following material models describe the behavior of the solid elements of a given material. In the CFEM framework, each element is bordered on all sides by cohesive elements, discussed in detail later in this chapter.

2.2.2.1 Viscoelastic Model for Estane Binder

Estane 5703 is a commercially available polyester polyurethane elastomer that is manufactured by the B.F. Goodrich Company. It is a binder agent commonly used in PBX formulations. The mechanical behavior of this material is strongly dependent on strain rate and temperature. The model described in detail below utilizes a generalized Maxwell model with a 22-term Prony series to describe the rate dependence of the shear modulus and is coupled to a Williams-Landel-Ferry shift function to account for the temperature dependence of the viscoelastic material [46]. This methodology was developed for Estane by Mas and Clements [46] and implemented into a 2D finite element framework by Barua et al. [47]. In integral form, the general stress-strain response for the Maxwell model in the current configuration is given by

$$\boldsymbol{\sigma}(t)=\int_0^t 2\mathrm{G}(t-t_r)\frac{\partial \boldsymbol{\varepsilon}^D}{\partial t_r}\,dt_r+\int_0^t \mathrm{K}(t-t_r)\frac{\partial \boldsymbol{\varepsilon}^H}{\partial t_r}\,dt, \tag{8}$$

where $\boldsymbol{\sigma}$ is the Cauchy stress, G is the shear modulus, K is the bulk modulus, t and t_r are the physical and reduced times, respectively, $\boldsymbol{\varepsilon}^D$ and $\boldsymbol{\varepsilon}^H$ are the deviatoric and hydrostatic parts of the Eulerian strain tensor. The bulk modulus is assumed to be constant over the regime of interest, as is seen in [31, 46]. The shear modulus varies as a function of the reduced (or relaxation) time t_r' according to a Prony series of the form

$$\mathrm{G}(t_r)=\mathrm{G}_\infty+\sum_{i=1}^{N_p}\mathrm{G}_i e^{-\frac{t_r}{t_{r,i}^p}}=\mathrm{G}_0\left(\mathrm{g}_\infty+\sum_{i=1}^{N_p}\mathrm{g}_i e^{-\frac{t_r}{t_{r,i}^p}}\right), \tag{9}$$

where $\mathrm{G}_0 = \mathrm{G}_\infty + \sum_{i=1}^{\mathrm{N}_p} \mathrm{G}_i$ is the instantaneous shear modulus at the reference temperature T_0, G_∞ is the steady-state shear modulus and, N_P is the number of terms in the Prony series, $\mathrm{g}_i = \mathrm{G}_i / \mathrm{G}_0$ is the relative modulus of the *i*-th term, and $t_{r,i}^p$ are the relaxation times.

The preceding relationships account for the strain rate sensitivity in the viscoelastic formulation. The elastic moduli of a viscoelastic material at a given strain are functions of both time and temperature. A convenient method to describe this dual dependency is to use time-temperature superposition [48]. The time-temperature superposition principle allows for the generation of master curves through the use of a shift factor A_T. This principle states that the stress-strain response at a given temperature can be related to that at another temperature by applying a change in time scale. In other words, a change in temperature at a given strain rate simply shifts the stress-strain curve, it does not affect the shape of the curve. The WLF shift function is one such application of the time-temperature superposition principle and is used in conjunction with the Maxwell model to capture the combined rate and temperature sensitivity of Estane. The reduced time (t_r) is related to the physical time by

$$\mathrm{d}t_r = \frac{\mathrm{d}t}{\mathrm{A}_\mathrm{T}\left(\mathrm{T}(t)\right)}. \tag{10}$$

The WLF shift function specifies the shift factor as a function of temperature as

$$-\log \mathrm{A}_\mathrm{T} = \frac{\mathrm{C}_1\left(T - \mathrm{T}_0\right)}{\mathrm{C}_2\left(T - \mathrm{T}_0\right)}, \tag{11}$$

where, *T* is the temperature, T_0 is the reference temperature, and C_1 and C_2 are fitting constants. The material parameters describing the rate- and temperature-sensitive behavior of Estane including the Prony series, and WLF shift parameters are used directly from [46].

The finite deformation viscoelastic relation presented next mirrors that presented in [49]. The Jaumann rate of Kirchoff stress can be obtained from the rate of deformation (**D)** according to the relation

$$\hat{\boldsymbol{\tau}} = \hat{\boldsymbol{\tau}}^{\mathrm{H}} + \hat{\boldsymbol{\tau}}^{\mathrm{D}} = \mathbf{L} : \mathbf{D}, \tag{12}$$

where, **L** is the isotropic elastic tensor, which for finite strains is

$$\mathbf{L} = \frac{E}{1+\nu}\left[\mathbf{I}' + \frac{\nu}{1-2\nu}\mathbf{I} \otimes \mathbf{I}\right] \tag{13}$$

and $\hat{\boldsymbol{\tau}}^{\mathrm{H}}$ and $\hat{\boldsymbol{\tau}}^{\mathrm{D}}$ are the hydrostatic and deviatoric parts of $\hat{\boldsymbol{\tau}}$, respectively. In addition, $\mathbf{I}'$ is the fourth order identity tensor, $\mathbf{I}$ is the second order identity tensor, and $\mathbf{I} \otimes \mathbf{I}$ indicates the tensor product of two second order identity tensors. Because the relaxation of the shear modulus only acts on the deviatoric part of the stress tensor, $\hat{\boldsymbol{\tau}}$ can be rewritten as

$$\hat{\boldsymbol{\tau}} = \left(1 - \sum_{i=1}^{\mathrm{N_p}} \alpha_i g_i\right)\hat{\boldsymbol{\tau}}^{\mathrm{D}} + \hat{\boldsymbol{\tau}}^{\mathrm{H}}, \tag{14}$$

where $\alpha_i = 1 - \frac{t_{r,i}}{\Delta t_r}\left(1-\gamma_{i)}\right)$, $\gamma_i = e^{\frac{\Delta t_r}{t_{r,i}}}$, and Δt_r is the increment of reduced time, in the current time step. Substituting Equation 12 into 14 gives an expression for the deviatoric part of the Jaumann rate of Kirchhoff stress

$$\hat{\boldsymbol{\tau}}^{\mathrm{D}}_{new} = \left(1 - \sum_{i=1}^{\mathrm{N_p}} \alpha_i \mathrm{g}_i\right) \cdot \left(\mathbf{L} : \mathbf{D}\right)^{\mathrm{D}}. \tag{15}$$

Now, substituting the instantaneous shear modulus (G_0) into Equation 15 gives

$$\hat{\boldsymbol{\tau}}_{new}^{\mathrm{D}} = \left(1 - \sum_{i=1}^{\mathrm{N_p}} \alpha_i \mathrm{g}_i\right) \cdot 2\mathrm{G}_0 \mathbf{D}^{\mathrm{D}} = 2\mathrm{G}_0 \mathbf{D}^{\mathrm{D}} - 2\mathrm{G}_0 \sum_{i=1}^{\mathrm{N_p}} \alpha_i \mathrm{g}_i \mathbf{D}^{\mathrm{D}}. \tag{16}$$

The first term in the expression for $\hat{\boldsymbol{\tau}}_{new}^{\mathrm{D}}$ is the instantaneous shear response and the second term describes the viscous response of the binder. Because the hydrostatic part of the Jaumann rate of Kirchhoff stress is independent of viscous effects, it can be calculated directly from

$$\hat{\boldsymbol{\tau}}^{\mathrm{H}} = \left(\mathbf{L} : \mathbf{D}\right)^{\mathrm{H}}. \tag{17}$$

The viscoelastic dissipation rate is found by evaluating the scalar product of the Kirchhoff stress and the viscoelastic strain rate. As a mechanism contributing to heat generation in the PBX composite, the viscoelastic energy dissipated in this manner is converted to thermal energy in the binder.

2.2.2.2 Hyperelastic Model for HMX

The Saint Venant – Kirchoff hyperelastic model is used to predict the mechanical response of the HMX phase of a PBX under the assumption that the material is undergoing purely elastic large deformations. This model is essentially an extension of a linear elastic finite material model into the nonlinear large deformation regime. The material description begins with a strain energy density *W* of the form

$$W(\mathbf{E}) = \frac{\lambda}{2}\left[\mathrm{tr}\left(\mathbf{E}\right)\right]^2 + \mathrm{G}\,\mathrm{tr}\left(\mathbf{E}^2\right) \tag{18}$$

where, λ is Lame’s constant, G is the shear modulus, and **E** is the Lagrangian strain tensor,

$$\mathbf{E} = \frac{1}{2}\left(\mathbf{F}^T\mathbf{F} - \mathbf{I}\right). \tag{19}$$

Alternately, the strain energy density can be represented in indicial notation by

$$W = \frac{1}{2}\left[\lambda\left(\delta_{ij}\delta_{kl}\right) + 2\mathrm{G}\left(\delta_{ik}\delta_{jl} + \delta_{il}\delta_{jk}\right)\right]\varepsilon_{ij}\varepsilon_{kl}. \tag{20}$$

The second Piola-Kirchhoff stress ($\mathbf{S}$) is found by taking the partial derivative of the strain energy density with respect to $\mathbf{E}$, yielding

$$\mathbf{S} = \frac{\partial \mathrm{W}}{\partial \mathbf{E}} = \lambda \operatorname{tr}\left(\mathbf{E}\right)\mathbf{I} + 2\mathrm{G}\mathbf{E}. \tag{21}$$

The isotropic elastic tensor ($\underline{\underline{\mathbf{C}}}$) is then

$$\underline{\underline{\mathbf{C}}} = \frac{\partial^2 W}{\partial \mathbf{E}^2} = \frac{\partial \mathbf{S}}{\partial \mathbf{E}} = \lambda \mathbf{I} \otimes \mathbf{I} + 2\mathrm{G}\mathbf{I}' \tag{22}$$

and the rate of change in the second Piola-Kirchhoff stress is

$$\dot{\mathbf{S}} = \frac{\partial^2 \mathrm{W}}{\partial \mathbf{E} \partial \mathbf{E}} : \dot{\mathbf{E}} = \underline{\underline{\mathbf{C}}} : \dot{\mathbf{E}}. \tag{23}$$

The parameters required to model the elastic response of HMX have been thoroughly studied in the literature. The elastic parameters used here are adapted from the work of [50] and are summarized alongside the parameters for Estane in Table 2.

Table 2. Material properties for hyperelastic HMX and Estane.

Material Property	HMX	Estane
Young's Modulus	21.2 GPa	N/A
Density	1.91 g/cc	1.19 g/cc
Specific Heat	1254.0 J/kg-K	1500 J/kg-K
Poisson's Ratio	0.277	0.499

2.2.2.3 Isotropic Viscoplastic Model for HMX

The elastic viscoplastic material model is implemented with the purpose of capturing the strain rate and temperature sensitivity of a plastically deforming solid. The particular model presented below has been developed by Zhou [51] and is simply reported here.

For elastic-plastic flow, the basic kinematic assumption is

$$\mathbf{F} = \mathbf{F}^e \cdot \mathbf{F}^p , \tag{24}$$

where $\mathbf{F}^e$ and $\mathbf{F}^p$ are the elastic and plastic portions of the deformation gradient, respectively. The rate of deformation , $\mathbf{D}$, and the spin, $\mathbf{\Omega}$, are the symmetric and anti-symmetric parts of the velocity gradient, $\dot{\mathbf{F}} \cdot \mathbf{F}^{-1}$. The deformation rate and spin can be decomposed into their elastic and plastic parts according to

$$\mathbf{D} = \mathbf{D}^e + \mathbf{D}^p + \mathbf{D}^t, \qquad \mathbf{\Omega} = \mathbf{\Omega}^e + \mathbf{\Omega}^p . \tag{25}$$

At this point, we restrict our attention to the case of small elastic strains, and thermo-elastic coupling is ignored such that the elastic moduli are not dependent on temperature. Under these conditions [52],

$$\hat{\boldsymbol{\tau}} = \mathbf{L} : \left[\mathbf{D} - \mathbf{D^p} \right] , \tag{26}$$

where $\hat{\boldsymbol{\tau}}$ is the Jaumann rate of Kirchhoff stress, $\mathbf{L}$ is the tensor of elastic moduli, α is the thermal expansion coefficient, and T is the temperature. For isotropic elastic response,

$$\mathbf{L} = \frac{E}{1+\nu} \left[\mathbf{I}' + \frac{\nu}{1-2\nu} \mathbf{I} \otimes \mathbf{I} \right], \tag{27}$$

where E is the Young’s modulus, v is Poisson’s ratio, $\mathbf{I}'$ is the fourth order identity tensor, $\mathbf{I}$ is the second order identity tensor, and $\mathbf{A} \otimes \mathbf{B}$ denotes the tensor product.

For an isotropically hardening, viscoplastic solid, $\mathbf{D}^p$ is given by

$$\mathbf{D}^p = \frac{3\dot{\bar{\varepsilon}}}{2\bar{\sigma}}\boldsymbol{\tau}', \tag{28}$$

where $\dot{\bar{\varepsilon}}$ is the equivalent plastic strain rate and

$$\boldsymbol{\tau}' = \boldsymbol{\tau} - \tfrac{1}{3}\left(\boldsymbol{\tau} : \mathbf{I}\right)\mathbf{I}; \qquad \bar{\sigma}^2 = \tfrac{3}{2}\boldsymbol{\tau}' : \boldsymbol{\tau}'. \tag{29}$$

The viscoplastic response of the HMX will be validated against available experimental data and is characterized by the following equations

$$\dot{\bar{\varepsilon}} = \frac{\dot{\varepsilon}_1 \dot{\varepsilon}_2}{\dot{\varepsilon}_1 + \dot{\varepsilon}_2}, \tag{30}$$

$$\dot{\varepsilon}_1 = \dot{\varepsilon}_0 \left[\frac{\bar{\sigma}}{g\left(\bar{\varepsilon}, T\right)}\right]^m, \tag{31}$$

$$\dot{\varepsilon}_2 = \dot{\varepsilon}_m \exp\left[-\frac{a g(\bar{\varepsilon}, T)}{\bar{\sigma}}\right], \tag{32}$$

$$g(\bar{\varepsilon}, T) = \sigma_0 (1 + \bar{\varepsilon}/\varepsilon_0)^N \left\{1 - \beta\left[\left(T/T_0\right)^\kappa - 1\right]\right\}, \tag{33}$$

where $\bar{\varepsilon} = \int_0^t \dot{\bar{\varepsilon}}\, dt$ is the equivalent plastic strain, $\dot{\varepsilon}_0$ and $\dot{\varepsilon}_m$ are reference strain rates, *m* and *a* are rate sensitivity parameters for strain rates below $10^3\ \mathrm{s}^{-1}$ and above $5 \times 10^4\ \mathrm{s}^{-1}$, respectively, σ_0 is the quasi-static yield stress, ε_0 is a reference strain, N is the strain hardening exponent, T_0 is the reference temperature, and β and κ are thermal softening parameters. The function $g(\bar{\varepsilon}, T)$ represents the quasi-static stress-strain response at ambient temperature. The material parameters for the viscoplastic response of HMX are found in Table 3 are fit to the experimental wave profiles obtained by Dick et al. [16] using the method discussed by Menikoff et al. [17].

Table 3. HMX material parameters for viscoplastic constitutive behavior.

σ_0	ε_0	N	T_0	β
260 MPa	5.88×10^{-4}	0.0	293 K	0.0

$\bar{\varepsilon}_0$	m	$\bar{\varepsilon}_m$	a	κ
1×10^{-4}	100.0	8.0×10^{12}	22.5	0.0

2.2.3 Cohesive Finite Elements

The CFEM framework utilizes the idea of cohesive zones in the presence of developing cracks introduced by Barenblatt [53], Dugdale [54], and Rice [55]. The CFEM has been used to study many phenomena related to delamination and fracture including tensile decohesion [56], quasi-static crack growth [57], ductile fracture [58, 59], [60] and fragmentation [29, 61], delamination in laminar composites [62, 63], and microstructural cracking and delamination in particulate composites [64, 65]. In this computational framework, cohesive finite elements are embedded along all element interfaces in the original mesh, as in [64, 65]. This method of inserting cohesive elements allows for semi-arbitrary crack nucleation and propagation, with potential crack paths limited only by the initial mesh resolution.

Each cohesive element is described by a bilinear traction separation law of the form developed by Zhai et al. [65]. In this cohesive model, the traction applied on any cohesive surface (**T**) is work conjugate to the interfacial separation ($\mathbf{\Delta}$). This law is derived from a potential, Φ, which is related to $\mathbf{\Delta}$ through the state variable

$$\lambda = \begin{cases} \sqrt{\left(\dfrac{\Delta_n}{\Delta_{nc}}\right)^2 + \left(\dfrac{\Delta_t}{\Delta_{tc}}\right)^2}, & \Delta_n \geq 0; \\ \left|\dfrac{\Delta_t}{\Delta_{tc}}\right|, & \Delta_n < 0. \end{cases}, \tag{34}$$

where $\Delta_n = \mathbf{n} \cdot \mathbf{\Delta}$ and $\Delta_t = \mathbf{t} \cdot \mathbf{\Delta}$ are the normal and tangential components of $\mathbf{\Delta}$, respectively, and $\mathbf{n}$ and $\mathbf{t}$ are the unit vectors normal and tangential to the cohesive surface. Δ_{nc} and Δ_{tc} are the critical normal and shear separations at which the cohesive strength vanishes and the cohesive element fails. This state variable describes the effective state of the cohesive element under mixed-mode separations. To capture the irreversibility of damage, the monotonically increasing parameter $\eta = \max\left(\eta_0, \lambda_{ul}\right)$ is introduced. η_0 is the initial value of η which describes the initial stiffness of the cohesive element, and λ_{ul} is the maximum value of λ experienced by the element thus far. The limiting values of $\lambda = 0$ and $\eta = 1$ correspond to zero separation and complete element degradation, respectively. The specific cohesive potential implemented here is of the form

$$\Phi = \Phi\left(\lambda, \eta\right) = \begin{cases} \Phi_0 \left(\dfrac{1-\eta}{1-\eta_0}\right)\left(\dfrac{\lambda^2}{\eta}\right), & 0 \leq \lambda \leq \eta \\ \Phi_0 \left(\dfrac{1-\eta}{1-\eta_0}\right)\left(1 - \dfrac{\left(1-\lambda\right)^2}{1-\eta}\right), & \eta < \lambda \leq 1 \end{cases}. \tag{35}$$

where, Φ_0 is defined as the work of separation from the undamaged to fully damaged states. A potential of this form allows for the traction to be defined by

$$\mathbf{T} = \frac{\partial \Phi}{\partial \mathbf{\Delta}}, \tag{36}$$

which allows for the calculation of normal and shear components of the traction

$$T_n = \sigma(\lambda,\eta)\frac{\Delta_n}{\lambda\Delta_{nc}} \text{ and} \tag{37}$$

$$T_t = \sigma(\lambda,\eta)\frac{\alpha\Delta_t}{\lambda\Delta_{tc}}, \tag{38}$$

where, $\alpha = \Delta_{nc}/\Delta_{tc}$, and

$$\sigma = \sqrt{(T_n)^2 + (T_t/\alpha)^2} = \begin{cases} \left(T_{\max}\dfrac{1-\eta}{1-\eta_0}\right)\dfrac{\lambda}{\eta}, & 0 \le \lambda \le \eta \\ \left(T_{\max}\dfrac{1-\eta}{1-\eta_0}\right)\dfrac{1-\lambda}{1-\eta}, & \eta < \lambda \le 1 \\ 0, & \lambda > 1 \end{cases} \tag{39}$$

Previous work with this type of CFEM approach has identified the issue of cohesive surface induced softening when a finite cohesive stiffness is used in the cohesive law [66]. This has been addressed by selecting a sufficiently large initial stiffness corresponding to the choice of element size such that the solution convergence criterion of Tomar et al. [66] is satisfied.

2.2.4 Contact Algorithm

In the current setting, prior to the failure of any cohesive elements, the computational domain of bulk and cohesive finite elements is continuously connected through shared nodes. Upon fracture of any cohesive element, the domain contains free surfaces, which are capable of unrestricted, nonphysical penetration into adjacent elements in a traditional finite element framework. Because this penetration represents a geometrically unacceptable condition in the domain, a mechanism for restricting penetration and modelling contact must be introduced. A contact algorithm consisting of penetration detection and surface traction calculation is described below.

2.2.4.1 Penetration Detection

The penetration detection algorithm employed in CODEX is a four (4) step process. (1) The computational domain is decomposed into overlapping, equally sized zones. Steps (2) – (4) are iterated over each potential contact pair within each of the zones. (2) A "bounding box" check is performed to remove elements that are not in immediate proximity to one another. (3) Each pair of elements is tested to determine if any edge of element 2 is in contact with the fractured edge of element 1. (4) Finally, the contacting elements are required to be on the "outside" of the surfaces in contact. Steps 1 and 2 serve to limit the number of calculations required in the more numerically intensive Steps 3 and 4. In the remainder of this section, these four steps will be discussed in more detail.

The first step in the contact detection routine is a spatial domain decomposition which splits the entire computational domain into overlapping, equally sized zones. Each zone contains a list of potential contact sites. The potential contact sites come in the form of the edges of bulk finite elements which are connected to failed (cracked) cohesive elements. The primary purpose of the spatial decomposition is to increase the computational efficiency of the eventual contact detection calculations. A schematic of the contact detection zones is shown in Figure 4. The size of each zone is 0.42 mm × 0.4 mm and the edges overlap neighboring regions by 0.12 mm. This amount of region overlap has been found to minimize the calculation time of the algorithm while assuring that all contact pairs are detected. The remainder of the contact detection is performed sequentially over each of the zones.

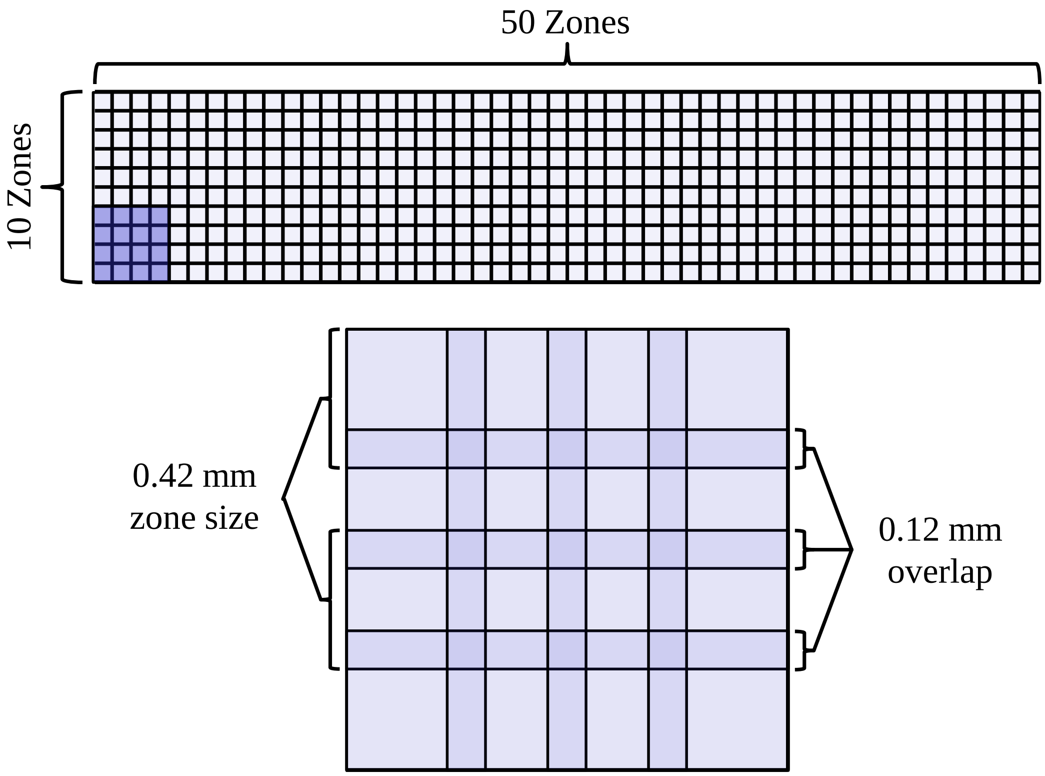

Figure 4. Schematic of the contact detection zones.

Step 2 in the contact detection scheme is the “bounding box” check. Essentially, the bounding box calculation determines if it is geometrically possible for two elements to be in contact (occupy the same space). This is determined by comparing the extents of each element. The extents of element 1 are described by

$$X_1^{\min} = \min\left(X_{1,1},\ X_{1,2},\ X_{1,3} \right) \tag{40}$$

$$X_1^{\max} = \max\left(X_{1,1},\ X_{1,2},\ X_{1,3} \right) \tag{41}$$

$$Y_1^{\min} = \min\left(Y_{1,1},\ Y_{1,2},\ Y_{1,3} \right) \tag{42}$$

$$Y_1^{\max} = \max\left(Y_{1,1},\ Y_{1,2},\ Y_{1,3} \right). \tag{43}$$

In order for any two elements to be in contact, their extents must overlap. This is accomplished in an efficient manner with the evaluation of four simple statements. The bounding boxes of two elements overlap if and only if

$$\boldsymbol{Y}_1^{\min} < \boldsymbol{Y}_2^{\max} \text{, and} \tag{44}$$

$$\boldsymbol{Y}_2^{\min} < \boldsymbol{Y}_1^{\max} \text{, and} \tag{45}$$

$$\boldsymbol{X}_1^{\max} > \boldsymbol{X}_2^{\min} \text{, and} \tag{46}$$

$$\boldsymbol{X}_2^{\max} > \boldsymbol{X}_1^{\min} . \tag{47}$$

This method of checking for an overlap of the bounding boxes reduces the number of potential contact pairs by eliminating non-intimate element pairs. The bounding box check is a quick check of exclusion (it cannot prove contact, but it can prove the lack of contact) that reduces the number times that steps 3 and 4 must be calculated within each zone.

Step 3 of the contact detection algorithm checks if any edge of element 2 intersects the failed surface of element 1. The test for the intersection of two line segments $\overline{\mathbf{AB}}$ and $\overline{\mathbf{CD}}$ is

$$\Theta_1 \bullet \Theta_2 < 0 \quad \mathit{and} \quad \Theta_3 \bullet \Theta_4 < 0 . \tag{48}$$

Where,

$$\begin{aligned}
\Theta_1 &= \begin{vmatrix} A_x - C_x & B_x - C_x \\ A_y - C_y & B_y - C_y \end{vmatrix}, \\
\Theta_2 &= \begin{vmatrix} A_x - D_x & B_x - D_x \\ A_y - D_y & B_y - D_y \end{vmatrix}, \\
\Theta_3 &= \begin{vmatrix} C_x - A_x & D_x - A_x \\ C_y - A_y & D_y - A_y \end{vmatrix}, \\
\Theta_4 &= \begin{vmatrix} C_x - B_x & D_x - B_x \\ C_y - B_y & D_y - B_y \end{vmatrix}.
\end{aligned} \tag{49}$$

All element pairs satisfying the requirements in Step 3 have two defining chaaracteristics: (1) each element contains at least one failed cohesive element, and (2) the two elements contain at least one common location in Euclidean space. Figure 5 shows three possible scenarios that would satisfy Step 3.

While all three scenarios in Figure 5 are mathematically in contact, only scenario 3 on the bottom represents a physical contact event. Step 4 of the detection algorithm evaluates the contacting surfaces from Step 3 to eliminate all false positive contact scenarios (1 and 2). Scenario 1 illustrates the first false positive contact condition. If the two potential contact surfaces in question are to be in contact, the contact surfaces must be oriented “towards” one another. This type of false-positive can be detected by requiring that the outward normal (relative to the bulk finite element) of the two segments point towards one another. Specifically, the dot product of the two outward normal vectors is required to be negative.

$$\hat{n}_1 \bullet \hat{n}_2 < 0 \tag{50}$$

Considering the three scenarios in Figure 5, Equation 18 is satisfied for scenarios 2 and 3 but is not satisfied for scenario 1. Scenario 2 arises due to the use of cohesive finite elements in compression. In this case, the side of element 1 that is detected as contact by Step 3 is the edge connected to the unfailed cohesive element adjoining elements 1 and 2. The outward normal vectors associated with the failed elements satisfy the requirement introduced to catch scenario 1, but the failed cohesive elements in elements are clearly in physical contact. A second requirement is that the failed surface of element 2 lie in the direction of the potential contact surface on element 1 (relative to the center of element 1). This requirement is enforced by ensuring that

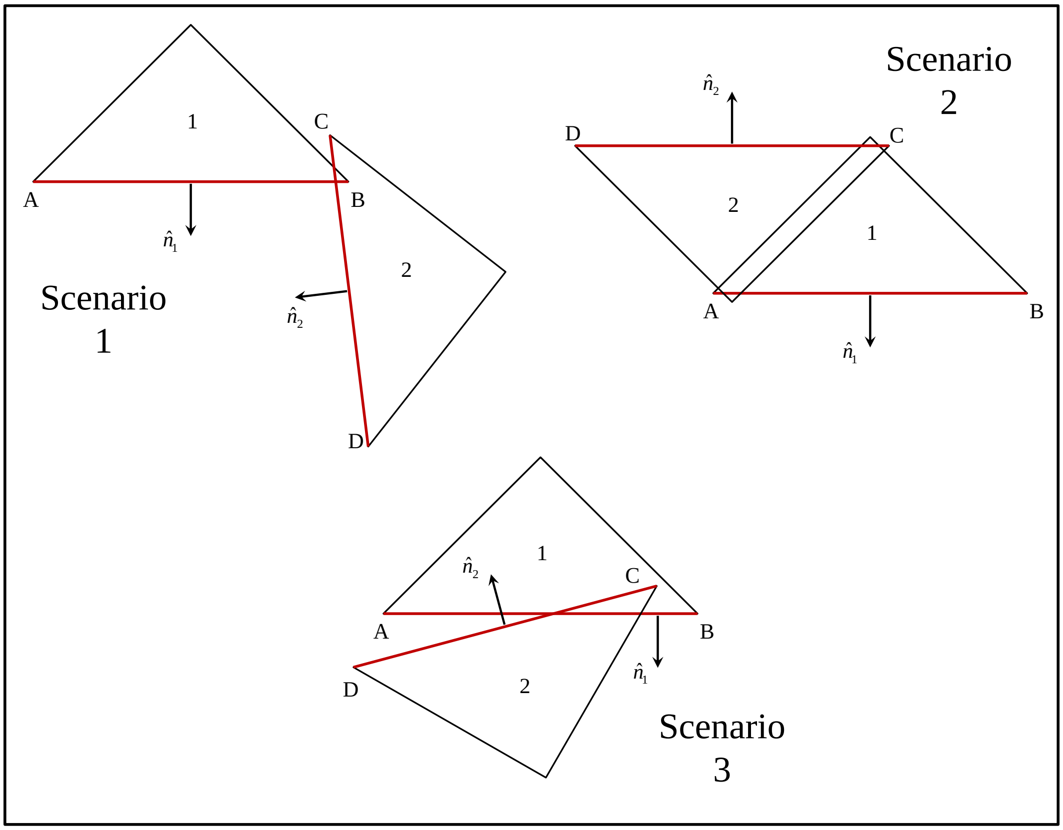

Figure 5. Three generalized contact scenarios that satisfy all requirements of Steps 1, 2, and 3.

$$\overline{AB} \times \overline{B\Lambda} < 0, \tag{51}$$

where, Λ is the centroid of the finite element containing segment $\overline{\mathbf{CD}}$. Scenarios 1 and 3 satisfy this requirement, but scenario 2 is excluded by this additional condition. The effect of the requirements imposed by Equations 18 and 19 is to reduce the set of potential contact pairs such that all remaining pairs represent a physical contact event. Each of these contact pairs is then passed into the contact force calculation, where the normal and tangential surface tractions acting on each element are determined.

2.2.4.1 Surface Traction Calculation

The surface traction calculation evaluates all contact pairs identified by the penetration detection algorithm. The four nodes comprising the contact pair are identified according to the following convention. The nodes of surface 1 are N_1 and N_2, and the nodes of surface 2 are N_3 and N_4 and the nodes are oriented as in Figure 6.

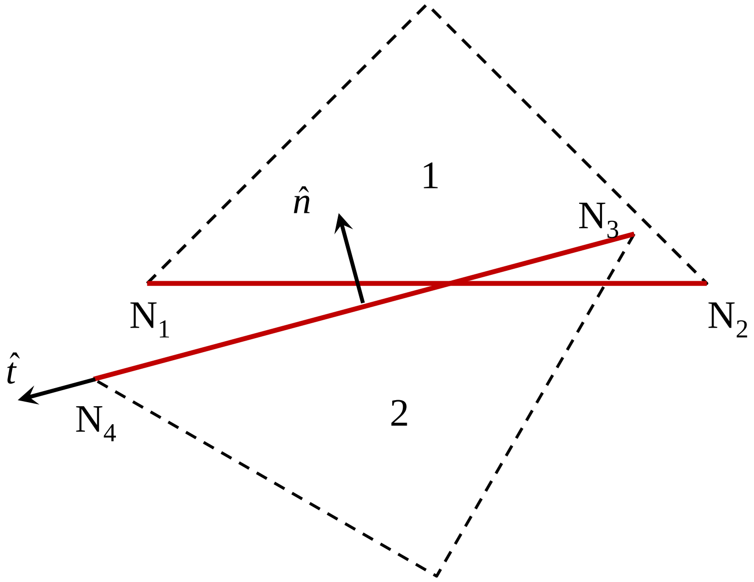

Figure 6. Naming convention for the nodes of a contact pair.

In a given contact event, surface tractions develop in the direction normal to the contact surface to restrict the interpenetration of two bodies and frictional forces develop in the direction tangential to the contact surface. One issue with calculating general contact between two line segments (edges of a triangular finite element) is determining the directions normal and tangential to contact. This is accomplished here by employing the concept of master / slave contact pairs. Specifically, contact is assumed to occur in the direction normal to surface 2 (and outward from its containing finite element) and friction occurs in the direction of the vector pointing from N_3 to N_4. It is convenient to define a contact coordinate system (*t*,*n*) relative to the orientation of surface 2.

$$\mathbf{X}^{contact} = \begin{bmatrix} X^t \\ X^n \end{bmatrix} = \mathbf{R} \cdot \begin{bmatrix} X^x \\ X^y \end{bmatrix} \tag{52}$$

where **R** is a rotation matrix mapping from the *x-y* coordinate system to the *t-n* system.

$$\mathbf{R} = \begin{bmatrix} \cos\theta & \sin\theta \\ -\sin\theta & \cos\theta \end{bmatrix} = \frac{1}{L} \begin{bmatrix} \left(X_4 - X_3\right) & \left(Y_4 - Y_3\right) \\ -\left(Y_4 - Y_3\right) & \left(X_4 - X_3\right) \end{bmatrix} \tag{53}$$

In this expression, *L*, is the length of surface 2. Now, utilizing *t-n* coordinates, the penetration depth is calculated using the expression

$$\delta = \max(0, X_3^n - X_i^n) \quad i = 1, 2 \tag{54}$$

The weighted average velocity of a given node and the side opposite ($\bar{V}_i^n$) is

$$\begin{aligned} \bar{V}_1^n &= \frac{1}{2}\left(V_1^n + \beta_1 V_3^n + \left(1 - \beta_1\right) V_4^n\right) \\ \bar{V}_2^n &= \frac{1}{2}\left(V_2^n + \beta_2 V_4^n + \left(1 - \beta_2\right) V_3^n\right) \\ \bar{V}_3^n &= \frac{1}{2}\left(V_3^n + \beta_3 V_1^n + \left(1 - \beta_3\right) V_2^n\right) \\ \bar{V}_4^n &= \frac{1}{2}\left(V_4^n + \beta_4 V_2^n + \left(1 - \beta_4\right) V_1^n\right) \end{aligned} , \tag{55}$$

where V_i^n is the velocity of the *i*-th node in the direction of the *n*-axis,

$$\begin{aligned}\beta_1 &= \frac{L_{14}}{L_{13}+L_{14}}\\ \beta_2 &= \frac{L_{23}}{L_{23}+L_{24}}\\ \beta_3 &= \frac{L_{23}}{L_{13}+L_{23}}\\ \beta_4 &= \frac{L_{14}}{L_{14}+L_{24}}\end{aligned}, \tag{56}$$

and L_{ij} is the distance between nodes *i* and *j*. The average acceleration of each node ($\bar{A}_i^n$) is calculated in an identical manner. The normal force on each node is then calculated using the relationship

$$F_i = m_i \Delta\tilde{A}_i^n = \frac{1}{2}\left(\frac{1}{2}\left(\bar{A}_i^n - A_i^n\right) + \frac{1}{dt}\left(\bar{V}_i^n - V_i^n\right) + \mathrm{c}_1\delta\right), \tag{57}$$

where m_i is the lumped mass of node *i*, *dt* is the time step size, and c_1 is a scaling constant. The first two terms in this expression restrict additional penetration between the two surfaces. The third term acts to reduce the amount of penetration that existed prior to the current time step. In general, this inherited penetration is due to compressive loading of cohesive elements prior to failure due to shear (tangential) separation. Inherited penetration from compressive loading of cohesive elements restricts the use of a penalty stiffness type contact force that is dependent only on penetration depth δ. In this computational framework, penalty forces dependent only upon the penetration depth are highly unstable because the penetration due to the cohesive elements is applied suddenly upon fracture of the cohesive element. Force equilibrium on the contact surfaces is then enforced with the relationship (similar expressions can be written for the forces on nodes 2, 3, and 4)

$$\Delta A_1^n = \frac{1}{2}\left(\Delta\tilde{A}_1^n - \frac{\Delta\tilde{A}_3^n + \Delta\tilde{A}_4^n}{2}\right). \tag{58}$$

After calculation of the normal forces on the contact pair, the tangential forces on the contact surface are calculated according to a Coulomb friction paradigm. The details of the frictional calculation follow. The relative sliding of surfaces 1 and 2 (in the absence of friction) is calculated from the relative tangential acceleration ($\hat{A}_i^t$) and relative tangential velocity ($\hat{V}_i^t$)

$$\hat{\delta}_i^t = \hat{A}_i^t \cdot \frac{dt^2}{2} + \hat{V}_i^t \cdot dt\,, \tag{59}$$

where $\hat{V}_i^t$ and $\hat{A}_i^t$ are calculated in similar manner by

$$\hat{A}_1^t = A_1^t - \beta_1 A_3^t - \left(1-\beta_1\right) A_4^t. \tag{60}$$

In this expression, the velocity and acceleration at each node is compared to the weighted average of the velocity and acceleration of the two nodes on the opposite surface. In the current framework, the effect of friction can range from frictionless sliding ($\delta_i^t = \hat{\delta}_i^t$) to slipless friction ($\delta_i^t = 0$). The relationship describing Coulombic friction is

$$F_i^t \le F_i^n \cdot \mu \tag{61}$$

where F_i^t is the tangential force at node *i* and μ is the applicable coefficient of friction. If the tangential driving force on the contact surface ($\hat{A}_i^t$) exceeds the normal force on the contact surface ($\hat{A}_i^n$) times the coefficient of friction, then a tangential force $F_i^t = F_i^n \cdot \mu$ is applied to the nodes of the contact surface and relative motion between the nodes is allowed. If the driving force is less than required for slipping, the force applied by friction is sufficient to restrict relative motion between the surfaces. After applying the friction force, the relative sliding is recalculated in order to determine the frictional work of contact.

$$W_i^f = \delta_i^t F_i^t \tag{62}$$

All of the frictional work of contact is converted into heat and is distributed to the associated nodes. At this point the total nodal force vector is updated for the final time in each time step.

In the selection of a coefficient of friction, there is very little information for the individual constituents of PBX 9501, namely HMX and Estane. Using drop weight impact tests on another HMX based PBX (PBX 9404), Green et al. [14] found that the coefficient of friction is approximately 0.3 – 0.7. With this result as a starting point, Chidester et al. [67] uses a coefficient of friction of 0.5 to model the fricitonal work on a PBX specimen (LX-10-1) and to predict the threshold velocity for impact induced ignition. In another study, Dickson et al. [68] directly measure the coefficient of friction for a sample of PBX 9501. This is achieved by contacting a rotating sapphire disk coated in grit with the PBX specimen and measuring both the normal and lateral forces transferred through the contact. This work finds that the coefficient of friction for PBX 9501 varies between 0.35 and 0.5. For the calculations in Chapters 3 and 4, the coefficient of friction (both static and kinematic) is chosen to be 0.5 for all frictional contact occurring between two HMX particles and for contact between HMX and Estane. Previous work by Barua [4] has shown that for values in the range of 0.5, there is relatively little dependence of the frictional behavior on the specific value of the coefficient of friction.

2.2.5 Loading Configuration

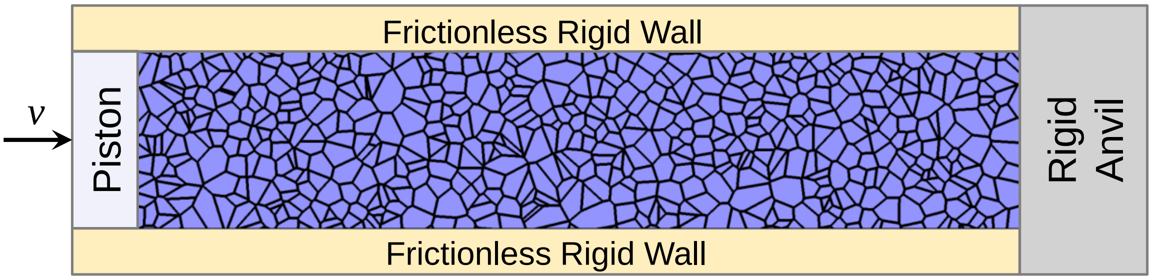

Figure 7. Diagram of the loading and boundary conditions.

The loading configuration used in this analysis are chosen to simulate piston-driven, nominally uniaxial strain conditions in the material. The specimens being tested are each 15 mm in the loading direction and 3 mm in the transverse direction and contain 72% – 90% HMX by area. As seen in Figure 7, the lateral walls constrain the specimen from expanding without introducing friction. The loading is the result of an imposed velocity condition on the left face of the specimen. The velocity is ramped (ramp time, 0.5 μs) to a steady velocity that remains constant for the remainder of the calculation. The range of imposed boundary velocities is from 50 m/s to 200 m/s for all of the 2D PBX microstructures. Analysis of the mechanical and thermal response of the PBX specimens is limited to the material under the influence of only a single pass of the stress wave, therefore wave reflection from the rigid anvil is not considered.

2.3 Postprocessing: Probabilistic Approach to Ignition Sensitivity

2.3.1 Thermal Criticality

Critical to the sensitivity analysis of an energetic material is a methodology for identifying any hotspots generated during the mechanical loading process and determining which hotspots, if any, contain sufficient energy to support sustained chemical reaction, termed thermal runaway. The mechanism for locating hotspots is composed of two (2) processes. Hotspot analysis is done by (1) locating all hotspots of interest, both critical and sub-critical and (2) applying an appropriate criterion to each hotspot in the domain in order to determine if and when each microstructure reaches the critical threshold. Locating hotspots is done by sectioning the domain according to the temperature field. All material below a pre-determined temperature threshold (T^*) is excluded from the analysis and the remaining material is composed of “hotspots”. At this point, all of the significantly heated material in the microstructure have been isolated, but there is no distinction between hotspots that have reached a state of thermal runaway and those that will be quenched by subsequent chemical reaction and conduction. In order to distinguish between critical and subcritical hotspots, a physically informed threshold is needed. Figure 8 shows potential size – temperature thresholds for critical hotspots in HMX as determined by two different sources [34, 38].

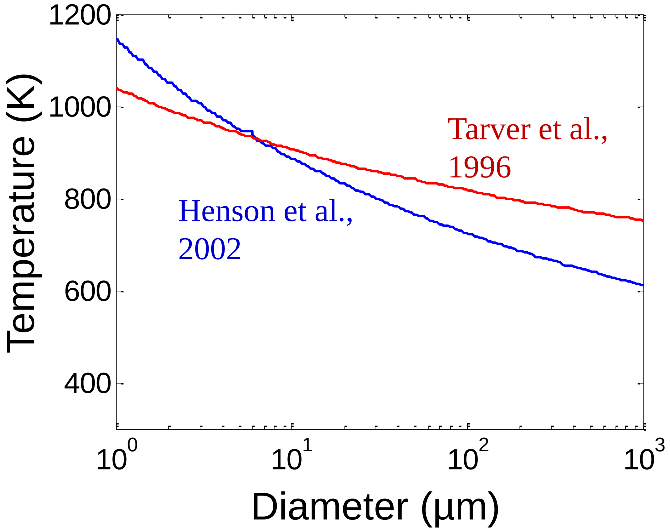

Figure 8. Size – temperature criticality thresholds for HMX using the methods of Tarver et al. [38] and Henson et al. [34].

Tarver et al. determined a critical size-temperature threshold for isolated hotspots with various geometries based on simulations of a four step thermal decomposition model coupled with thermal conductivity of the various chemical constituents. In the analysis of Chapters 4 and 6, the results of Tarver's analysis are used to create a "go / no-go" initiation criterion for hotspots where criticality is determined by a given hotspot's size and temperature in relation to Tarver's threshold. This critical threshold is treated as a material property that indicates an initiation event in any material having sufficient temperature rise over a given amount of HMX. In this way, a distinct time required to generate a hotspot leading to thermal runaway is obtained and can be used to compare various microstructures.

2.3.2 Ignition Sensitivity

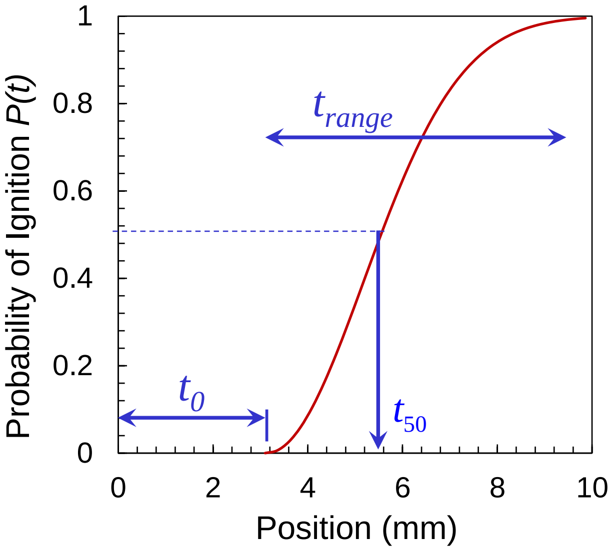

Figure 9. Physical interpretation of the Weibull distribution parameters.

Ignition sensitivity is evaluated through a statistical treatment of the results obtained from the CFEM calculations. In order to quantify the effect of random packing variations in statistically similar (constant particle size distribution, packing fraction) microstructures, this work analyzes multiple instantiations with the same microstructural description for each loading condition. A modified form of the Weibull distribution function is used to describe the probability of ignition for a set of similar microstructures.

$$P(t) = 1 - e^{-\Phi(t)}, \qquad \Phi(t) = \begin{cases} 0, & t < t_0 \\ \left(\dfrac{t - t_0}{\tau}\right)^m, & t \geq t_0 \end{cases} \tag{63}$$

In the above equations, $P(t)$ is the cumulative probability, t is the time to criticality, t_0 is the cutoff or threshold time below which the probability of initiation is zero, τ is a parameter affecting the slope of the distribution, and m is a shape factor. This probabilistic treatment allows for the quantification of the stochastic nature of initiation in highly heterogeneous PBXs. The three primary descriptors that are used to characterize and compare ignition sensitivity for different loading and material cases are shown in Figure 9. The threshold time (t_0), mean time to criticality (t_{50}), and range of probable ignition times (t_{range}) and can be obtained from the Weibull distribution function. Using t_0, t_{50}, and t_{range}, this study describes the initiation behavior and quantifies the effect of changing material properties and loading conditions on the initiation sensitivity of a PBX.

CHAPTER 3: VISCOPLASTICITY AND THE MECHANICAL BEHAVIOR OF PBX

Initiation events occur across such a large spectrum of both shock and non-shock situations, therefore it is crucial that the mechanisms leading to energy localization are well understood at the critical length and time scales for all loading types. Because hotspot formation is difficult to diagnose experimentally, computations which model the active dissipation mechanisms and microstructural complexity of the PBX composites can be used to study the mechanical, thermal, and damage processes which lead to or increase the likelihood of hotspot generation.

The focus of this chapter is to calculate, quantify, and analyze the effect of viscoplastic HMX on the mechanical, thermal, dissipative, and damage response of a two-phase PBX. Specific attention is given to fully characterizing the dynamic material response of PBXs comprised of an Estane binder and HMX grains by isolating and understanding the role of plasticity, fracture, and friction as well as how these mechanisms interact with one another. The CFEM framework is used to predict the response of a systematically varying set of microstructures to loading by piston velocities ranging from 50 to 200 m/s. The mechanical, thermal, dissipative, and damage response of each set and the effect of viscoplastic HMX is extensively quantified as functions of imposed piston velocity, HMX packing fraction, and distance from the piston.

3.1 Methodology

CFEM calculations are carried out on sets of PBX microstructures having HMX area fractions of 0.72, 0.76, 0.81, and 0.90 using the CFEM framework described in

Chapter 2. Each set of microstructures consists of twenty instantiations with similar average grain size and grain size distributions. These sets of microstructures are described in detail in Chapter 2.1.1. To clearly delineate the effect of viscoplasticity on the thermal and mechanical response of the PBX specimens, each specimen is tested two times. The first time for each specimen contains hyperelastic HMX and the second contains HMX modeled using the viscoplastic constitutive relation. For each test, the specimen is loaded by means of a virtual piston with a specified velocity history in the direction parallel to the long axis of the specimen. The specific loading history is shown in Figure 10.

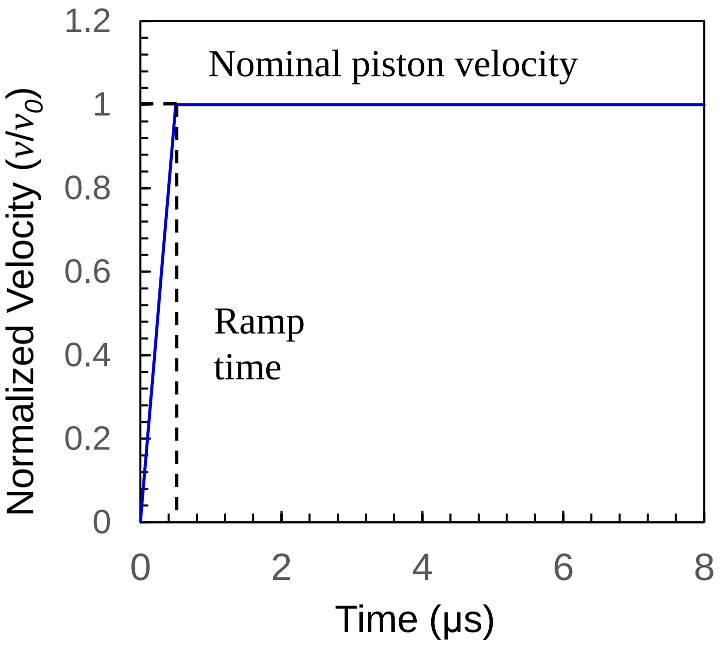

Figure 10. Velocity history for uniaxial loading of PBX specimens using CODEX.

Each specimen is loaded with piston velocities ranging from 50 to 200 m/s in order to capture the effect of viscoplastic deformation in the HMX grains over a large range of loading conditions. The boundary conditions on the remaining faces of the domain are chosen such that the specimen is fully confined by a frictionless boundary. The loading scenario is thus one of nominally uniaxial strain on the scale of the specimen. Analysis of the thermal and mechanical response of the PBX specimens is then restricted to the period of time prior to the stress wave reflecting off of the rigid wall, initially located 15 mm from the piston face. The response of the PBXs to impact loading are evaluated in terms of the kinematic behavior (velocity and acceleration), mechanical behavior (axial stress, von Mises equivalent stress, and hydrostatic stress), thermal behavior, dissipative processes (frictional, viscoelastic, and viscoplastic dissipation), and damage (binder fracture, intragranular fracture, and debonding) in the following sections. The objectives of this analysis are to fully describe the behavior of fully dense PBXs under impact loading and to quantify the effect of viscoplastic HMX on the response of the system as a whole over a range of stimuli.

3.2 Kinematic Response of PBXs

3.2.1 Characterization of Heterogeneous Velocity Field

The velocity field is the primary characteristic of the kinematic response of the PBX to impact loading. Figure 11 shows the average longitudinal velocity for both the elastic and viscoplasic cases as functions of position (initial distance from the piston face). At low piston velocities, the velocity increases rapidly from zero to a very high fraction of the piston velocity, then steadies into a region of nearly constant velocity. The length of material (in mm) required for the longitudinal velocity profile to accelerate from a stationary to a steady velocity is subsequently referred to as the width of the velocity or stress wave (w_s). For high piston velocities, the velocity similarly increases steeply from zero over a distance of w_s. However, in the region behind the wave front, the velocity continues to increase slowly to a maximum value of the imposed piston velocity at the loaded surface. As a result of this gradient in the velocity field, in high piston velocity cases the material behind the wave front will experience additional axial compression behind the stress wave front, but at low impact velocities all of the axial compression will occur during the initial loading period.

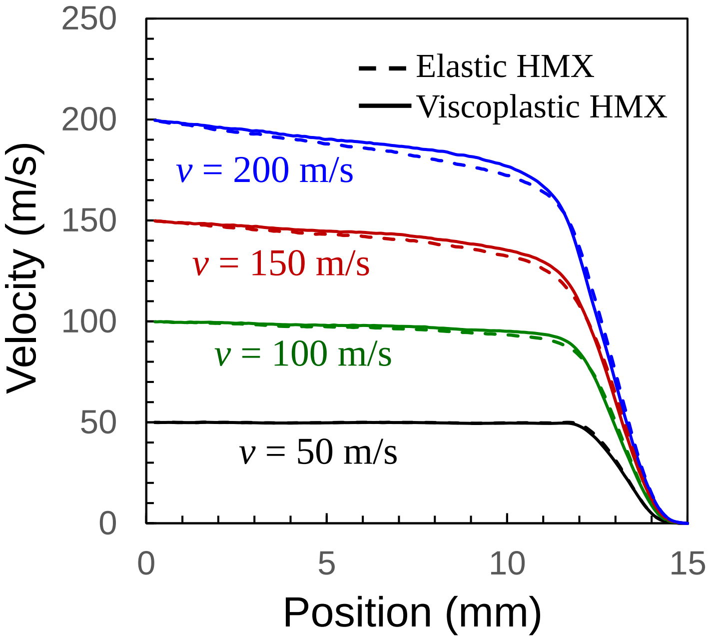

Figure 11. Average longitudinal velocity as a function of position for an HMX packing fraction of 0.81 and piston speeds ranging from 50 – 200 m/s.

Spatial variations in the velocity field develop due to the geometric and mechanical heterogeneities that exist in each PBX microstructure. These fluctuations can lead to increased localized stresses or, in the case of free surfaces, relative sliding. Figure 12 shows the standard deviation of the (a) longitudinal and (b) transverse velocity field as a function of distance from the piston for the entire specimen. It can be seen that the velocity fluctuations in the longitudinal and transverse directions correspond well with one another everywhere in the wave profile except for the region near the wave front (distance from piston > 12 mm). This correspondence indicates that the fluctuation vector is approximately 45 degrees relative to the loading direction, which is the direction of the majority of the fractured surfaces in the domain. Taken together, the fluctuations in the velocity field of a fully dense PBX are dominated by the relative sliding of fractured (or debonded) material. In the region near the wave front, the standard deviation of the velocity field is significantly higher in the longitudinal direction than in the tangential, indicating that fracture and frictional sliding is not yet a dominant feature in velocity fluctuations in the vicinity of the wave front.

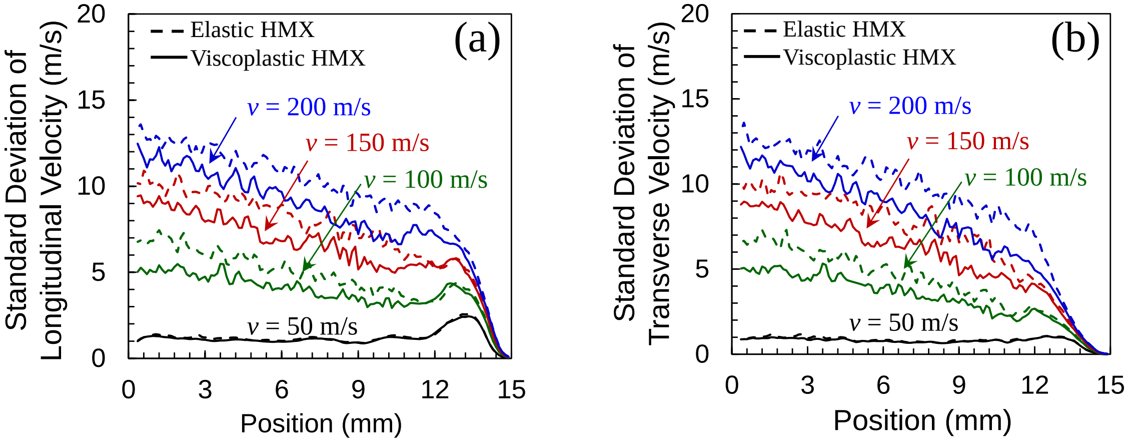

Figure 12. The standard deviation of the (a) longitudinal and (b) transverse velocity as a function of position and piston velocity for specimens having an HMX packing fraction of 0.81.

Figure 13 shows the standard deviation of the longitudinal velocity as a function of position (distance from the piston) and piston velocity in the (a) HMX phase and (b) Estane phase of the composite. For both elastic and plastic HMX, there is significantly more variation in the velocity field of the binder than in the HMX material the same distance from the piston. This effect is most evident at high piston velocities and reduces to a negligible difference at 50 m/s. The difference in magnitude of the velocity fluctuations in the HMX and the binder highlights the possibility of sliding between the grain boundaries and adjacent binder material that has been previously debonded. Sustained, oscillatory relative motion along the grain boundaries would lead to associated heating at sites where the grain boundaries have debonded from the Estane.

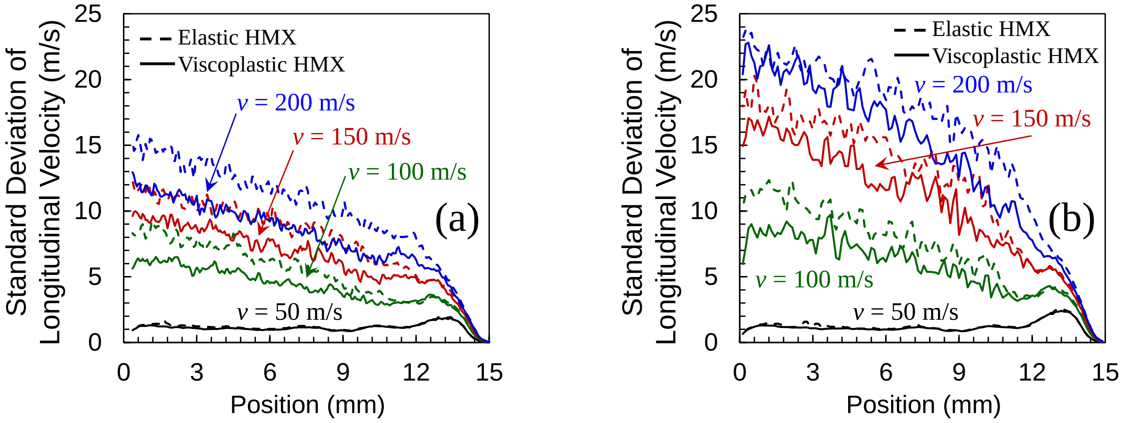

Figure 13. The standard deviation of the longitudinal velocity in the (a) HMX and (b) Estane as a function of position and piston velocity for specimens having an HMX packing fraction of 0.81.

3.2.2 Evolution of the Acceleration Field

The other main component of the kinematic response of the PBX composite is the acceleration. Figure 14 shows the propagation of the acceleration from 1 to 5 μs. For all specimens, with both elastic and plastic HMX, the acceleration begins as a sharp pulse with a width equal to the bulk composite elastic wave speed times the ramp time of the loading curve. As the acceleration pulse propagates down the specimen, it is “blunted”, becoming progressively less severe in magnitude and occurring over a longer period of time. In terms of the rise time of the stress wave, this blunting of the acceleration pulse will be manifested in the form of a widening stress wave front as it propagates away from the piston. Over the range of 0 to 5 μs, the acceleration pulse is significantly blunted for both microstructures containing elastic and plastic HMX grains.

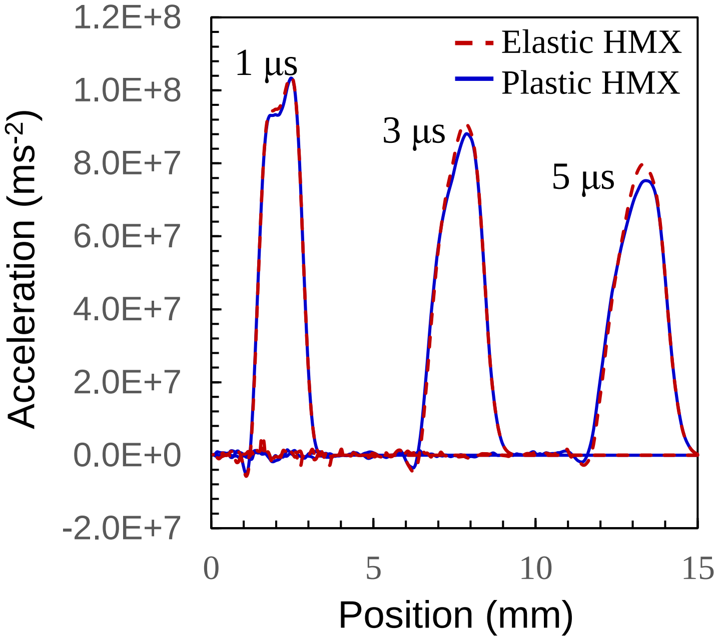

Figure 14. Evolution of the acceleration as a function of longitudinal position for a piston velocity of 50 m/s.

3.3 Mechanical Response of PBXs

3.3.1 Longitudinal Stresses

The first measure of the mechanical response considered is the longitudinal (or axial) stress. Figure 15 shows the longitudinal stress contour map for the same geometry, but having elastic (left) or plastic (right) HMX grains. Both material types show qualitatively similar stress fields. In general, the longitudinal stress fields are characterized by reasonably homogeneous stresses in the HMX grains. The behavior of the binder is dependent on the “orientation” of the binder ligament. For binder regions that are generally parallel to the direction of loading, the stresses are similar to those in the neighboring grains. However, the binder ligaments that are oriented perpendicular to the loading direction have longitudinal stresses that far exceed those in the nearby grains. The blue colored (longitudinal stress > 1 GPa) binder regions are clearly visible for both microstructures in Figure 15.

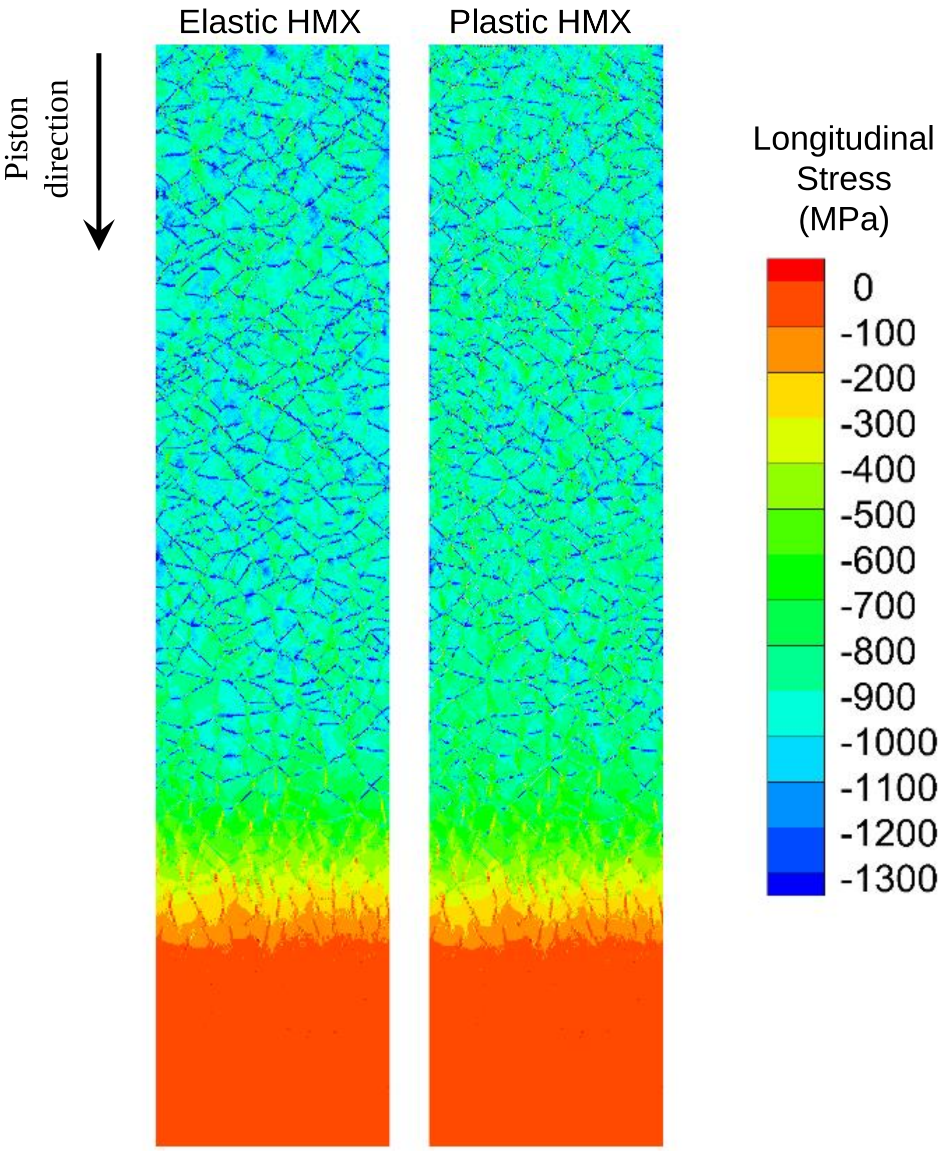

Figure 15. Longitudinal stress contours for PBX specimens with 81% HMX and a piston speed of 200 m/s.

3.3.1.1 Average Longitudinal Stress

The stress contours for the specimens containing either elastic or plastic HMX have many similar trends and characteristics. In order to begin quantifying the magnitude of the differences between them, the average stress as a function of distance from the piston is analyzed. Figure 16(a) shows the average axial stress profile for the twenty instantiations consisting of 81% HMX for piston velocities ranging from 50 to 200 m/s. Figure 16(b) shows the “effect of plasticity” on the longitudinal stress profiles. The effect of plasticity for a given variable is calculated as

$$Plasticity\ Effect = \xi_{plastic} - \xi_{elastic},$$

where, $\xi_{plastic}$ is the value of the variable in the specimens with plastic HMX and $\xi_{elastic}$ is the value of the variable in specimens with elastic HMX. This measure will be frequently used in this section to quantify the direct change in a specific quantity due to the addition of plastic deformation in the HMX grains.

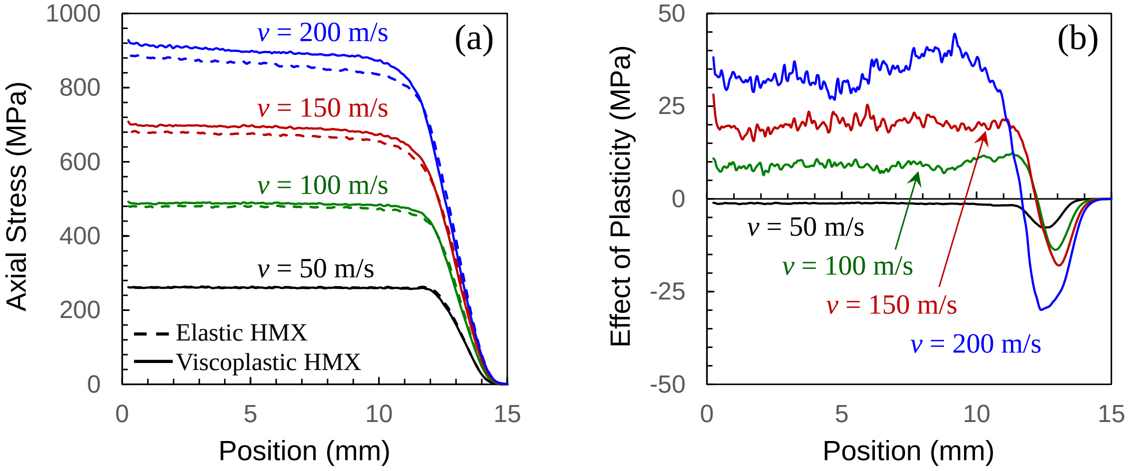

Figure 16. (a) Axial stress profiles and (b) change in axial stress profiles for elastic and viscoplastic HMX specimens having 81% HMX and subject to piston velocities from 50 – 200 m/s.

Figure 16(b) shows that when the HMX is modeled as a viscoplastic material, the average longitudinal stress in the grains is increased relative to the specimens with elastic

HMX for piston velocities greater than 50 m/s. At 50 m/s however, plastic HMX causes a decrease in average longitudinal stress. In a homogeneous elastic-plastic solid undergoing plane strain loading, the stress strain curve follows the constrained or P-wave modulus from the unloaded state to the onset of yielding and then follows the bulk modulus. For a given material, the bulk modulus is always less than the constrained modulus, indicating that the stress in an elastic material should never be exceeded by that in an elastic-plastic material (where the elastic portions are equivalent). The results shown in Figure 16 show the opposite trend, as the piston speed increases, the specimens elastic-plastic HMX carry more stress than their elastic counterparts. This difference is due to damage (fracture) induced by the loading. At low velocities (50 m/s), the damage induced is relatively small causing the plastic HMX to lessen the stress carrying capacity of the composite. However, as the loading intensity increases, significantly more damage occurs in the binder, on the interface between the binder and HMX, and in the HMX itself. The elastic microstructures show significantly more damage than the specimens containing plastic HMX at the same loading intensities. This difference is considered in more detail in Section 3.6.

The level of the longitudinal stress behind the stress wave front is a function of HMX fraction as well as velocity. Figure 17 shows the effective axial stress (average stress behind the wave front), as a function of both packing fraction and piston velocity for the elastic and plastic HMX specimens. Qualitatively, it is clear that for both material types, the effective longitudinal stress increases monotonically with both packing fraction and piston velocity.

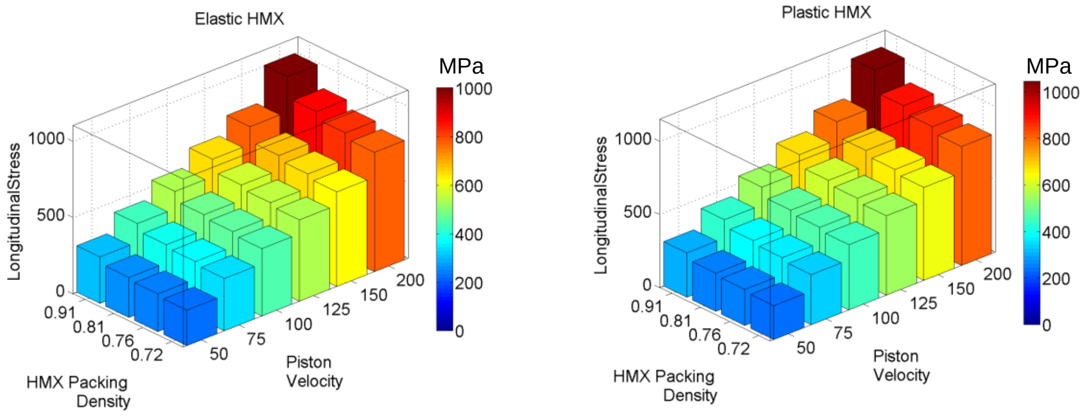

Figure 17. Effective longitudinal stress as a function of HMX packing fraction, piston velocity, and material type.

The effect of plastic HMX on the effective longitudinal stress is a complex interaction. Figure 18 shows the increase in longitudinal stress due to plasticity as a function of piston velocity and HMX packing fraction. For all piston velocities, the magnitude of the effect of plasticity understandably increases with the packing fraction of the HMX. At 50 m/s piston velocity, plasticity in the HMX causes a decrease in axial stress of 1.19 MPa to 1.27 MPa for HMX packing fractions of 0.72 and 0.90, respectively. As the velocity increases, the effect of plasticity is to increase the longitudinal stress in the HMX phase of the material. This effect is indicative of the complex nature of the interactions occurring in these specimens. At low velocities, the material remains relatively undamaged, contributing to a modest reduction in axial stress. At high velocities, however, there is significantly less damage in the specimens with plastic HMX, causing these specimens to carry more axial stress than the corresponding microstructures with elastic HMX.

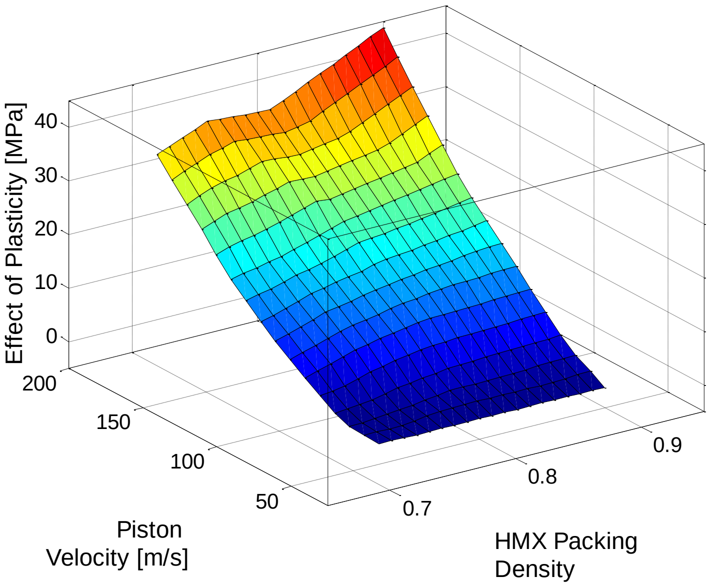

Figure 18. The effect of plasticity on the effective longitudinal stress as a function of piston velocity and HMX packing fraction.

3.3.1.2 Comparison to Experimentally Obtained Hugoniot

As a measure of validation of the mechanical response of the PBX composite, the effective longitudinal stress is compared to experimental results obtained by Dick [6] on the shock loading of PBX 9501 at pressures less than 2 GPa. In order to compare these computational results to those of Dick, the computational results will be fit to an analytical form that represents the effective axial stress as a function of packing fraction and piston velocity. This function takes the form

$$\sigma_{yy}^{eff}(\eta,v)=v\cdot c_1(\eta)+c_2, \tag{64}$$

where, v is the piston velocity, η is the HMX packing fraction, c_2 is a fitting parameter, and

$$c_1(\eta)=c_\eta\cdot\eta. \tag{65}$$

The parameter c_2 controls the predicted stress level for zero piston velocity (or packing fraction). The parameters are fit to the data generated in this study, subject to the constraint that $\sigma_{yy}^{eff}(\eta, 0) = 0$, specifically restricting the function to predict zero longitudinal stress for the whole range of packing fractions when the imposed piston velocity is zero. This constraint leads directly to $c_2 = 0$ for both elastic and plastic HMX cases and c_η is 5.645 for the case of elastic HMX and 5.816 for the specimens with plastic HMX. Figure 19 shows the direct comparison of the current results to those of the low pressure experiments performed by Dick [6].

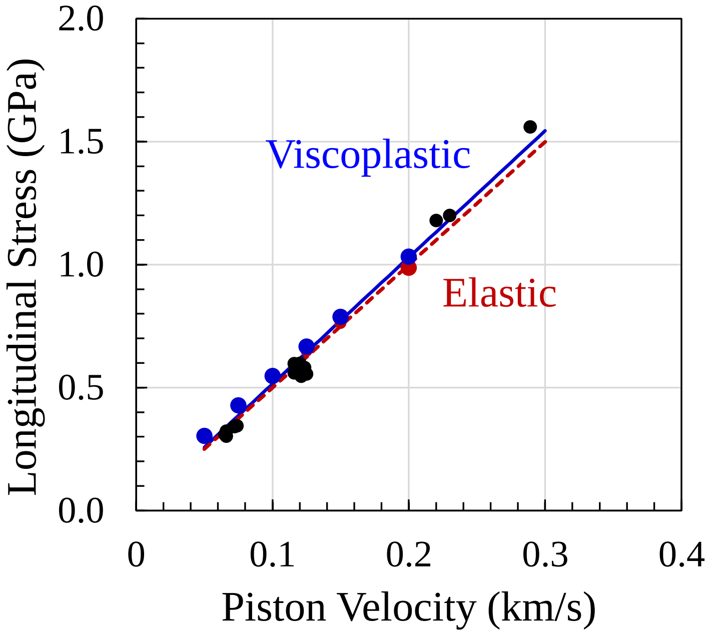

Figure 19. Comparison of computational results to experimentally-obtained axial stress vs. piston velocity Hugoniot [69].

This linear fit to the computational results obtained in this work provides a physically accurate interpretation when extrapolated to low intensity loads and a lower limit of axial stress when extrapolating to higher piston velocities. Because the fit is linear in velocity, it will under-predict the axial stress induced by high intensity loading. Under high impact pressures, the elastic response of both the HMX and the Estane will be stiffer than the applied elastic constants (measured at ambient pressure) due to the pressure sensitive elastic response of both HMX and Estane that is not explicitly modeled here. Figure 19 compares the axial stress versus piston velocity relationship of the results presented here to those of Dick [6]. The dashed and solid lines correspond to the analytical fit for the PBX specimens containing elastic and plastic HMX, respectively. The black circles are the experimental results. The analytical fit shows good correspondence with the experimental results over this entire range of simulated piston velocities (50 – 200 m/s) and when extrapolated to the data point at .289 km/s, underestimates the effective pressure by only 4%.

3.3.2 Von Mises Stress

Evaluating the effect of plasticity on the mechanical behavior of PBX requires an analysis of the von Mises stresses in these scenarios. The von Mises stress is the stress measure most directly influenced by the onset of plasticity. The von Mises stress is also of critical importance because it provides a measure of the total shear stress in the material. The presence of elevated levels of shear stress in the presence of cracks also provides a driving force for frictional slip in damaged materials.

3.3.2.1 Von Mises Stress as a Function of Piston Velocity

Figure 20(a) shows the von Mises stress profile for elastic and plastic HMX cases for an HMX packing fraction of 0.81 and impact velocities from 50 to 200 m/s. The dashed lines, corresponding to the specimens with elastic HMX show a similar trend regardless of the piston velocity. Over the rise time of the stress wave, the von Mises stress increases smoothly from zero to a steady value that increases with loading intensity from 146.3 MPa at to 50 m/s loading to 377.2 MPa for 200 m/s loading. The profiles of the plastic HMX specimens show a nearly identical response for piston speeds less than 100 m/s. At higher impact speeds, however, plastic slip becomes significant and noticeably alters the von Mises stress profile. The characteristic of the profile for the plastic HMX specimens at high velocities is a smooth increase from zero to a maximum value that increases with piston velocity. The maximum von Mises stress level for a piston velocity of 150 m/s is 290.4 MPa, 4.2% lower than the steady level of von Mises stress in the elastic HMX specimens at this velocity of 303.2 MPa. When the piston velocity is increased to 200 m/s, the peak von Mises stress in the plastic HMX profile is 305.8 MPa, 18.9% less than the steady value of 377.2 MPa in the elastic specimens. Following this maximum value, the von Mises stress relaxes to a steady value. Another feature of interest in the plastic profiles is the level to which the von Mises stress relaxes. The profiles for the plastic HMX specimens in Figure 20(a) indicate that the relaxed value of von Mises stress is lower for the higher for the higher velocity impacts. This effect is likely due to the increase in damage associated with increased piston velocity, which lead to reduced shear resistance.

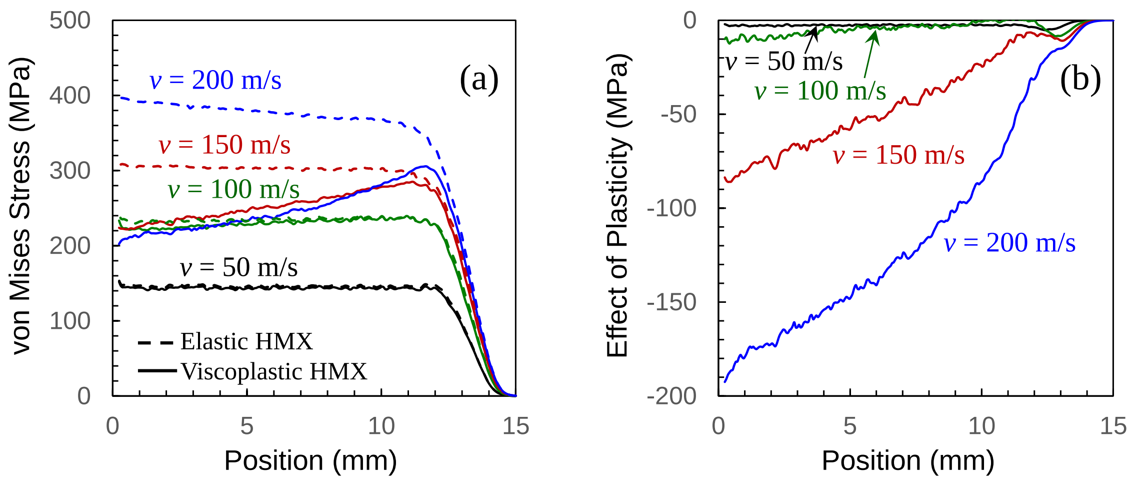

Figure 20. The (a) von Mises stress profile and (b) change in von Mises stress profile due to viscoplasticity for an HMX packing fraction of 0.81 and piston velocities ranging from 50 – 200 m/s.

Figure 20(b) shows the effect of plasticity on the von Mises stress for the same range of piston velocities. At 50 m/s, there is very little effect of plasticity on the von Mises response, indicative of a limited amount of plastic deformation in the specimens at this loading intensity. When loaded with a 100 m/s piston velocity, plasticity causes a decrease in the level of von Mises stress in the plastic HMX over the 5 mm of specimen nearest the piston, but the plasticity has no effect beyond that. For piston velocities of 150 and 200 m/s, significant effect due to plasticity is evident over the entire length of the specimen, indicating that this loading intensity is sufficient to induce plastic deformation in the whole specimen. Extending these observations, for piston velocities below 100 m/s, the heterogeneity-induced shear stresses are not sufficient to cause ubiquitous plastic deformation. For piston velocities near 100 m/s, sufficient plastic deformation is induced to affect a portion of the domain, but is dissipated within the 15 mm specimen length. When the piston velocity exceeds 150 m/s, the stresses in the material are significant enough to induce plastic deformation throughout the 15 mm domain.

3.3.2.2 Distribution of von Mises Stress

The von Mises stress in these microstructures, however, is far from uniform. As a measure of the variability of the von Mises stress states in the material, Figure 21 shows the coefficient of variation of von Mises stress (c_v^{VM}) as a function of piston velocity and HMX packing fraction for (a) elastic HMX and (b) plastic HMX specimens. The specimens with elastic HMX show a monotonic decrease in c_v^{VM} with increasing piston velocity from 0.30 at 50 m/s to 0.14 at 200 m/s for $\eta = 0.72$. The specimens containing plastic HMX, however, do not exhibit a monotonic trend. As the piston velocity increases from 50 to 100 m/s for $\eta = 0.72$, c_v^{VM} decreases from 0.27 to 0.15. For all packing fractions, there exists a minimum in c_v^{VM} between 125 and 150 m/s, followed by an increase in c_v^{VM} of 0.16 to 0.21 from 150 to 200 m/s. For 50 m/s piston velocity, the specimens with plastic HMX have 11% less variability (for packing fractions between 0.72 and 0.81, 13% variability for $\eta = 0.90$). This reduction in variability increases to a maximum of 23% at 100 m/s prior to the change in slope of the plastic HMX specimens. Increasing the piston velocity from 100 to 150 m/s leads to a reduction in variability of only 2%. Above 150 m/s, the specimens having plastic HMX exhibit a 43% increase in the variability of the von Mises stress over the elastic specimens. This drastic change stems from the onset of wide-spread plastic deformation at piston velocities over 150 m/s causing the average von Mises stress to stop increasing. However, the average von Mises stress in the elastic HMX continues to rise as a function of impact velocity, causing the aforementioned increase in variability due to HMX plasticity at high impact velocities.

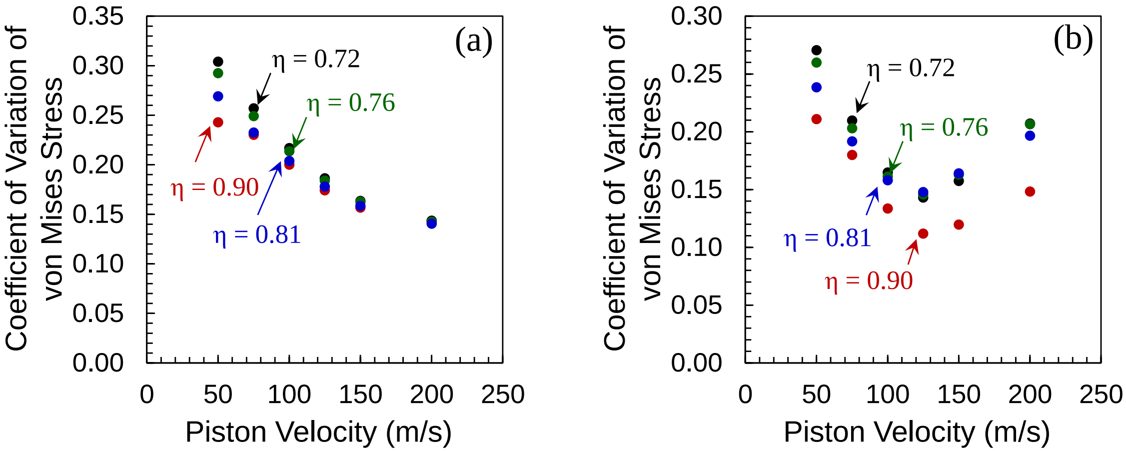

Figure 21. Coefficient of variation of the von Mises stress as a function of HMX packing fraction and piston velocity for specimens having (a) elastic HMX and (b) plastic HMX.

The variability in von Mises stress as a function of packing fraction can also be analyzed using Figure 21. For the elastic HMX, increasing the packing fraction of HMX leads to a reduction of the variability in the von Mises stress distribution. This effect is seen to steadily decrease as a function of piston velocity. At 50 m/s, c_v^{VM} reduces from 0.30 for a packing fraction of 0.72 to 0.24 for $\eta = 0.90$, a reduction of 20%. As piston velocity increases to 200 m/s, the change in variability due to packing fraction decreases to a reduction of only 0.1% for packing fractions from 0.72 to 0.90. For the specimens with plastic HMX, a different trend is present. For the full range of tested piston velocities, the microstructures with an HMX packing fraction of 0.90 exhibited the same trend in variability as the less densely packed microstructures but consistently less in magnitude than the other cases. For the HMX fractions less than 0.90, the effect of packing density increases as a function of c_v^{VM}.

The presence of viscoplasticity in the HMX grains effects the von Mises stress response at the average, specimen, and statistical scales. In terms of average quantities, viscoplasticity reduces the overall level of von Mises stress behind the stress wave for impact velocities exceeding 100 m/s. At 200 m/s, the reduction in effective von Mises stress due to plasticity is 131 MPa, 35% of the stress in the specimens with elastic HMX. On a specimen level, viscoplasticity enforces a limit on the maximum von Mises stress which is a strong function of loading rate but always less than if plasticity were not present. After reaching the peak stress level near the onset of loading, the material then begins to relax to a more steady condition, thereby softening the material. In terms of the distribution of stress states, at low piston velocities, there is more change in the variability of the von Mises stress state due to changes in packing fraction from 0.72 to 0.90 than there is due to introducing viscoplastic HMX. As piston velocity increases, the effect of plasticity in the HMX begins to be the dominant cause of the variability in the stress field, relative to the effect of packing fraction.

3.3.3 Hydrostatic Stress

The hydrostatic stress (pressure) is an important measure of the effect of plasticity on HMX due to its role in frictional interactions. The hydrostatic stress represents an approximate measure of the normal stress on a crack face. According to the principles of Coulomb friction, an increase in normal stress (force) on a crack increases the shear driving force required to cause frictional slip (and associated heating).

3.3.3.1 Hydrostatic Stress as a Function of Piston Velocity

The average hydrostatic stress as a function of distance from the piston and piston velocity is shown in Figure 22(a). The general shape of the hydrostatic stress profiles closely mirror those of the longitudinal velocity profiles. At low stresses, the material behind the stress wave front is subjected to a steady stress level, but as the piston velocity increases, the hydrostatic stress decreases as a function of distance from the piston. This decrease is due to the velocity gradient noted in Chapter 3.2. Because the velocity is decreasing away from the piston, the material behind the stress wave front is continuously being compressed. This continuous compression causes the hydrostatic stress in the specimens to be monotonically increasing in time.

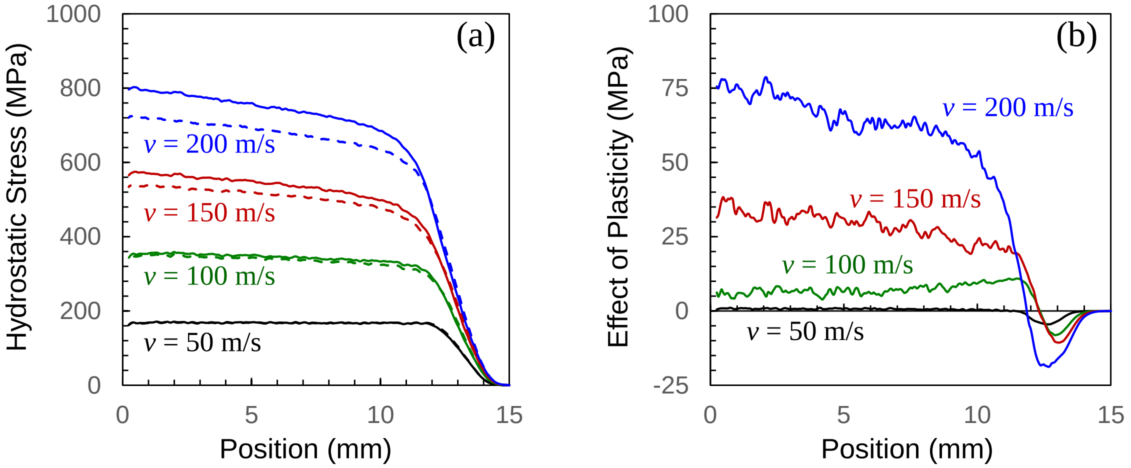

Figure 22. (a) Hydrostatic stress profile and (b) change in hydrostatic stress profile due to viscoplasticity for an HMX packing fraction of 0.81 and piston velocities ranging from 50 – 200 m/s.

Figure 22(b) shows the effect of plasticity on the hydrostatic stress as a function of position and loading intensity. For all piston velocities, the plastic HMX causes a decrease in hydrostatic stress during the loading ramp followed by an increase in hydrostatic stress behind the wave front. The initial decrease in pressure due to plasticity is indicative of the response of an undamaged composite in the presence of plastic deformation. The transition from a decrease in pressure during the ramp to an increase in pressure behind the stress wave is due to the onset and propagation of fracture. Following this region of rapid transition, the effect of plasticity on hydrostatic stress stabilizes into a response that is either steady ($v < 125\ \text{m/s}$) or steadily increasing ($v \geq 125\ \text{m/s}$). For the case of steadily increasing effect of plasticity, the damage (fracture) in the elastic HMX specimens continues to evolve more rapidly than in the plastic HMX specimens enhancing the differences between the microstructures. This difference will be discussed in more detail in section “Damage in PBXs”, below.

In the analysis of the thermal response that follows, the temperature rise in the HMX grains comes from one of three sources: friction, plasticity, or conduction from the binder to the bonded grains. According to the conductivity of HMX and the relatively low temperature of the binder, this mode of temperature rise is not likely to be a dominant mechanism for critical heating and is therefore not explicitly analyzed. The heating due to viscoplastic deformation is due to plastic deformation and von Mises stress and will be discussed explicitly in the following section “Dissipation in PBXs”. Concerning heating due to friction, the effect of plasticity on the hydrostatic and von Mises stresses significantly alters the environment under which frictional slip is occurring (or not occurring). According to Coulomb friction, the two factors determining whether a given contact pair is stationary or slipping are the normal force acting on a crack surface and the tangential driving force., The driving force required to initiate slipping increases linearly with the normal force acting on a given crack. Now, the tangential driving force is related to the equivalent shear stress in the material, as measured by the von Mises stress, and the normal force on the crack surface is related to the hydrostatic stress. Because the addition of plasticity decreases the von Mises stress (driving force) in the HMX grains and increases the hydrostatic stress (normal force), one key effect of plasticity is that it creates a stress state within the various specimens that is less conducive to frictional sliding, thereby reducing a major source of heating within this framework. The effect of plasticity on frictional dissipation is analyzed in more detail in the “Dissipation” section below.

3.4 Thermal Response of PBXs

In the analysis of ignition sensitivity in energetic materials, the temperature rise due to mechanical stimulus is of critical importance. In this section, the temperature in the HMX grains is analyzed in detail. First, a qualitative analysis of the heating in both elastic and plastic HMX specimens will be performed. Following this, the average and peak temperatures are analyzed as well as the effect that plasticity has on these temperatures as a function of HMX packing fraction, piston velocity, and distance from the piston. Using this methodology, characterization of the thermal response in the elastic and plastic HMX is performed on two different scales: local hotspot characterization (qualitative analysis of thermal contours) and the bulk thermal response (average and peak temperatures).

3.4.1 Comparison of Temperature Fields

The first observations of the thermal response of PBXs to impact loading are gained from visual analysis of the temperature contours of the specimens after significant wave propagation. In this way, it is possible to distinguish the mechanisms leading to heating in each of the different loading and material settings. Figure 23 shows the temperature contours of the same geometric microstructure under four different loading and material settings in order to directly analyze the differences. Specifically, the temperature contours resulting from piston velocities of (top) 150 m/s and (bottom) 200 m/s for a specimen having (left) elastic HMX and (right) plastic HMX. All of the contours are taken 4.5 μs after the piston impacts the specimen. For low piston speeds, the temperature rise in the HMX grains is limited to a small number of elements, making contour plots of limited value. The contours shown in Figure 23 provide insight into the active heating mechanisms in each of the cases and the relative importance of each.

The circled regions labeled “A” indicate the types of regions that contain the peak temperature in each microstructure. They are characterized by highly localized heating on the periphery of grains, often near the junction of three or more different grains. The heating in these regions is dominated by friction on multiple crack surfaces and (for the plastic HMX cases) localized plastic heating. The arrows labeled “B” point to intragranular cracks which are heating due to frictional sliding. The heating occurring on cleaved surfaces of HMX is typically sub-critical and not as intense as the heating in the “A” regions. The third type of heating is plastic heating arising from plastic deformation occurring in the majority of the HMX grains (where possible). This bulk plastic heating is both the most common type of heating (in plastic HMX) and the least intense type of heating. Figure 23 shows clear differences in the way that the elastic and plastic HMX specimens localize temperature rise. The elastic HMX specimens are characterized by large quantities of frictional heating due to intragranular cracking as well as multiple “A”-type heating locations. The plastic HMX specimens are very different, they exhibit very few intragranular cracks and a much smaller number of “A”-type locations. In addition, at these piston velocities, all of the HMX material behind the wave front is experiencing low amounts of plastic heating, relatively evenly distributed in the grains.

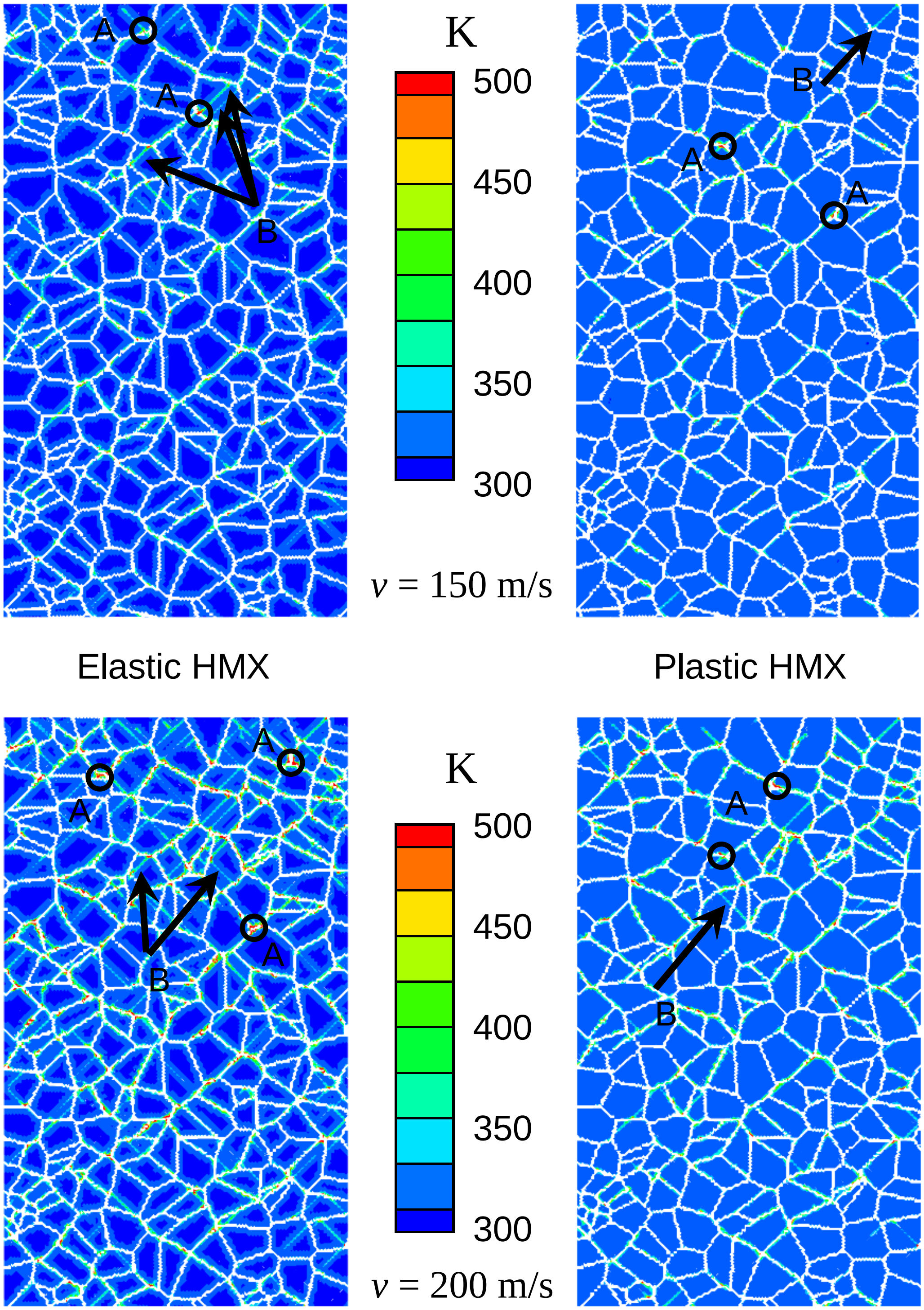

Figure 23. Temperature contours for the HMX portion of the same microstructure due to a piston velocity of (top) 150 m/s and (bottom) 200 m/s. Specimens with elastic HMX are on the left and those having plastic HMX are on the right. The contours occur 4.5 μs after the piston touches the specimen.

Figure 24 shows the average temperature profile and the effect of viscoplasticity on the average temperature as a function of piston velocity and distance from the piston. The average temperature, for all piston velocities, is higher in the specimens with the elastic HMX than those with plastic HMX. The one region of the domain where this is not the case is in the vicinity of the stress wave. In fact, during the stress wave and immediately following, the temperature in the plastic HMX is actually slightly higher than the temperature in the in the elastic grains. This is because widespread plastic heating begins even in the wave front, but the frictional heating does not begin until the wave front has passed through the region. Once the stress wave has passed, the heating in elastic HMX specimens begins to outpace the heating of the plastic HMX specimens. For all piston velocities, the heating in the elastic and plastic HMX specimens is almost the same for the first 5 mm behind the wave front. More than 5 mm behind the wave front, The heating rate in the elastic HMX specimens begins to outgrow the plastic HMX specimens.

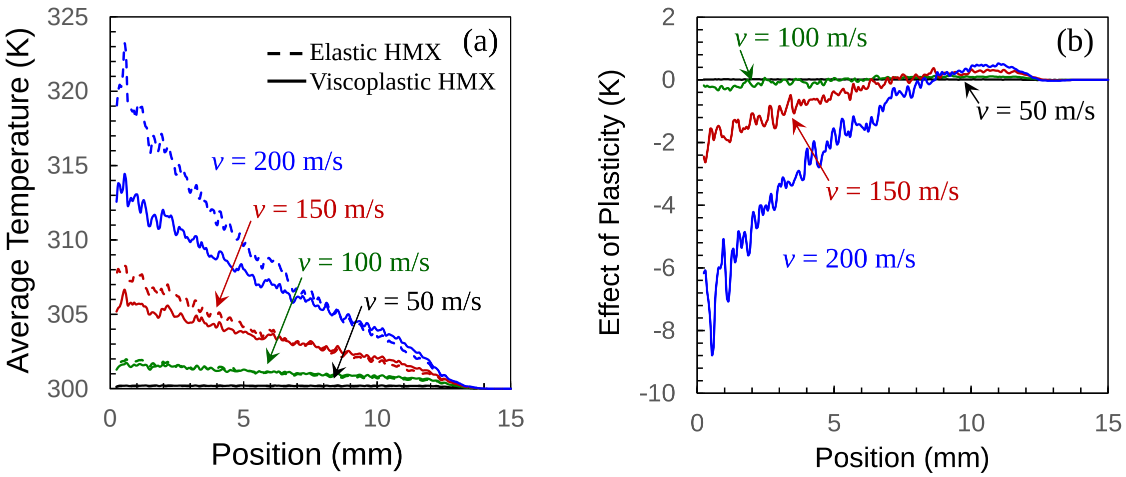

Figure 24. Average temperature profile for HMX packing fraction of 0.81 and piston velocities ranging from 50 – 200 m/s.

3.4.2 Effect of Velocity and Packing Fraction on Average Temperature

The average temperature of all material behind the wave front is considered to be the "bulk", "homogenized", or "effective" temperature for each loading and microstructural condition because the average temperature varies constantly as a function of distance from the piston. Figure 25 shows the average temperature as a function of piston velocity and HMX packing fraction for (a) elastic HMX and (b) plastic HMX specimens. At low piston velocities (up to 100 m/s), the average temperature rise in the specimens with plastic HMX is higher than the specimens having elastic HMX only. For a piston velocity of 50 m/s, the plastic HMX specimens experience approximately 5.5% more heating than the elastic HMX specimens. As the piston velocity increases to 100 m/s, this effect completely disappears. For piston velocities higher than 100 m/s, the plastic HMX specimens experience up to 27% less ($v = 200\,\mathrm{m/s}, \eta = 0.90$) heating than elastic specimens.

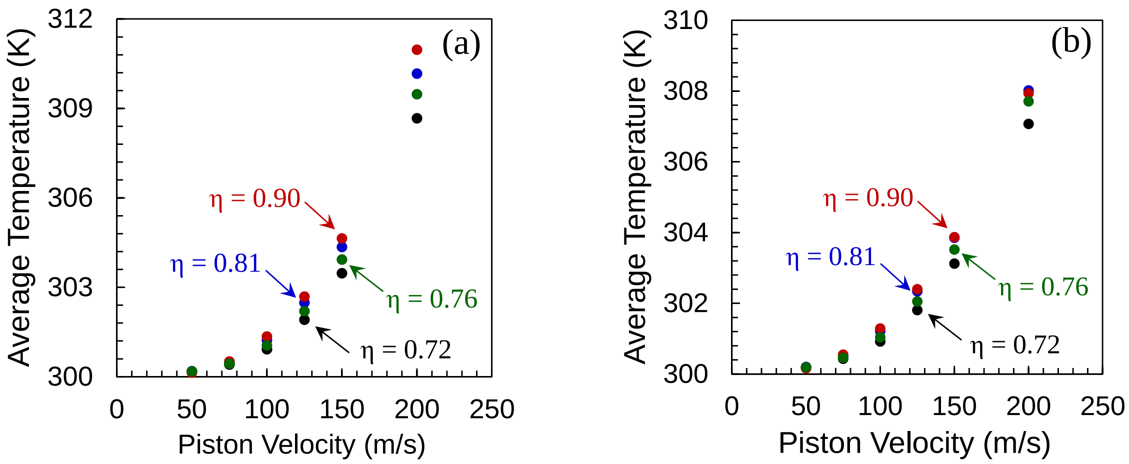

Figure 25. The average temperature behind the wave front as a function of piston velocity and packing fraction for (a) elastic HMX and (b) plastic HMX specimens.

There is very little identifiable difference between the elastic and plastic HMX cases in terms of the form of temperature rise as a function of piston velocity. The primary difference between the two cases is in the magnitude of the heating. For the elastic HMX specimens in Figure 25(a), there is a clear relationship between packing fraction and temperature or temperature rise. A greater fraction of HMX is directly correlated to increased average temperature. For velocities in excess of 50 m/s (at 50 m/s, there is less than 0.2 K heating), an increase in HMX packing fraction from 0.72 to 0.90 is associated with an increase in average temperature of 19 – 31% (0.1 – 2.3 K). The plastic HMX specimens in Figure 25(b), do not show the same trend. Where the elastic HMX specimens heated consistently more with increasing HMX fraction, the average temperature in the plastic HMX specimens for packing fractions of 0.76 to 0.90 remain closely clustered together, even at high piston velocities.

3.4.3 ”Peak” HMX Temperature

The peak temperature in the HMX is used extensively in the calculation of thermal criticality and in some analyses is the primary determining factor in predicting the sensitivity of the PBX composites. Much attention is given to the peak temperature and its importance in evaluating the performance of a PBX in Chapters 4 and 5, therefore this section only briefly considers the peak temperature as a function of distance from the piston for both elastic and HMX plastic specimens. Figure 26 shows the “peak” temperature as a function of distance from the piston for velocities ranging from 50 to 200 m/s. The peak temperature profiles in this figure have been obtained using the following methodology. First, the peak temperature profile for each of twenty statistically similar specimens is created. Then, to obtain a representative profile for the entire microstructure set, the twenty profiles are averaged together, resulting in the profiles in Figure 26. So, the peak temperature profiles in the figure are actually the average (or expected) peak temperature profiles for a generic, random microstructure belonging to the statistical set shown. This averaging scheme leads to the form of the profiles in the figure. Because a peak temperature region is more likely to occur near the piston (this is examined in Chapter 5), the average peak temperature profiles likewise exhibit a maximum near the piston and then decrease towards the wave front. For any given specimen, however, the peak temperature can occur away from the piston. In this analysis, peak temperature regions are located as far as 7 mm away from the impact face.

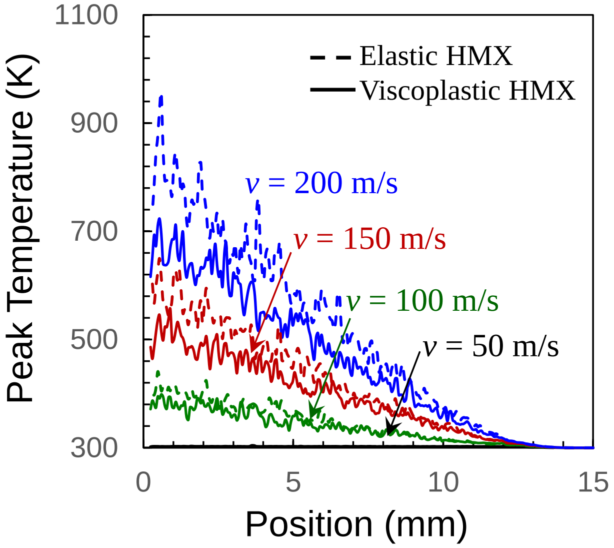

Figure 26. Peak temperature as a function of piston speed and distance from the piston.

Figure 26 shows that the peak temperature in the plastic HMX specimens is lower than that in the elastic HMX for all piston velocities. At low velocities, the differences are modest but increase with loading intensity. At a piston velocity of 100 m/s, the plastic HMX specimens heat by 41 K less than the elastic HMX, a difference of 9.4%. As the loading intensity increases, this difference grows to 94 K and 14.4% at 150 m/s and goes as high as 232 K and 24% at 200 m/s.

3.5 Dissipation in PBXs

Temperature rise in the HMX grains is the cumulative effect of all of the energy dissipated into a given mass of material. The previous section focused on the magnitude and location of the temperature rise. This section investigates the mechanisms which cause the heating to occur, namely the various dissipation mechanisms such as frictional dissipation and viscoplastic dissipation. Of specific interest here is the way that plasticity in the HMX changes the way that energy is dissipated in terms of types, location, and rate of energy dissipation.

3.5.1 Effect of Piston Velocity on Dissipation Mechanisms

This section focuses on quantifying the magnitude of the effect of viscoplasticity on the dissipation in a PBX setting over a range of piston velocities. For the sake of clarity, the microstructures having an HMX packing fraction of 0.81 will be discussed here and the effect of packing fraction on dissipation is the topic of the following section. In general, the dissipation in the HMX grains is due to either frictional or plastic work. The frictional dissipation as a function of piston velocity and distance from the piston is given in Figure 27(a). It is apparent that for both the elastic and plastic HMX specimens, the frictional dissipation is a decreasing function of distance from the piston, which reaches zero dissipation near the rear of the wave front (about 13 mm on the “Position” axis). Microstructures containing plastic HMX have between 49.4% and 57.6% less frictional dissipation given the same magnitude of piston velocity. This reduction in frictional dissipation likely reduces not only the magnitude of the hotspots generated but also the frequency (spatial and temporal) at which hotspots form in each test because many regions of extreme heating occur in the presence of frictional sliding along cracked surfaces.

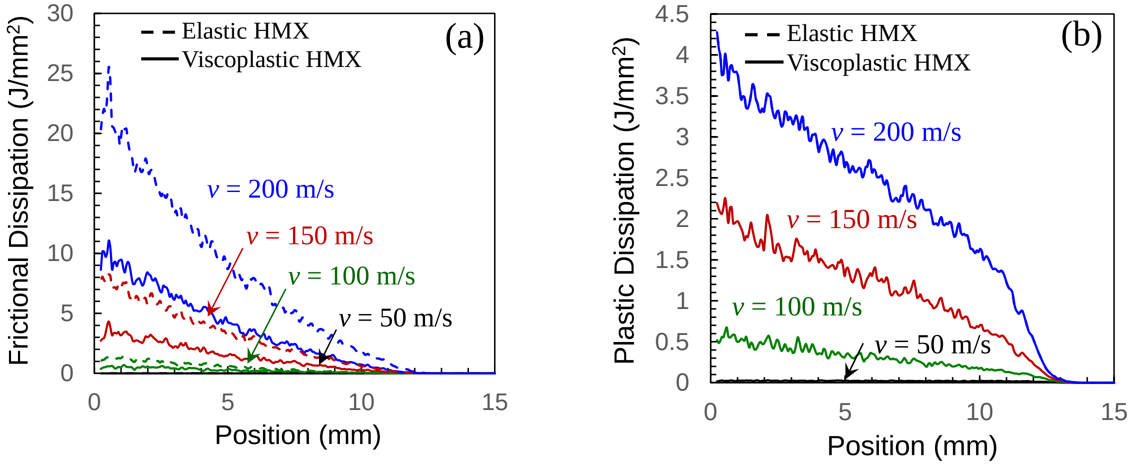

Figure 27. (a) Comparison of frictional dissipation as a function of distance from the piston and (b) plastic dissipation as a function of distance from the piston after 5 μs of loading.

Figure 27(b) shows the plastic dissipation as a function of position over the range of piston velocities. Only the profiles for the specimens having plastic HMX are shown, because only they are capable of having plastic dissipation. One distinct difference between the frictional and plastic dissipation profiles is the shape. The frictional dissipation profiles grow as an approximately quadratic function of distance behind the wave front. The plastic dissipation profiles, however, begin to rise sharply within the wave front and then flatten into nearly linear growth as a function of distance behind the wave front after the initial rise. Figure 28(a) shows the profiles for total dissipation (frictional + plastic) as a function of position and piston velocity. The total dissipation profiles are a linear combination of the profiles in Figure 27. The profiles show that the dissipation in the material in the vicinity of the wave front is dominated by plastic dissipation associated with the compression of the specimen. After the passage of the wave front, frictional dissipation takes over as the primary heating mechanism. It is in this friction-dominated region that the hotspots typically occur under the current loading conditions. The partitioning of the total dissipation profile into frictional and plastic parts is shown in Figure 28(b). The specific profiles in this figure correspond to microstructures with an HMX packing fraction of 0.81 loaded with a piston velocity of 200 m/s. At a piston velocity of 200 m/s, the specimens with plastic HMX dissipate 27.4% less total energy than the elastic specimens. In addition, the dissipation in the plastic HMX specimens is partitioned into frictional dissipation that is highly localized on crack surfaces and plastic dissipation that is distributed throughout the HMX grains. The specimens with plastic HMX dissipate 50.7% less energy through friction than do the elastic HMX specimens. This reduction in surface based frictional dissipation will greatly reduce the rate and frequency at which hotspots (regions of energy localization) are generated in specimens capable of plastic deformation.

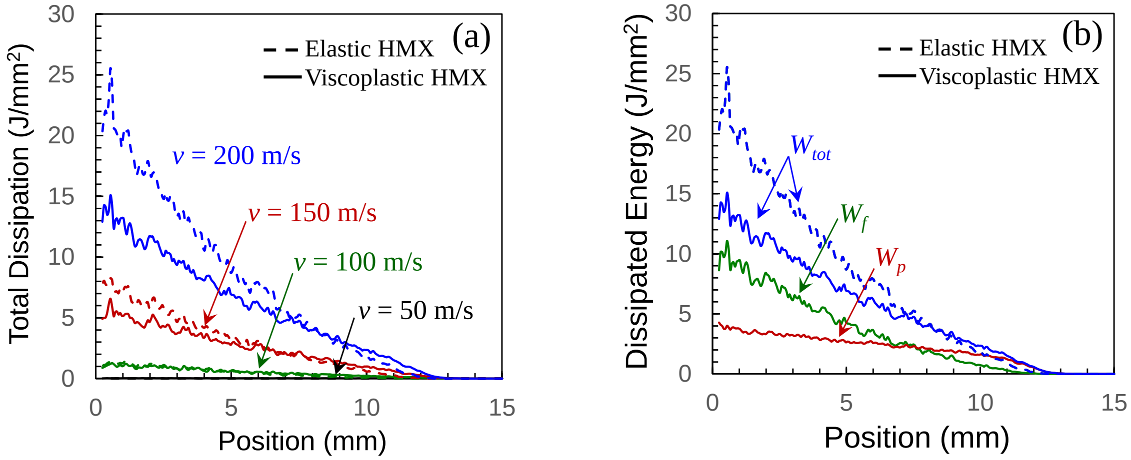

Figure 28. (a) Comparison of total dissipated energy profiles for 0.81 HMX fraction after 5 μs of loading and (b) partitioning of the total dissipation in HMX grains into profiles of frictional and plastic dissipation.

3.5.2 Change in Dissipation Rate Due to Microstructure and Loading

The effective dissipation rates of frictional and total energy for the first 5 μs of loading are calculated as a function of both packing fraction and piston velocity in order to determine the magnitude of the effect of plasticity on the active dissipation mechanisms. The dissipation rates here are calculated as Joules dissipated per microsecond per millimeter of impact surface. This provides a measure of dissipation rate that is insensitive the specimen size. Figure 29 shows the frictional dissipation rates over the full range of test space considered. As expected, the dissipation rates of specimens with only elastic HMX represent a scaled measure of the average temperature behind the wave front because frictional dissipation is the only pertinent heating source for these microstructures. To summarize, the dissipation rate for specimens with elastic HMX increases more than linearly as a function of piston velocity and almost linearly as a function of HMX packing fraction. The specimens with plastic HMX behave differently, however. The frictional dissipation rate for all velocities greater than 50 m/s is between 46 and 60% lower for the plastic HMX specimens but have a similar dependence on piston velocity. For the plastic HMX specimens at high impact velocities, the trend of concerning the dependence of the frictional work rate on packing fraction is violated. Figure 29 shows that for velocities greater than 150 m/s, the specimens with a packing fraction of 0.81 have the highest frictional dissipation rate of any microstructural configuration containing plastic HMX. It is thought that the reduction in dissipation for the most dense PBXs is due to a decrease in the geometric heterogeneity.

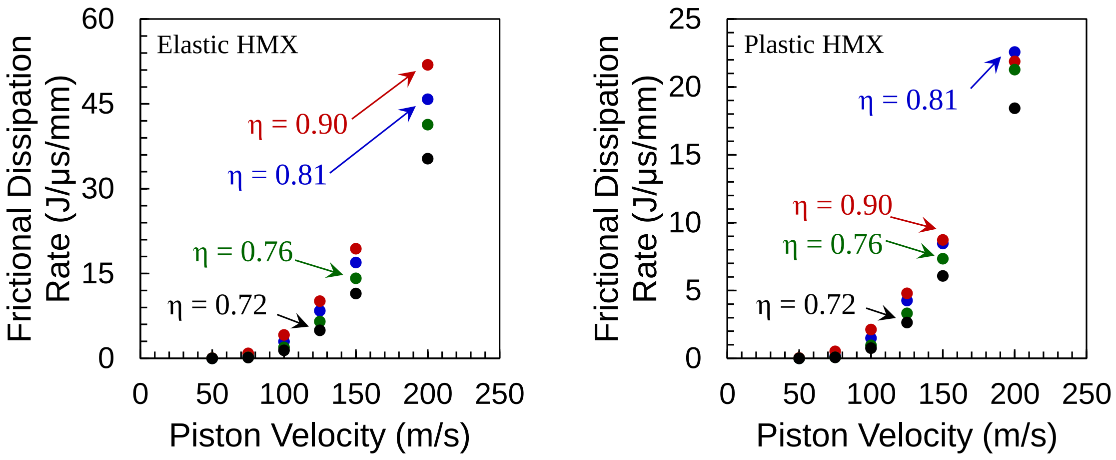

Figure 29. Effective frictional dissipation rate in the HMX through 5 μs.

The total dissipation rates in Figure 30 show that the trend of increasing dissipation with packing fraction is prevalent in both the elastic and plastic HMX specimens. The presence of this trend in the total dissipation rate for the plastic HMX but not the frictional dissipation rate indicates that as the loading intensity increases, the plastic dissipation rate is significantly greater in microstructures with more HMX, compensating for the lower frictional dissipation rate at high packing fraction and velocity.

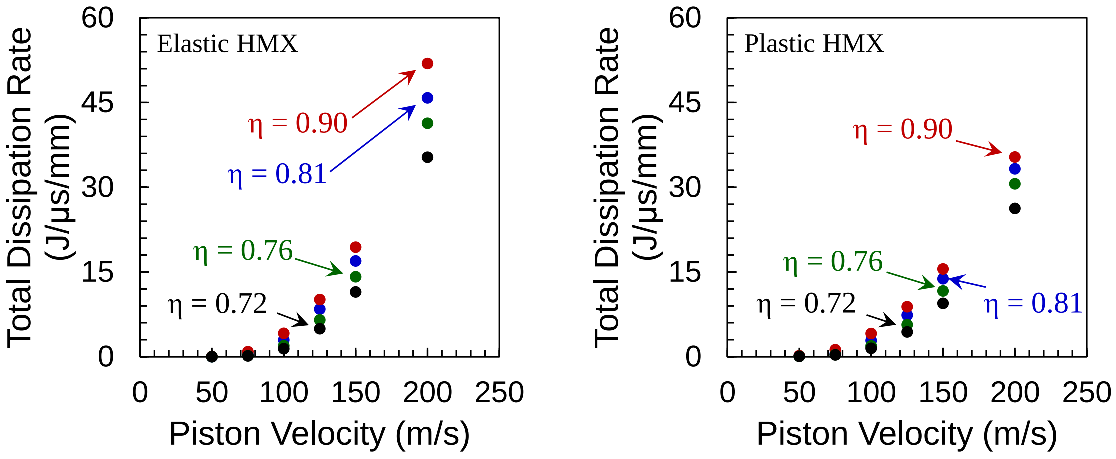

Figure 30. Effective total dissipation rate in the HMX for the first 5 μs.

Allowing for viscoplastic deformation in the HMX grains of a PBX specimen has a significant effect on both the magnitude and mechanisms associated with energy dissipation leading to temperature rise. The total dissipated energy available to heat the plastic HMX is up to 31% less than the energy dissipated by friction alone in the elastic HMX specimens. Further accentuating the difference in potential local hotspot sites between the elastic and plastic HMX is the fact that up to 38% of the total dissipation in the plastic HMX specimens comes in the form of plastic dissipation that is distributed to a large volume (area) of HMX and therefore generating relatively little temperature rise. The specimens having plastic HMX also dissipate up to 57% less energy onto cracked surface by means of frictional dissipation, greatly reducing the propensity for hotspots.

3.6 Damage in PBXs

In a two-phase composite, there are three types of potential fracture that can occur, cracks (or damage) in either of the phases or debonding of the two phases along the interface. The purpose of this section is to quantify the primary damage mechanisms for the PBX of interest and to evaluate the magnitude of the effect of HMX viscoplasticity on the various types of damage. This is achieved by analyzing the fracture density (measured in number of fractures per square millimeter of specimen) of the three types of damage over the full range of loading and microstructural settings.

3.6.1 Binder Fracture

Fracture in the Estane binder occurs during impact events because the viscoelastic binder material becomes stiff and “glassy” under high loading rates. Figure 31 shows the fracture density in the Estane as a function of piston velocity and HMX packing fraction for both the elastic and plastic HMX specimens. In general, all specimens follow a similar trend, the binder fracture density increases more than linearly as a function of piston velocity and decreases monotonically as a function of HMX packing fraction. Interestingly, there is a significantly larger decrease in binder fracture density in the 0.90 packing fraction specimens. For both the elastic and plastic HMX specimens, the 90% dense specimens exhibit between 80 and 90% less fracture per mm^2 than the 0.81 packing fraction specimens. This drastic decrease in fracture density indicates that very different response mechanisms may be active for PBXs with dense packings of HMX. At very low velocities (< 75 m/s), there is very little binder fracture in any of the microstructures. As the piston velocity increases to 100 m/s, the density of fracture in the binder of the plastic specimens is as much as 61% lower than that of the elastic HMX specimens. For a piston velocity of 200 m/s, the reduction in binder damage due to HMX plasticity decreases to between 19 and 26%, depending on the packing fraction.

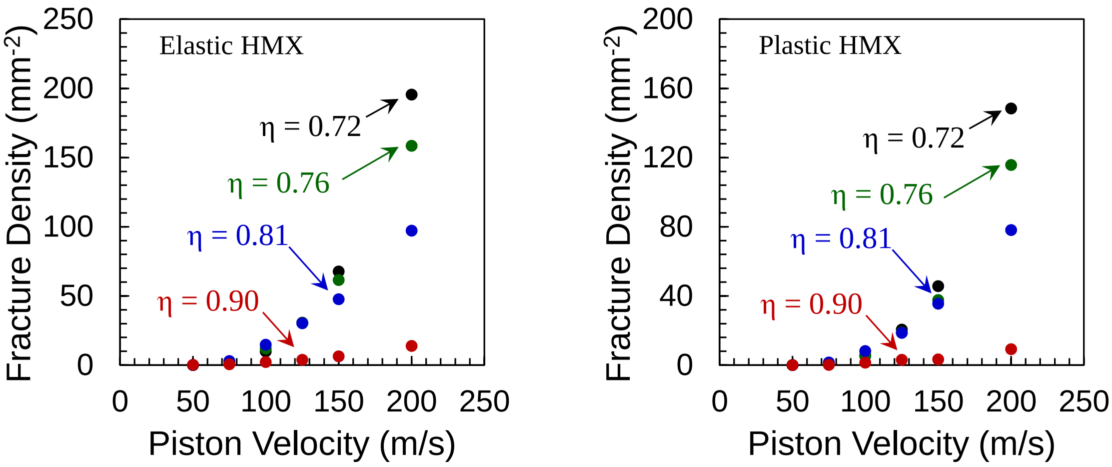

Figure 31. Density of binder fracture sites per mm^2 of specimen as a function of velocity and HMX packing fraction.

3.6.2 Debonding Between HMX and Estane

The most common type of damage observed for all microstructure types and all piston velocities is debonding between the HMX particles and the Estane binder. Intuitively, this response is reassuring because the most severe stress and strain gradients in a heterogeneous composite occur at the interfaces between two-phases with significantly different mechanical behaviors. Figure 32 shows the debond density for both the elastic and plastic HMX specimens as a function of piston velocity from 50 to 200 m/s and packing fractions from 0.72 to 0.90.

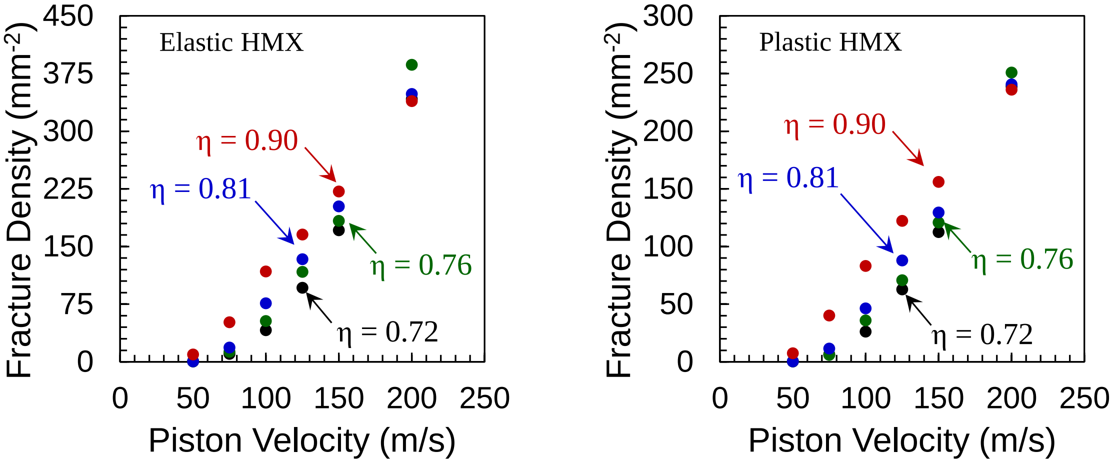

Figure 32. Density of debonding sites per mm^2 of specimen as a function of velocity and HMX packing fraction.

Like the binder fracture density, the debond density for a packing fraction of 0.90 behaves in a different manner than all of the lower packing density cases. Figure 32 shows that for packing fractions between 0.72 and 0.81, the debond density increases more than linearly (concave up) as a function of piston velocity, but the debond density for the 0.90 packing fraction specimens increases less than linearly (concave down) with piston velocity. At low velocities, the debond density increases with packing fraction, but due to the difference in the dependence upon piston velocity, the 0.90 packing fraction material has the least amount of debonding of any microstructure set for both the elastic and plastic HMX specimens. The availability of plastic deformation reduces the amount of debonding by between 30 and 40% depending on the packing fraction and piston velocity. The significant decrease in debonding sites in the plastic HMX specimens greatly decreases the potential locations for energy localization along grain boundaries.

3.6.3 HMX Fracture

The final type of damage explicitly modeled is intragranular fracture of the HMX particles. When large HMX grains cleave along continuous paths (long cracks), the material on either side of the crack is heated, contributing to much larger, continuously connected heated regions. Figure 33 shows the intragranular fracture density for both material types, all piston velocities, and all packing fractions. In general, the fracture density in the HMX is related to velocity and packing fraction in much the same way as debonding density. Namely, the density of HMX fracture increases more than linearly with piston velocity and monotonically with increased HMX packing fraction. Of all of the fracture types, the intragranular fracture mode shows the most effect from introducing plasticity to the HMX particles. Viscoplasticity in the HMX causes a reduction in intragranular fracture of between 69 and 79%, depending on the packing fraction and loading intensity.

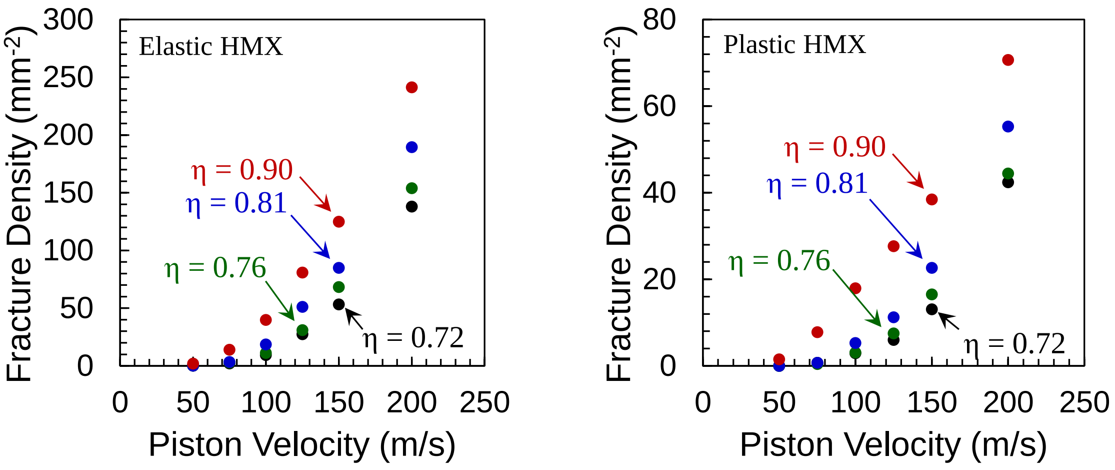

Figure 33. Density of intragranular fracture sites per mm^2 of specimen as a function of velocity and HMX packing fraction.

3.7 Conclusions

This primary focus of this chapter has been to quantify the effect of viscoplastic HMX on the total material response of a PBX composite subjected to a range of constant velocity, piston-driven loads. This has been accomplished by means of analyzing the kinematic, mechanical, thermal, dissipative, and damage behaviors of identical sets of PBX specimens having either elastic or viscoplastic HMX grains. In each of these five areas, the viscoplastic HMX significantly influences the response of the PBX composites.

Results have shown that the viscoplastic HMX does not affect the bulk or average velocity profile. However, the viscoplastic HMX significantly reduces the magnitude of the fluctuations in the velocity field of the PBX specimen. This indicates that the plasticity has a homogenizing effect over the range of piston velocities studied. At present, it has not been possible to validate the kinematic response of the PBX specimens due to an inability to model the exceedingly high strain rates which exist in shock loading experiments. Such an effort to validate this portion of the computational framework is ongoing.

Analysis of the effect of viscoplastic HMX on the mechanical response of PBXs has shown that the introduction of viscoplastic HMX causes an increase in both the longitudinal and hydrostatic stresses induced in the PBX while simultaneously decreasing the magnitude of the von Mises stresses in the HMX grains. In addition, the average longitudinal stresses behind the stress wave front are shown to be in good agreement with experimental results in the range of 50 to 300 m/s impact loading. This quantitative agreement of the induced stress state is a marked improvement over previously published research performed using a similar CFEM framework [70]. This correspondence with experimental data also provides solid validation for the mechanical and damage responses of the PBXs under this type of non-shock loading.

The thermal response of the PBX specimens having viscoplastic HMX is characterized by a significant reduction in average heating, peak temperature rise, and the number or amount of material experiencing localized heating (hotspots). This reduction in heating is found to be accomplished through the mechanism of greatly reducing the density of fracture sites of all three potential types: intragranular fracture density is reduced by about 75%, the density of debonding between the HMX and binder is reduced by 35%, and fracture within the binder material is reduced by 23%. It is believed that the reduction in von Mises stresses in the viscoplastic HMX acts to limit the driving forces which lead to fracture and, once fractured, contribute to frictional sliding. Acting in concert with reduced driving forces, the increased hydrostatic stresses due to viscoplasticity further reduce the sliding friction by increasing the driving force required to initiate sliding.

The results in this chapter clearly indicate that viscoplastic HMX acts on the material system to limit shear stresses (as measured by the von Mises equivalent stress), damage, and dissipation. It should be noted that this analysis covers non-shock loading with piston velocities ranging from 50 to 200 m/s leading to axial stresses up to approximately 1 GPa only. As the loading velocity increases and the ramp time of the curve is reduced into a shock loading event, it is likely that viscoplastic dissipation in rapidly deforming, highly localized regions will begin to dominate the thermal response of the PBX.

CHAPTER 4: EFFECT OF VISCOPLASTICITY ON IGNITION SENSITIVITY

In the evaluation of an energetic material and evaluating its usefulness, it is necessary to meet specifications for both performance (explosive output) and sensitivity. It is crucial to understand the loading conditions under which a specimen will ignite both intentionally and unintentionally. Often, the determination of an explosive involves testing a number of specimens using a consistent experimental setup but varying the amplitude of the loading until a number of ignition and non-ignition results are obtained [3, 43, 59]. In order to quantify the ignition sensitivity of various explosive materials and experimental techniques, analytical descriptions of the threshold distinguishing between ignition and non-ignition events are developed. Walker and Wasley [15] proposed a critical input energy criterion specifically for use with heterogeneous explosives in response to flyer plate impact. Over time, modifications to this criterion have been implemented to extend the regime of applicability to include rod impact [40], spherical impactors [2], and other loading geometries [41, 42]. Eventually, James [42] modified the form of the Walker and Wasley criterion to include terms explicitly defining a minimum input energy threshold and a measure of the minimum velocity capable of igniting the material. The updated critical energy criterion (subsequently referred to as the H-J criterion) has been used with much success to describe the critical thresholds for a wide range of explosive formulations, input pressures, and projectile geometries.

The focus of this chapter is to fully quantify the effect of viscoplastic HMX on the ignition sensitivity and critical velocity threshold of a two-phase PBX. Not only will this work distinguish between ignition and non-ignition events, but the relative sensitivity of igniting samples is also evaluated. This is accomplished through the utilization of a three step process coupling deterministic analysis of mechanical processes, local analysis of the resulting temperature field, and a probabilistic treatment of the stochastic variation in the results. The CFEM calculations of Chapter 3 explicitly determine the mechanical and thermal response of a range of PBXs to constant velocity, piston driven loading. From the results of the CFEM analysis, the resulting temperature fields are investigated for the presence locally intense regions of heating (hotspots) capable of exceeding a chemically-derived criticality condition. The effect of viscoplastic HMX on the random fluctuations or stochasticity in the predicted times to ignition is evaluated by the use of Weibull distribution function to describe the probability of ignition of a randomly selected specimen subjected to a given load intensity and duration. Finally, the effect of viscoplastic HMX on the safe threshold velocity and the critical input energy as calculated by the $P^2\tau = \text{constant}$ relation [15] and the H-J criterion are investigated.

4.1 Methodology

The calculations performed in this chapter concern the ignition sensitivity of two-phase (HMX and Estane) polymer bonded explosives (PBX) under the influence of a piston compressing the material at a constant velocity. The CFEM micromechanics calculations for these microstructures and loading conditions are carried out and discussed in detail in Chapter 3. This analysis of ignition sensitivity focuses on the evolution of the temperature field of each specimen, as calculated in Chapter 3. The region of interest in each specimen is the material that is within 7.5 mm of the piston at the moment of impact, or half of the total domain of the specimens used by the CFEM analysis. This results in a region that is initially 7.5 mm long by 3 mm wide prior to being compressed by the stress wave. For each microstructure ($\eta = 0.72 - 0.90$) and piston velocity ($v = 50 - 200\ \text{m/s}$) analyzed in Chapter 3, the Tarver criticality condition shown in Figure 34 is applied as a material property for the HMX phase of the PBXs. Any specimen having a single critical hotspot within the 8 μs load duration of the calculations is said to ignite. If ignition occurs, the load duration required to cause ignition is calculated as the “time to criticality”. The statistical distribution of times to criticality within each specimen set is analyzed using the Weibull distribution function to analytically represent the probability that a randomly generated microstructure morphology with the same size and characteristics will ignite if subjected to a given load duration.

Finally, three methods are used to quantify the sensitivity of the PBXs and the minimum velocity required to ignite the materials is calculated. First, the probability that a specimen will ignite is calculated for all piston velocities and a Weibull distribution function of the form described in Chapter 2.3.2 is fit to the data to identify both the threshold velocity and the velocity at which half of the specimens are expected to ignite. The second method used to quantify the sensitivity of the PBXs is a modified version of $P^2\tau = \text{constant}$ critical energy criterion proposed by Walker and Wasley [15]. Lastly, the ignition sensitivity data is compared to the H-J relation [11].

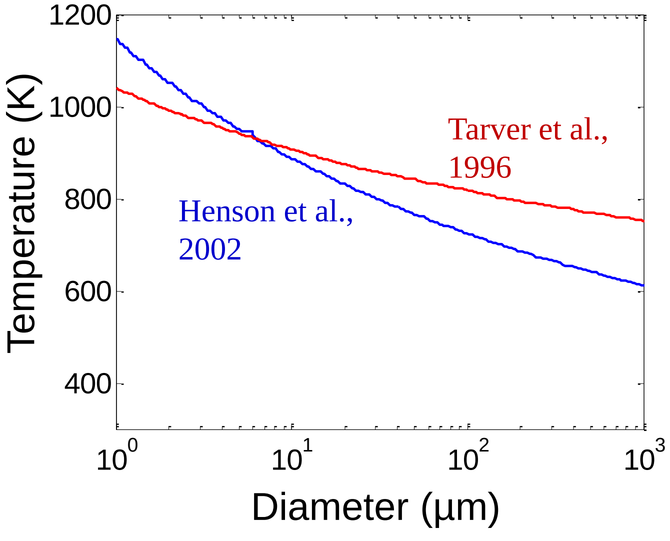

Figure 34. Tarver criticality condition based on the minimum hotspot size and temperature required for thermal runaway.

4.2 Quantification of the Predicted Ignition in PBXs

4.2.1 Ignition Sensitivity

The ignition sensitivity for each microstructure and loading intensity is quantified in this analysis by calculating the time to criticality from the threshold described in Chapter 2.3.1 derived from the work of Tarver et al. [38]. In general, the specimens which require a shorter loading duration to generate a critical hotspot are said to be “more sensitive” than microstructures and loading conditions requiring a greater duration of loading to generate a critical hotspot. In addition to those specimens that generate critical hotspots, there are specimens which fail to generate a critical hotspot in the first 8 μs of loading. It is at this time (8 μs) that the wave front reflecting from the far boundary begins to interfere with the results, and the calculations are terminated. All specimens which do not ignite prior to 8 μs are said to not ignite.

For piston velocities generating a significant number of ignition events, it then makes sense to analyze the difference in sensitivity among the ignited specimens using the loading time required to cause critical behavior. Figure 35 shows the probability that a specimen having between 72 and 81% HMX by area will have generated a critical hotspot as a function of load duration. Results are shown for impact velocities for which greater than 40% of the microstructures ignite. Specifically, Figure 35 shows the times to criticality for piston velocities of 200 m/s (black), 150 m/s (blue), and 125 m/s (red). The curves in the figure correspond to the fit of the critical time data to a Weibull distribution function. For the specimens loaded at 125 m/s, between 40 and 95% ignition was observed. Therefore, the Weibull function is fit to the available data with the assumption that the remaining specimens ignite after 8 μs.

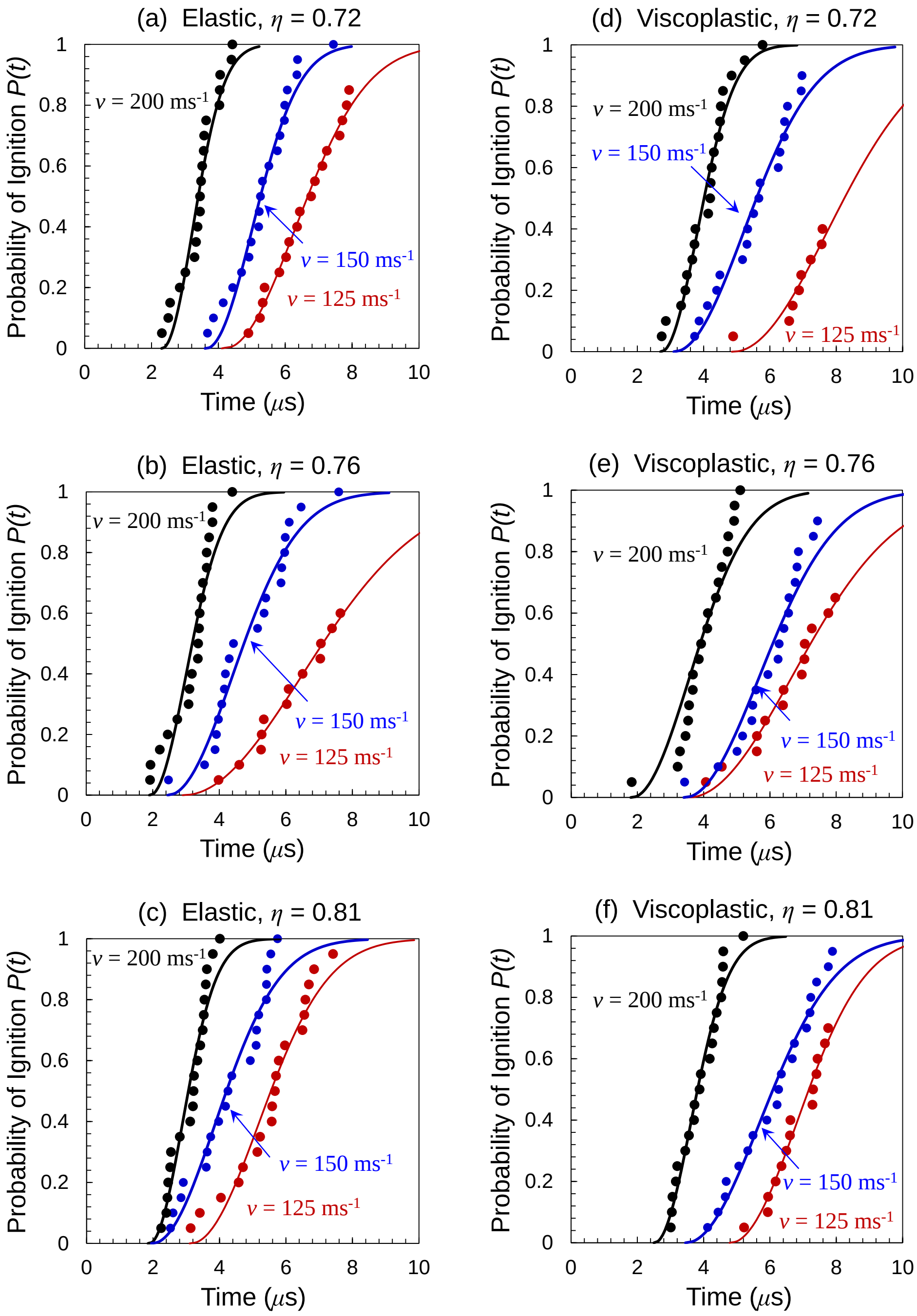

Figure 35. Cumulative probability of ignition in PBX specimens. The times to ignition for all specimens are marked by data points and the analytical fit to the Weibull distribution function for each set is shown by a solid line. Data are presented for HMX packing fractions from 0.72 to 0.81 for both (a-c) elastic HMX and (d-f) plastic HMX specimens. The results for all piston velocities causing more than 2 critical hotspots are (black) 200 m/s, (blue) 150 m/s, and (red) 125 m/s.

The Weibull representation of the ignition sensitivity data obtained from the CFEM calculations provides a mechanism for direct comparison of the response of different microstructures and loading conditions. The three Weibull parameters used here to discuss the relative sensitivity of the PBXs are the threshold time to ignition t_0 , the mean time to ignition t_{50} , and the range of potential critical times t_{range}. Figure 36, Figure 37, and Figure 38 show the dependence of t_0, t_{50}, and t_{range}, respectively, on piston velocity and HMX packing fraction for both the (blue) elastic and (red) plastic HMX specimen sets. Interestingly, the threshold time (and t_{50}, t_{range}) is not a significant function of HMX packing fraction, therefore when quantifying the effect of piston velocity and plasticity on t_0, t_{50}, t_{range}, the various packing fractions will be considered together. This observed response of HMX packing fraction having no significant effect on the sensitivity of the PBX echoes the experimental findings of Chidester et al. [3]. Chidester et al. performed a series of Stevens impact tests on a wide range of pristine and aged PBX compositions using two types of impactor geometry. While the focus of the work was to differentiate the sensitivity of new and pristine PBX specimens, the authors have only minimal discussion concerning the difference in sensitivity among the various compositions. For example, velocity thresholds are presented for specimens of LX-14 (95.5wt% HMX, 4.5wt% Estane), LX-10-1 (94.5wt% HMX, 5.5wt% Viton A), LX-04 (85wt% HMX, 15wt% Viton A), and PBX 9501 (94.9wt% HMX, 2.5wt% BDNPA-F, 2.5wt% Estane, O.lwt% DPA or Irganox). The range of threshold velocities for these compositions is only 35 to 45 m/s. These ranges presented for the threshold velocity of these four compositions all have an overlapping region from 40 to 41.2 m/s, indicating that the threshold or safe velocity is not significantly dependent on the HMX packing fraction of the composition.

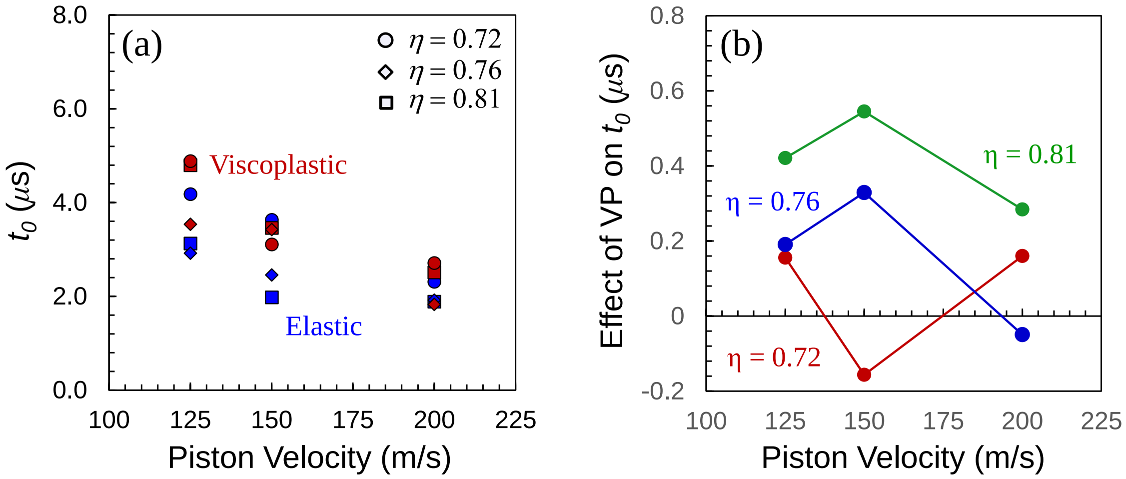

Figure 36. (a) The threshold time to ignition as a function of piston velocity and HMX packing fraction and (b) the effect of viscoplasticity on the threshold time over the same range of velocity and packing fraction.

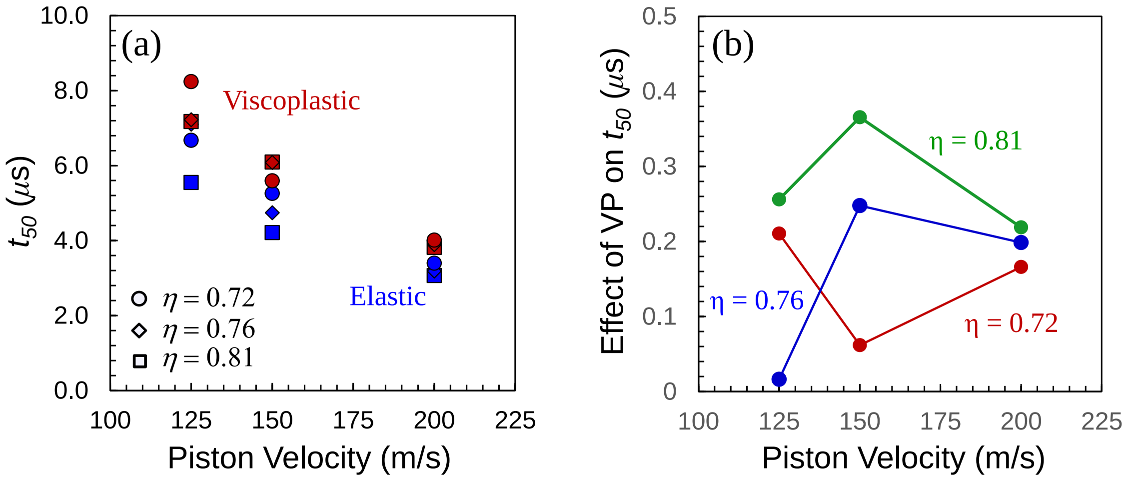

Figure 37. (a) The mean time to ignition as a function of piston velocity and HMX packing fraction and (b) the effect of viscoplasticity on the mean time to ignition over the same range of velocity and packing fraction.

In general, the results show that t_0, t_{50}, and t_{range} all decrease as a function of piston velocity. For the plastic HMX microstructures, the threshold time decreases from

4.4 μs to 2.35 μs as the impact velocity increases from 125 to 200 m/s, a 46.7% reduction in the minimum time required to form a critical hotspot. Comparing the threshold times of the elastic and plastic HMX specimens shows that the effect of plasticity is to increase the time to criticality. This effect of increasing t_0 due to plasticity is greatest at 125 m/s (25.6% increase) and decreases as the piston velocity increases to 200 m/s (13.1% increase). The mean time to criticality is the least sensitive measure to the number of specimens. Figure 37 shows the mean time to ignition for each microstructural and loading intensity. Similar to t_0, t_{50} decreases monotonically as a function of piston velocity and exhibits an increase in mean time to ignition due to HMX plasticity. As the piston velocity increases from 125 to 200 m/s, t_{50} decreases from 6.4 μs to 3.2 μs (50% decrease) for the elastic HMX specimens and from 7.5 μs to 3.9 μs (48% decrease) for the plastic HMX specimens. The effect of viscoplasticity on t_{50} is to increase the mean time to ignition by between 16 and 22%, as compared to the elastic HMX specimens.

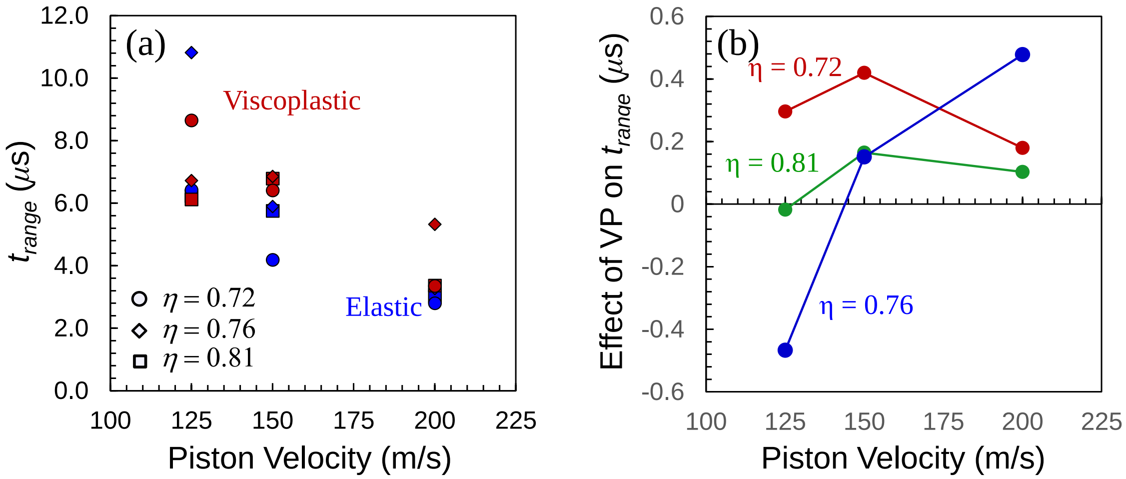

Figure 38. (a) The range of potential times to ignition as a function of piston velocity and HMX packing fraction and (b) the effect of viscoplasticity on the range of critical times over the same range of velocity and packing fraction.

The effect of both impact velocity and viscoplasticity on the range of critical times can be seen in Figure 38. For piston velocities from 125 to 200 m/s, t_{range} decreases from 7.8 to 3.0 μs (61.2% reduction) for specimens with elastic HMX and from 7.2 to 4.0 μs (44.0% reduction) for the plastic HMX specimens, The effect of plasticity on the range of critical times is different in nature than the effect of plasticity on either t_0 or t_{50}. For both t_0 and t_{50}, the effect of plasticity is to delay the ignition, thereby desensitizing the PBX specimens, regardless of the piston velocity. However, the effect of plasticity on t_{range} acts to reduce the range of critical times by 6.3% at 125 m/s, but increases the range of critical times by 24.5% and 25.3% at 150 and 200 m/s, respectively.

4.3 Distribution of Hotspot Generation

In the previous section, the ignition sensitivity was quantified in terms of a “go / no-go” type analysis and by studying the change in the characteristics of the Weibull representation of the probability of ignition versus time results due to piston velocity, HMX packing fraction, and HMX material description. In order to understand the spatial distribution of hotspots as well as the temporal distribution, the position of critical hotspots is quantified and is used to describe the local behavior of nucleating hotspots. Figure 39 and Figure 40 show the distance of critical hotspots from the piston as a function of the time required for the hotspot to form for piston velocities from 125 to 200 m/s. Figure 39 provides the overall picture of hotspot generation as a function of piston velocity for both the (left) elastic and (right) viscoplastic HMX specimens. Qualitatively, it is clear from this figure that there is a delay time before which no specimens ignite and that following the delay time, there is a limited region within which that hotspots will be created. How is this region defined? Logically, it is apparent that all hotspots must occur between the face of the piston and the farthest extent of the elastic stress wave in the specimen. In order to quantify the region of material generating hotspots, Figure 40 shows a dashed line corresponding to the average composite wave speed for this material and offset from the origin by a constant delay time t_d.

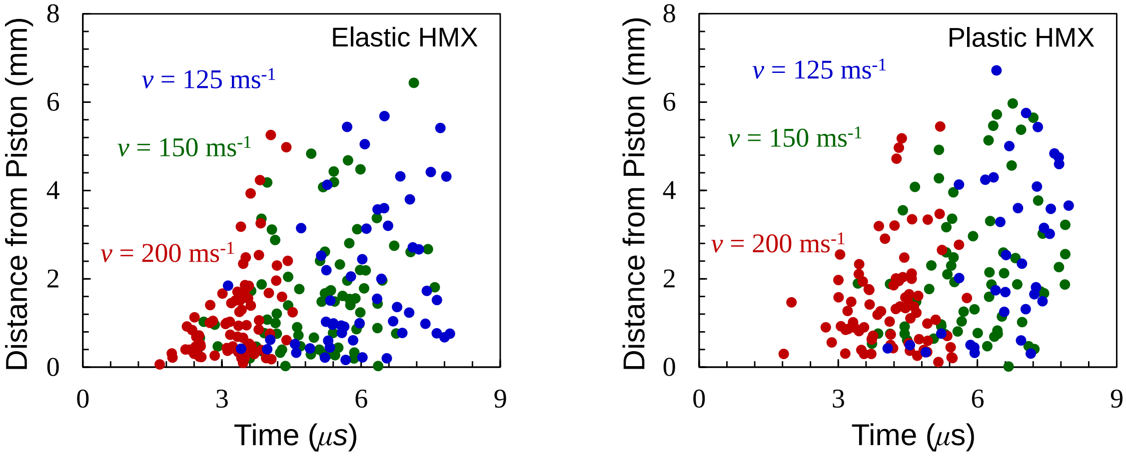

Figure 39. Location of critical hotspots in (left) elastic and (right) plastic HMX specimens.

In Figure 40, the hotspot location data is separated by piston velocity to directly compare the effect of viscoplastic HMX on the spatial distribution of critical hotspots. The increase in delay time for decreasing piston velocity is readily perceived as a gap between the composite wave speed line and the data in each figure. In order to quantify the location of the hotspots as a function of velocity, three measures are used: average hotspot location, the delay time (t_d), and the frequency distribution of hotspots as a function of distance from the piston. It is important to point out that the discussion of the spatial distribution of hotspots considers only the first critical hotspot generated in any given specimen.

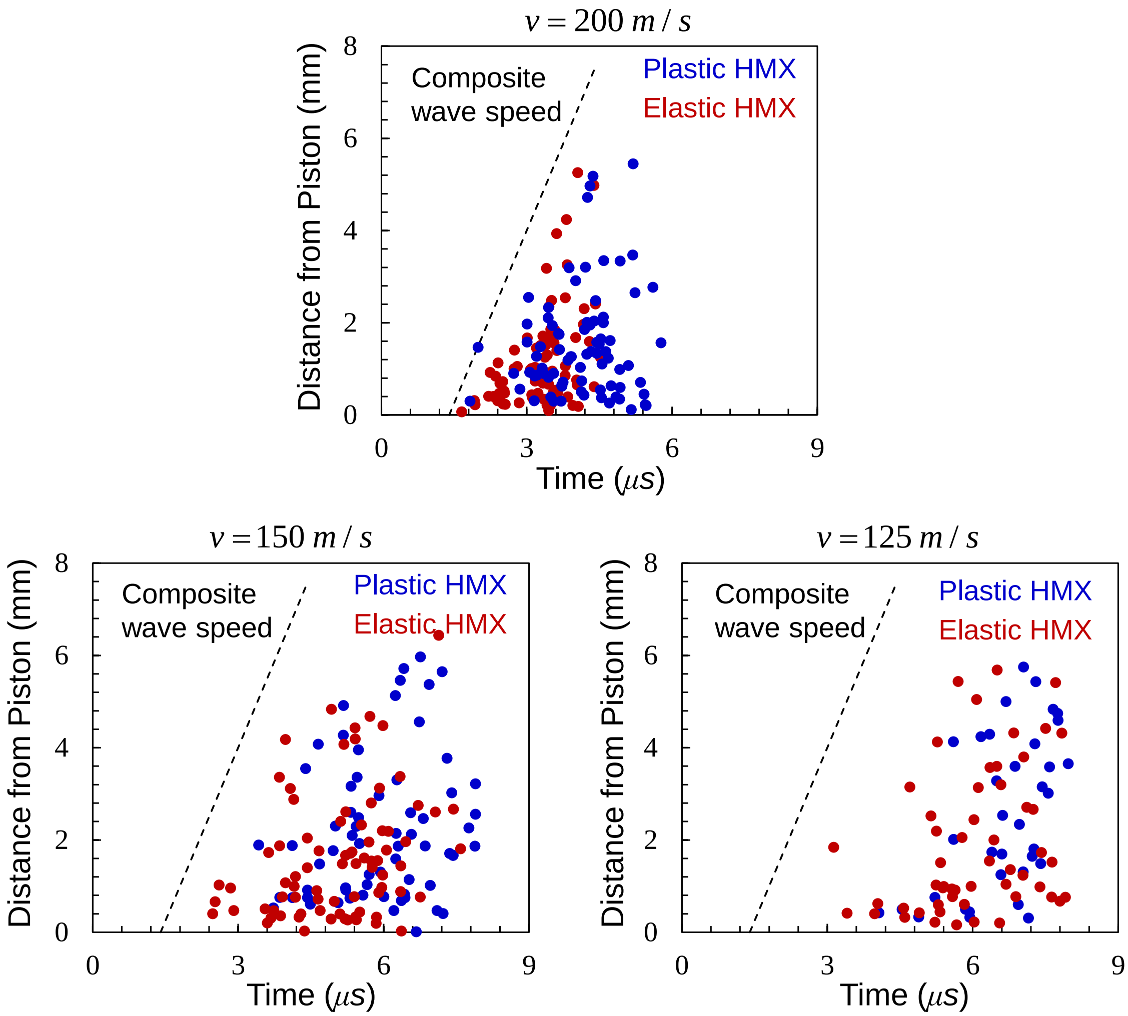

Figure 40. Location of critical hotspots as a function of critical time for piston velocities from 125 to 200 m/s.

The average location of first critical hotspots provides a good measure of the general trends concerning the change in hotspot distribution as a function of velocity and material description. The results show that the average hotspot location decreases from 1.91 mm to 1.17 mm from the piston for the elastic HMX specimens as the piston velocity increases from 125 to 200 m/s and from 2.67 mm to 1.52 mm from the piston for plastic HMX specimens under the same loading conditions. This indicates that, for the range of piston velocities studied, specimens whose HMX grains behave in an elastic manner are likely to generate hotspots between 22 and 28% closer to the piston face than the same microstructure with plastic HMX grains. Figure 41 shows the delay time as a function of piston velocity for both the elastic and plastic HMX cases. For both material types, there is a clear reduction in delay time with increasing piston velocity. This decrease in delay time corresponds to the critical hotspots initiating closer to the immediate passage of the stress wave front. The imposed boundary conditions specify a ramp time of 0.5 μs prior to reaching the nominal piston velocity, thereby creating a wave structure that begins with a wave rise time of 0.5 μs and gradually increases with propagation distance. The results indicate that critical hotspots generate in the PBX material after the passage of the wave front. Specifically, at piston velocities up to 200 m/s, the hotspots require additional heating behind the stress wave front in order to transition into a spot capable of thermal runaway. If the trend of decreasing delay times extrapolated along the line of best fit, it is possible to estimate the velocity at which hotspots will begin to be generated within the rise time of the wave. The velocity required for initiation of hotspots within the wave front is 308 m/s for the elastic HMX specimens and 226 m/s for the plastic HMX specimens, a difference of 82 m/s (30%).

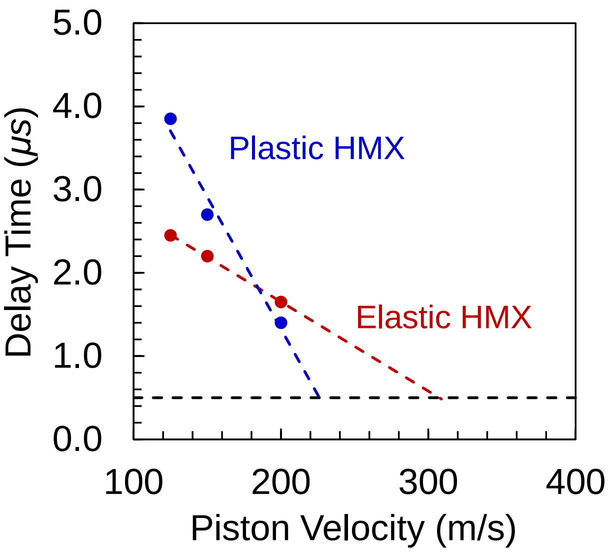

Figure 41. Delay time as a function of piston velocity for (red) elastic and (blue) plastic HMX specimens.

Now, where the average hotspot location describes the mean location of hotspots and the delay time measures the closest hotspot to the passing stress wave front, the relative frequency distribution quantifies the location of all hotspots in each loading condition. Figure 42 shows the relative frequency distribution of critical hotspot location for both material types for piston velocities from 125 to 200 m/s. For all piston velocities and both elastic and plastic HMX, the peak density of hotspots occurs within a millimeter of the piston face. Beyond this, there are distinct differences between the various loading and microstructure conditions. At high piston velocities, the first critical hotspots are much more concentrated near the impact face, but as the piston velocity decreases, it can be seen that the distribution contains significant numbers of hotspots far from the piston. At 200 m/s, 70% of the hotspots in the elastic HMX specimens and 60% of the hotspots in the plastic HMX occur within 1.5 mm of the piston while only 52% and 32% of the hotspots generated at 125 m/s occur within this range for the elastic and plastic HMX specimens, respectively. Analogous to this, it can be clearly seen that lower piston velocities contain many more hotspots at a distance of 4 mm from the piston in Figure 42. The specimens loaded at 125 m/s have 14% (elastic) and 30% (plastic) of the critical hotspots at least 4 mm from the piston. As the piston velocity increases, the proportion of hotspots at least 4 mm from the piston steadily decreases to only 3% of the hotspots in elastic HMX and 5% of the hotspots in the plastic HMX. The effect of plasticity on the spatial distribution of critical hotspots is seen to be significant as well. Viscoplasticity in the HMX causes the likely location of critical hotspots to shift away from the piston in much the same way that decreasing velocity does. The specimens with viscoplasticity generate 25% fewer hotspots in the 1.5 mm nearest the piston, relative to elastic HMX specimens. In addition, the viscoplastic specimens generate 76% more first critical hotspots more than 4 mm from the piston. The significance of this change in the distribution of critical hotspots is that the maximum hotspot density (number of hotspots per mm depth) is reduced in the presence of viscoplasticity. In the framework of the analysis presented here, the density of hotspots does not play a role in the determination of whether or not a specimen ignites, but the concept that hotspot density is a critical factor in the growth of a hotspot (or distribution of hotspots) into a deflagration or detonation event is central to the work in [8, 71]. The fact that the effect of viscoplasticity is similar in nature to the effect of reducing the loading intensity provides evidence in support of the idea that viscoplasticity in the HMX grains lowers the ignition sensitivity of the PBX containing it.

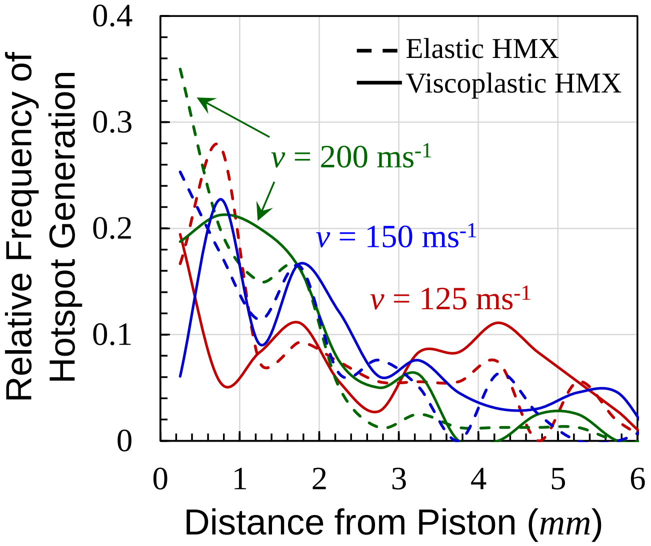

Figure 42. Distribution of critical hotspots in specimens loaded by piston velocities ranging from 125 to 200 m/s.

4.3.1 Adjustment to Critical Ignition Times Accounting for Wave Transit

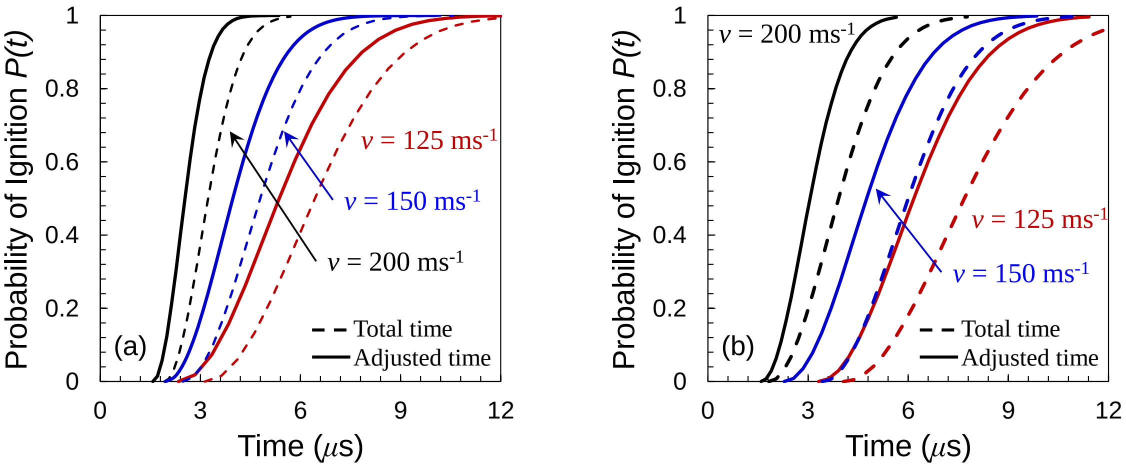

Figure 43. Adjusted and total critical time Weibull distributions for piston velocities ranging from 125 m/s to 200 m/s for Figure 43(a) elastic HMX and (b) plastic HMX specimens.

Now that the spatial distribution of critical hotspots has been thoroughly quantified, the location of the individual hotspots will be used to determine the duration of load required to generate each spot. In order to determine the duration of load required at each hotspot in order to cause thermal runaway (referred to below as the adjusted time, t_a), the transit time of the composite elastic wave from the piston to the hotspot is subtracted from the critical time calculated above. Figure 43 compares the adjusted and total time Weibull distributions for both the (a) elastic HMX and (b) plastic HMX specimens. The adjusted time Weibull distributions provide a measure of the variation of local heating rate at the critical hotspots of the various specimens. For example if the heating rate for all critical hotspots is exactly the same, the adjusted time Weibull distribution would collapse into a vertical line at t_a. As the adjusted time Weibull becomes increasingly vertical, the likelihood increases that a single rate-controlling mechanism is generating the majority of the nucleated hotspots. Conversely, as the adjust time Weibull becomes broader, the likelihood increases that multiple mechanisms leading to significantly different heating rates are present in a given regime. Table 4 lists the parameters of $t_0, t_{50}, \text{and } t_{range}$ for the adjusted time Weibull distributions describing the heating rate of both the elastic and plastic HMX specimens. The threshold time and mean time to criticality are consistently higher in the specimens with plastic HMX, indicating that the presence of viscoplastic deformation at these rates actively decreases the local heating rate at future critical hotspots.

Table 4. List of the parameters for the adjusted time Weibull distributions.

Piston Velocity	t_0		t_{50}		t_{range}	
	Elastic	Plastic	Elastic	Plastic	Elastic	Plastic
125 m/s	2.34	3.31	5.36	6.17	8.00	7.50
150 m/s	1.96	2.29	3.97	4.76	5.40	6.44
200 m/s	1.57	1.59	2.54	3.06	2.52	3.75

4.4 Sensitivity Thresholds

The spatial and temporal distribution of critical hotspot generation has been quantified and analyzed. Utilizing the Weibull distribution function, the ignition sensitivity of PBXs has been discussed in terms of threshold time to criticality, mean time to criticality, and the range of times which encompasses the transition from a “completely safe” loading scenario to one that will “always” ignite. However, in order to be able to compare the ignition sensitivity as calculated here to experimental sensitivity measurements, the results must be recast into a form that is meaningful in terms of experimentally measurable quantities. In this section, three methods for discussing ignition sensitivity are introduced. First, the probability that a specimen will ignite at a range of impact velocities is used to predict a threshold velocity and “expected” velocity for ignition. The other two sensitivity measures are based upon the concept of critical input energy. A form of the so called $P^2\tau = \text{constant}$ relationship introduced by Walker and Wasley [15] is used here to compare the sensitivity of the specimens with elastic and plastic HMX and in Chapter 6 to evaluate the relative sensitivity of the proposed “aluminum bonded explosives. Finally, the criterion proposed by James [11] is unsuccessfully applied to the current results.

4.4.1 Criticality as a Function of Piston Velocity

In Chapter 3, a sets of twenty microstructural instantiations of various HMX packing fractions are loaded with piston velocities ranging from 50 to 200 m/s. The resulting temperature distribution is analyzed as described in this chapter to identify the first critical hotspot leading to thermal runaway in each individual specimen. For each piston velocity, some proportion of the tested microstructures reaches ignition by way of a single instance of thermal runaway. At 50 m/s, there were no specimens for either the elastic or plastic HMX cases that ignite, and at 200 m/s all specimens from both the elastic and plastic HMX cases ignite. In this way, this range of piston velocities captures the whole regime in which there is some uncertainty as to whether a specimen will ignite. By bracketing the response regime of interest and testing the material at a range of intermediate velocities, it is possible to build a statistical likelihood of ignition under the current loading and boundary conditions.

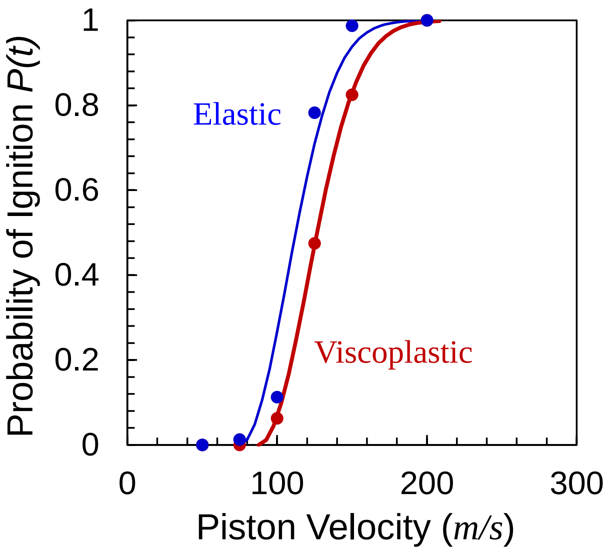

Figure 44. Probability of ignition of the PBX specimens as a function of impact velocity.

Figure 44 shows the fraction of microstructures (regardless of HMX packing fraction) that ignite for each piston velocity studied. Due to the similarity in the form of the response, the data is fit to a Weibull distribution function where the fitting parameter t_0 is now the threshold velocity v_0. Analysis of the data in this form provides a convenient way to directly compare the effect of HMX viscoplasticity on the ignition sensitivity of the PBX of interest. From the results in Figure 44, the predicted threshold velocity for the specimens with elastic HMX is 75 m/s and the threshold for the plastic HMX specimens is 88 m/s. The velocity corresponding to a 0.5 probability of ignition is 112 m/s and 127 m/s for the elastic and viscoplastic HMX specimens, respectively. In terms of these two measures of ignition sensitivity, the introduction of viscoplastic deformation into the HMX grains causes an increase in the threshold velocity of 13 m/s (16.9%) and an increase in the median velocity of 15 m/s (12.7%).

Using this approach, an estimated value of the threshold velocity is found to be 88 m/s (for the plastic HMX specimens). Experimental determination of the threshold velocity of PBXs similar in nature to those presented here has been performed by Chidester et al. [3]. In that work, a series of Stevens tests are performed on a range of explosive compositions with HMX as the primary constituent, resulting in a threshold below which no reaction is detected. The safe velocity thresholds determined by Chidester et al. fall in the range of 35 to 45 m/s. The two compositions outside of this range are PBX 9404 which is more sensitive due to its energetic binder (nitrocellulose) and a low density pressing of PBX 9501 that was less sensitive (velocity threshold range of 43.3 - 53.4 m/s). The experimentally obtained threshold range of 35 to 45 m/s is approximately half of the threshold calculated here. One potential reason for this discrepancy is the difference in loading or boundary conditions. For a Stevens test, a projectile is launched into a confined specimen. If reaction is detected, the test is described as a “go” for ignition. This means that the stress wave that propagates through the material may reflect off of the confining back wall prior to the initiation of the hotspot. In the vicinity of this reflection, the stresses are much more intense (the axial stress increases by up to 100%) than those experienced by the material during the first wave pass through the material. In this analysis, no wave reflection is permitted and therefore only a single wave pass is considered. Therefore, the material conditions in the vicinity of the rear confining wall in a Stevens test experiences loading rates and intensities similar to those present in a single wave transit for a piston speed twice as high. In this way, the current analysis is in good agreement with the experimentally determined thresholds of Chidester et al. in order to further validate this method and to more faithfully match the boundary conditions of the experiments, future simulations should be performed which explicitly model the projectile and the confinement of the specimens, allowing for full wave reflection.

4.4.2 Criticality as a Function of Axial Stress

The previous approach explicitly considers only the piston velocity and the proportion of specimens which ignite under those conditions. Implicitly, however, this analysis is potentially flawed in that “ignition” in this case is said to occur if a specimen has any critical hotspots prior to wave reflection from the far boundary of the specimen, introducing a constant time $t = 8\,\mu s$ in which the ignition must occur. As such, it is advantageous to utilize a critical threshold which explicitly relates the load duration and the load intensity. Namely, the $P^2\tau = \text{constant}$ relationship proposed by Walker and Wasley [15] to capture experimentally observed ignition phenomena is modified here as

$$\sigma_{yy}^2 t_{50} = c\,. \tag{66}$$

where σ_{yy} is the effective longitudinal stress as discussed in Chapter 3.3, t_{50} is the mean time to criticality presented earlier in this chapter, and c is a constant for each material type. Figure 45 shows the effective axial stress versus the mean time to criticality for all of the microstructure and loading scenarios presented in Chapter 3. The results for both the elastic and plastic HMX specimens are then fit to determine the value of *c* that best represents the data. This type of critical input energy approach appears to correspond well to the data and provides a convenient method for the relative comparison of sensitivity. In Figure 45, any event lying to the left of the dashed lines is a non-ignition event and anything falling to the right of the dashed lines indicates a likely ignition event. As such, the more sensitive that a particular formulation is, the farther to the left that it will appear in this axial stress - t_{50} space. The results shown here are in agreement with the earlier methods of describing and quantifying the ignition sensitivity and indicate that the specimens containing plastic HMX are clearly less sensitive in this loading regime than the corresponding specimens with elastic HMX.

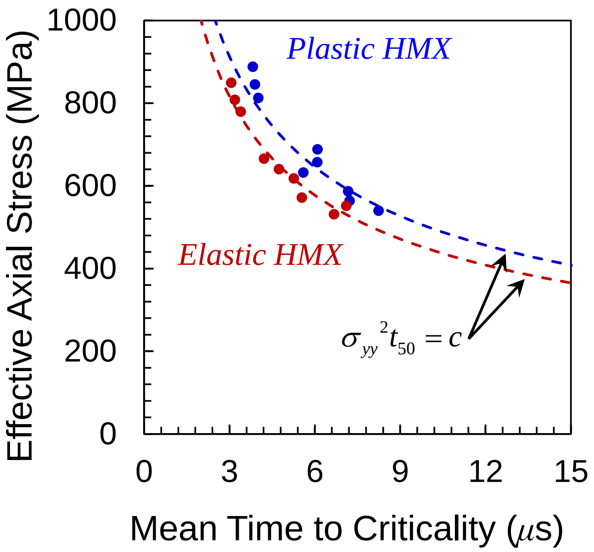

Figure 45. Critical threshold relationship in terms of applied axial stress and load duration required for ignition shows a decrease in sensitivity due to the presence of viscoplastic deformation in the HMX.

4.4.3 Criticality as a Function of Input Energy

Building off of the critical energy criterion of Walker and Wasley [15], James [11] presented a modified critical energy criterion that is applicable to a wide range of material systems and loading scenarios. The concept for this method arises from the apparently asymptotic nature of sensitivity results at both high and low velocity extremes. James [11] noted that the existing data across a wide spectrum of conditions tended to require a minimum amount of energy in order to ignite, regardless of the amplitude of the loading. Secondly, James identified that there also seems to exist a particle velocity below which no ignition will occur, no matter how long the load is maintained. Utilizing these two concepts, what is now referred to as the H-J relation takes the following form.

$$\frac{E_c}{E} + \frac{\Sigma_c}{\Sigma} = 1 \tag{67}$$

In this expression, E_c is the “trigger” energy required for ignition to occur, Σ_c is a measure of the kinetic energy (velocity) below which no ignition can occur, E is the input energy, and $\Sigma = {v^2}/{2}$.

Figure 46 shows the critical input energy as a function of Σ for specimens containing plastic HMX. The dashed line corresponds to the H-J relation that generally passes through the data. It should be noted that the specific values in this H-J relation are not fit to the data in the figure. Due to the apparent disconnect between the trend defined by the H-J relation and the criticality data from this study, a representative curve has been reproduced that passes through the data in order to clearly illustrate the fundamental differences observed between this data and the H-J relation. Figure 46 indicates that the critical energy required to ignite the material is actually decreasing with decreasing piston velocity. If this behavior is treated as a trend, it would suggest that there exists a piston velocity below which all specimens will ignite, regardless of the input energy. While it is obvious that this particular trend is not physical, it is not immediately apparent why the data on ignition sensitivity in terms of critical energy calculated herein diverges so drastically from the expected form of the H-J relation. Generally, there are two broadly defined issues that are potentially the cause of this unexpected trend in terms of critical energy and piston velocity. The first and most likely issue can be described as a deficiency in the model, and the second potential issue is an incompatibility between the current work and the H-J relation.

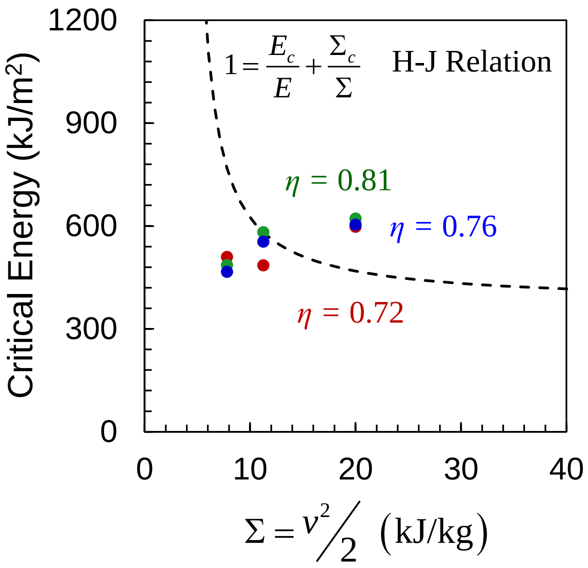

Figure 46. Comparison of results to a HJ relation in terms of critical input energy and piston velocity. Results shown are for the plastic HMX specimens.

The most likely source for the deviation between the commonly observed trend and the calculated response of this analysis is a deficiency in the modelling capability of the presented framework. Within this framework, there are at least three (3) conditions that could lead to inaccuracies between experimental and computational results. (1) Insufficient resolution of the PBX microstructure of interest could lead to migration away from controlling hotspot mechanisms. In the process of microstructure generation described in Chapter 2, it is assumed that the smaller grain size modes are completely absent (or uniformly, continuously dissolved into the binder) from the PBX composition. Recent work by Welle and Molek [43] show that the grain size distribution of HMX in a pressed granular setting can have a significant influence on the sensitivity thresholds due to ignition of thin flyer experiment. In addition to the grain size distribution, the present method of microstructure generation produces specimens containing no void space (100% of the volume is made up of either HMX or Estane). The influence of preexisting pores on the initiation of HMX based explosives has been studied extensively and is shown to be critical in both the localization of energy into hotspots [23] as well as providing a path for the propagation of burning in the HMX [5]. Finally, the use of a structured triangular mesh grid to describe a highly irregular microstructure leads to only marginal geometric discretization of the specific desired grain morphologies, especially on the boundaries. (2) Specimen ignition may require a certain density of “critical” or even subcritical hotspots rather than simply a single “critical” hotspot. The present methodology assumes that a single runaway hotspot is sufficient to ignite the entire specimen. There are two possible reasons that this hypothesis could cause divergence from experimental results. First, it is common for models predicting the processes connecting initiation to deflagration or detonation to consider the effect of the density of hotspots as well as the size and temperature of the most significant hotspot [71]. Secondly, the problem could arise from a difference in what is considered an ignition event. In an experimental setting, an ignition (or “go”) event is often characterized by visible, violent reaction or by the presence of a propagating pressure wave from the reaction processes. However, it seems distinctly possible that local reaction sites may occur internally in a given specimen without leading to observable or readily quantifiable pressure outputs. In this case, temperature rise sufficient to cause the initiation of reaction is present, but the conditions are not favorable to propagate beyond some local region of influence. In this scenario, the material has been damaged by the degradation of its mechanical and future performance capabilities, without the occurrence of complete, large-scale reaction. (3) The magnitude of the temperature rise due to frictional sliding may not be accurate in the vicinity of extreme pressures and extensive fractures. As discussed in Chapter 2, the frictional coefficients for modeling contact between the various constituents are known only to a low degree of certainty. For the purposes of this work, parameters closely agreeing with previous work and experimental investigation have been chosen and their influence on the specimen scale frictional response is minimal. In general, the characteristics of frictional contact are also known to vary as a function of both confining pressure and surface temperature of the material, but for this class of materials, the effect of pressure and temperature have yet to be investigated to provide guidance for the accurate evolution of the frictional behavior with temperature and pressure.

In addition to model inadequacies, if is also possible that the difference between the H-J type response and the behavior exhibited by the specimens tested here is due to problems with the H-J relation or its applicability to the loading conditions considered here. Specifically, the H-J relation is an analytic representation of the global response that is effective over a wide range of load intensity [11]. While this does provide the most useful tool for describing the behavior of the material regardless of the loading scenario, it also precludes the model from the capability of capturing local shifts in dominant hotspot formation mechanism, if any. Finally, the discrepancy between the H-J relation and the computational findings presented here could simply be due to an incompatibility between the loading regime applicable to H-J and the loading condition of this work. The H-J relation is formulated to accurately represent the results from a wide range of impact scenarios including plates, flat-nosed rods, spheres or round-nosed rods, or shaped charge jets. The potential incompatibility arises from the fact that all of these loading scenarios represent shock loading events and the loading conditions of the present work correspond to non-shock loading. Identifying the specific cause of the seeming inconsistency between the results obtained using the current computational framework and those of the H-J type relation is the subject of current and ongoing research.

4.5 Conclusions

This chapter has focused on quantifying three features related to the ignition sensitivity of void and pore free two-phase PBXs containing HMX in an Estane binder.

The first thrust of this chapter has been to characterize the variation in ignition responses determined between statistically similar instantiations of idealized microstructures. The results have shown that for HMX packing fractions ranging from 0.72 to 0.81, the ignition sensitivity as measured by the threshold time, mean time to criticality, and range of critical times is not a function of packing fraction. The variation within the times to criticality of each set of similar microstructures is greater in magnitude than any variation that has been seen due to changes in HMX packing fraction. The one exception to this finding are the ignition sensitivity results for microstructures containing an HMX packing fraction of 0.90. Results indicate a drastic increase in both threshold time and mean time to criticality when compared to the times for any other packing fraction. This drastic increase is hypothesized to be an artifact of the current computational framework, rather than a true measure of material response. Due to the use of an isotropic material description for the HMX grains, the only source of material heterogeneity is the distribution of binder throughout the PBX microstructure. However, when the amount of binder in the material becomes very small and the grains begin to contact one another through or around the binder, much of the geometric heterogeneity which leads to stress and strain localization begins to be washed away. In real PBX composites, the HMX grains are not isotropic, but rather they are anisotropic both in their elastic and plastic deformation behaviors due to the underlying crystal structure of the material. Chapter 5 studies the role of anisotropy on the impact response of a fully dense ensemble of HMX particles.

The second thrust of this chapter quantifies the ignition sensitivity of PBX by way of threshold velocity and critical input energy. The calculated threshold, or safe, velocity for this PBX is found to be almost exactly double the experimentally measured safe velocity as determined by the Steven sensitivity test in use at Lawrence Livermore National Laboratory. However, the factor of two difference may be explained by the difference in boundary conditions between the experiments and calculations. In the calculations, the stress wave is not allowed to influence the ignition sensitivity of the material after reflecting from the rigid anvil opposite the loading piston. In effect, this limits the ignition analysis to hotspots generated due to a single wave pass through the material. In contrast, the experimental setup of the Steven test only measures whether or not ignition is achieved, regardless of the number of wave passes. Therefore, as the stress wave is reflecting off of the rigid (or very stiff) rear confinement, the strain rate and axial stress can resemble the strain rate and stress state of a single, unreflected stress wave propagating from an impact up to twice as fast. The results have also been shown to have good agreement with the critical energy criterion of Walker and Wasley [15], but do not correspond to the H-J criterion in any way. Future work is currently under way to determine the significance of this deviation from the H-J type threshold criterion.

The final goal of this chapter has been to quantify the effect of viscoplastic HMX on both of the preceding sensitivity descriptions. Results have shown that viscoplasticity HMX increases the threshold time and mean time to criticality, and the range of critical times by as much as 25%, relative to identical specimens having elastic HMX. This delay of criticality echoes the decrease in sensitivity as determined by the threshold velocity and critical energy criterion. The results indicate that the threshold velocity for specimens having viscoplastic HMX is increased by 13 m/s (16.9%) relative the specimens with elastic HMX, and the critical input energy has been found to be 25% higher in the specimens having viscoplastic HMX.

CHAPTER 5: THERMOMECHANICAL RESPONSE OF POLYCRYSTALLINE HMX

Under dynamic loading, energetic crystals may ignite due to the localization of dissipated energy into small, intensely heated regions termed “hotspots”. These hotspots in energetic materials form through mechanisms such as compression of voids, friction between crack surfaces inside the material, and localized shear deformation [9, 23, 72-74]. Heating due to each of these mechanisms depends on the histories of the states of local stress and rate of deformation in the material. Existing literature examines the behavior of energetic crystals and polymer-bonded explosives (PBXs) in two general forms: as single crystals with anisotropic material properties [31, 33, 50, 75-88], and as heterogeneous collections of energetic grains with isotropic material properties [22, 24, 47, 89, 90]. The single crystal simulations have been carried out using both discrete methods (e.g., molecular dynamics (MD) and density functional theory (DFT)) [50, 75-84] and continuum scale methods [33, 85-88]. Analyses utilizing discrete methods have yielded understanding of many of the thermo-mechanical properties of the polymorphs of HMX including crystal structure and lattice parameters [79], isotherms [78], elastic constants [50], viscosity [75], thermal conductivity, and behavior in compression [76]. On the other hand, the continuum analyses have considered anisotropic yield surfaces with [33] or without [31, 85-88] circular (spherical) voids. The studies that consider PBXs as collections of heterogeneously distributed particles with isotropic properties are able to capture many of the complex interactions that arise from the mesostructure of the granular composites. 2D and 3D Eulerian simulations like those of Benson [22] and Baer [24] use isotropic material descriptions to analyze the stress and temperature fields generated by shock loading of porous granular HMX. Lagrangian simulations have been carried out to analyze the effect on ignition sensitivity of inter-particle friction (Soulard et al. [91] and Panchadhara and Gonthier [32]) and the effects of frictional dissipation along both interand intra-granular cracks on hotspot formation (Barua et al. [47]). Specifically, the study of Panchadhara and Gonthier concerns ensembles of initially porous granular HMX. The results showed the importance of both plasticity and friction along the surfaces of HMX grains in heating and hotspot formation. The studies of Barua et al. have concerned several issues, including the development of a framework to account for fracture, contact and frictional heating in microstructures of PBXs [47], contributions to heating of dissipation through fracture, friction in both HMX grains and the polymer binder (as well as along the grain-binder interfaces) [92] and the effects of the transient nature of loading on the contributions of the various heating mechanisms [64]. The study of Mas et al. [20] accounts for grain scale features in a coarse grained simulation by using the method of cells to model split Hopkinson pressure bar tests on PBXs. The results show that fracture plays a significant role at this scale on the deformation of the PBXs, due to large stress gradients between different phases. Even with this level of grain detail, it is still not possible to isolate specific localization sites due to the interaction of mesostructural organization, friction, and plasticity. Bardenhagen and Brackbill [93] investigated stress bridging and stress fingering in lattices of circular (cylindrical) grains. Using the particle and cell computational technique, they found the properties of the binder material to be the dominant factor affecting the stress distribution and localization in the grains. On the other hand, Bardenhagen et al. [94] embedded microstructures of a PBX obtained by X-ray microtomography in General Interpolation Material Point method simualtions of response under compressive loading. The method offers an explicit link between micromechanical information and macroscale models. The technique uses the stochastic transformation field analysis to capture multi-scale effects. The result is a statistical macroscale model capable of modeling the bulk material effects and strain distributions in the material. Taken together, these studies have clearly shown that material heterogeneities at different scales, elastic and inelastic deformation mechanisms, and dissipation through a range of bulk and interfacial avenues combine to affect the heating and development of hotspots in the materials. Despite the wide range of analyses reported, thus far no analysis has been carried out to account for the crystalline nature of HMX grains, the primary constituent in many PBX composites and granular explosives (GX). This lack of study for molecular crystals is in contrast to the extensive work that has been carried out for polycrystalline metals, including Cu [95-98], Ta [99, 100], titanium alloys [101, 102], and steels [103] among many others. These studies have shown that the polycrystalline nature of materials significantly affect local mechanical and thermal behaviors.

The primary objective of this paper is to analyze and quantify the effect of crystalline anisotropy and polycrystalline microstructure on the response of HMX-based PBXs and GXs. To this effect, the 3D Lagrangian framework developed by Rimoli et al. [104] for polycrystalline PETN is adopted. The specific form of HMX analyzed is β-HMX which has a monoclinic structure [90]. The analyses focus on the effects of polycrystalline slip and microstructure attributes on the early-time histories and heterogeneous variations of stress and temperature fields for imposed boundary velocities from 50 to 400 m/s. This paper does not deal with initiation. The model used does not account for the binder phase in PBXs, voids, cracks or other defects. In essence, what we analyze are polycrystalline aggregates of HMX grains with perfect bonding. This choice of framework allows us to fully quantify of the effects of (1) the structure of crystalline slip systems in HMX and (2) the microstructural level crystalline anisotropy on the conditions in energetic materials under prescribed loading and boundary conditions. In doing so, we provide a measure for the contribution to heating of crystalline plasticity as one of the many sources that hitherto has not been fully quantified for granular or polymer-bonded energetic materials.

This chapter is based on the published work in [27] performed in collaboration with Drs. Julian J. Rimoli and Min Zhou.

5.1 Energetic Molecular Crystals

The range of possible bonding strength between grains in PBXs and GXs can vary greatly, from no bonding (packed granular particles) to perfect bonding. Here, we only consider the case of perfect bonding, therefore, the systems can be regarded as polycrystalline ensembles in which the grain boundaries do not fail under conditions analyzed.

The polycrystalline model here can be regarded as an idealization of PBXs in which the thickness of the binder between adjacent grains is much smaller than the size of the grains so that it is taken to be zero. This approach simplifies the material condition and allows us to delineate the effect of intrinsic material anisotropy on the behavior of the overall material. The ensemble of crystals is generated using the relaxed dual complex (RDC) method proposed by Rimoli and Ortiz [105]. The RDC method takes as input an initial triangulation of the domain. The triangulation is then refined appropriately to provide suitably sized grains. Barycentric subdivision is performed on the entire refined triangulation and grains are defined as the barycentric dual of the nodes in the refined triangulation. The grain boundaries are then relaxed using a grain boundary energy minimization scheme to achieve the final grain morphologies. At this point, the grain ensemble is geometrically arranged into a regular packing of two distinct grain morphologies and sizes, as seen in Figure 2. The resulting microstructure is a polycrystalline HMX with each grain having a random crystallographic orientation. It should be pointed out that, although this method may not yield grain morphologies that perfectly match those observed in experiments, it provides an efficient way to generate microstructures with desired attributes such as grain sizes and grain size distributions. These microstructures can allow trends in material behavior to be explored. More realistic generation of 3D microstructures (see, e.g., [106, 107]) is not the focus of this study.

Regardless, the simulation framework adopted here lends itself to studies which could use microstructures generated using other methods.

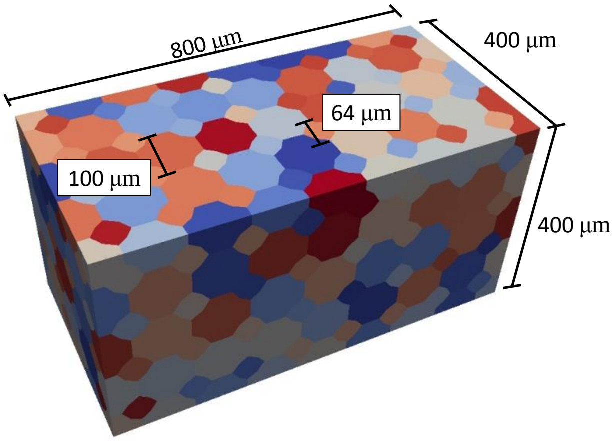

Figure 47. Configuration for 3D analysis and microstructure model.

HMX (octahydro-1,3,5,7-tetranitro-1,3,5,7-tetrazocine) is the primary energetic constituent in many PBXs, such as PBX 9501. This material is a polymorphic molecular crystal which has α, β, δ, and γ phases [89]. For determining the critical behaviors of HMX, the β and δ phases are of the greatest importance. The β phase has a monoclinic crystal structure and is stable at room temperature and pressure. It is commonly used in the initial formulations for PBXs [90, 108] and is the polymorph considered in this study. At 438 K, the β phase begins to transform to the δ phase, which has a hexagonal crystal structure, according to the Arrhenius kinetics [109, 110]. At 521 K, the melting temperature, the δ phase is more stable than the β phase at any pressure [111]. Under certain conditions, cracking can play a significant role in the response of β-HMX [7, 9, 33, 112] and extensive analyses have been carried out to quantify the dissipation associated with fracture and post-fracture crack-face friction. The consideration of fracture and friction requires a more complicated model and is beyond the scope of this paper. Such a model also has a disadvantage in that the cross influences between fracture and other dissipation mechanisms can make the delineation of the effects of specific mechanisms (crystalline slip in this paper) challenging. Here, we opt for a framework that focuses on the anisotropic crystalline response by accounting for both monoclinic elasticity and crystalline plasticity and by ignoring phenomena associated with fracture. Acknowledging that this is an idealization, we note that the benefit of this approach is the opportunity to systematically quantify the scale and extent of oscillations in the stress, deformation, and temperature fields in the materials resulting from the anisotropy of material response and microstructure heterogeneity.

5.1.2 Elasticity – Monoclinic Crystal Symmetry

The elastic properties of β-HMX have been thoroughly studied by way of nondestructive measurement techniques such as impulsive stimulated light scattering (ISLS) [113], Brillouin scattering [114], and MD simulations [50]. Table 5 contains sets of elastic constants obtained using each of these three methods.

Table 5. Elastic Properties of B-HMX.

	C_{11}	C_{12}	C_{13}	C_{15}	C_{22}	C_{23}	C_{25}	C_{33}	C_{35}	C_{44}	C_{46}	C_{55}	C_{66}
Zaug [113]	20.8	4.8	12.5	-0.5	26.9	5.8	-1.9	18.5	1.9	4.2	2.9	6.1	2.5
Stevens & Eckhardt [114]	18.4	6.37	10.5	-1.1	14.4	6.42	0.83	12.4	1.08	4.77	2.75	4.77	4.46
Sewell & Menikoff [50]	22.2	9.6	13.2	-0.1	23.9	13	4.7	23.4	1.6	9.2	2.5	11.1	10.1

Due to the monoclinic crystal symmetry in β-HMX, thirteen elastic constants fully define the elastic stiffness tensor. The elastic strain energy density can be written in the form of

$$\mathbf{W}^e = \boldsymbol{\varepsilon}^e : \mathbf{C}^e : \boldsymbol{\varepsilon}^e, \qquad (68)$$

where $\boldsymbol{\varepsilon}^e$ is the recoverable (elastic) portion of the strain tensor and C^e is the elastic stiffness tensor which can be expressed as

$$\mathbf{C}^e = \begin{bmatrix} C_{11} & C_{12} & C_{13} & 0 & C_{15} & 0 \\ C_{12} & C_{22} & C_{23} & 0 & C_{25} & 0 \\ C_{13} & C_{23} & C_{33} & 0 & C_{35} & 0 \\ 0 & 0 & 0 & C_{44} & 0 & C_{46} \\ C_{15} & C_{25} & C_{35} & 0 & C_{55} & 0 \\ 0 & 0 & 0 & C_{46} & 0 & C_{66} \end{bmatrix}. \qquad (69)$$

At high loading rates, pressure gradients cause gradients in the elastic moduli in the loaded and unloaded regions of the material. Therefore, a full representation of the anisotropic material behavior would include the evolution of each of the elastic moduli with respect to pressure. Such an analysis is beyond the scope of this investigation, but should be pursued when reliable, pressure dependent, anisotropic moduli are identified.

It should be noted that obtaining a complete set of temperature dependent constants would be advantageous due to the fact that the material undergoes significant heating during impact loading. Zaug [113] determined five of the necessary constants for two different temperatures using ISLS, but a lack of certainty on the remaining constants leads us to consider the other two data sets. An analysis of potential elastic constants has been done by Vial et al. [115], leading to the identification of the constants of Stevens and Eckhardt [114] as better than those of Zaug [113] because of the sample sizes used in the analyses. Zamiri [85] compares the responses obtained using these three sets of constants to the response experimentally measured by Rae et al. [7] in the [110] and [001] crystalline directions. It is found that the constants of Sewell et al. [50] provide the best fit to the experimental data. Based on this, we adopt the constants of Sewell *et al.* [50] in this study. The incorporation of fully pressure- and temperature-dependent elastic moduli is likely a future task when more complete data is available.

5.1.3 Crystalline Plasticity and Thermal Response

Relative to elasticity, considerably less information concerning the inelastic deformation of β-HMX exists in the literature. Analysis of impact experiments on specially grown single crystals has previously led to a belief that slip along the $(001)[100]$ and $(\bar{1}02)[201]$ systems (in P2$_1$/c notation) as well as twinning and cleavage [16] can occur in β-HMX. The slip along these two systems was subsequently considered in a continuum model to analyze the yield surface of HMX single crystals under quasi-static loading [85, 86]. More recently, MD simulations show that there are five additional potential slip systems: $(\bar{1}\bar{1}1)[\bar{1}0\bar{1}]$, $(011)[0\bar{1}1]$, $(\bar{1}02)[010]$, $(011)[100]$, and $(010)[100]$ [33]. Barton et al. have implemented a crystalline plasticity model with all seven slip systems to study the development of hotspots in the vicinity of an intragranular pore in a single crystal under shock loading with pressures of the order of 10 GPa. Figure 1 illustrates all seven slip systems relative to the unit cell in the P2$_1$/c space. The slip systems labeled in green also correspond to the two systems used by Zamiri. Due to the uncertainty concerning the slip behavior of β-HMX, we will consider cases with both two- and seven- slip systems and compare the differences in behavior for both cases. For clarity, we will refer to the case with two slip systems as the Zamiri case and the case with seven slip systems the Barton case. All seven slip systems and relevant material parameters are summarized in Table 6. Note that the two slip systems in the Zamiri case are among the seven slip systems in the Barton case.

The crystal plasticity model outlined below follows the formulation of Rimoli et al. [104]. The local deformation condition is described by the displacement gradient

$$\boldsymbol{\beta} = \nabla \mathbf{u}\,, \tag{70}$$

where **u** is the displacement field and ∇ is the gradient operator. The plastic portion of the displacement gradient is

$$\boldsymbol{\beta}^{p} = \sum_{\alpha=1}^{N} \gamma_{\alpha} \mathbf{s}_{\alpha} \otimes \mathbf{m}_{\alpha}\,. \tag{71}$$

In the above relation, N is the total number of slip systems, *α* is the number of a slip system, γ^{α} is the magnitude of the plastic shear strain on the α^{th} system, $\mathbf{s}_{\alpha}$ and $\mathbf{m}_{\alpha}$ are the unit vector in the slip direction and unit vector normal to a slip plane, respectively, corresponding to the α system. The irrecoverable (plastic) part of the linearized Green strain tensor can then be represented as

$$\boldsymbol{\varepsilon}^{p} = \frac{1}{2}\left[\boldsymbol{\beta}^{p} + \boldsymbol{\beta}^{pT}\right] \quad ,(72)$$

and the elastic part of the strain tensor is

$$\boldsymbol{\varepsilon}^{e} = \boldsymbol{\varepsilon} - \boldsymbol{\varepsilon}^{p}\,. \tag{73}$$

The work conjugate stress tensor for the linearized Green strain is the Cauchy stress, $\boldsymbol{\sigma}$. As a result of the linearization of the strain tensor, crystal orientations are constant and do not rotate under strains. The critical resolved shear stress (CRSS), τ_{c}^{α}, on each slip system can be described by the relation

$$\tau_{c}^{\alpha} = \tau_{0}^{\alpha} + \sum_{\beta=1}^{N} h_{\alpha\beta} \gamma^{\beta}\,, \tag{74}$$

where τ_0^α is the initial CRSS listed in **Table 6** and *h* is the hardening matrix for the crystal. Due to limited experimental characterization, the hardening matrix, *h*, is taken to be **0**, so hardening is not explicitly considered. The collection of functions given by

$$f^\alpha\left(\sigma,\tau_c{}^\alpha\right)=\tau^\alpha-\tau_c{}^\alpha \tag{8}$$

defines what is known as the yield surface in classical plasticity theory. The rate of plastic deformation is constrained by Equation 4 such that

$$\dot{\varepsilon}^p=\sum_{\alpha=1}^{N}\dot{\gamma}_\alpha\mathbf{s}_\alpha\otimes\mathbf{m}_\alpha \tag{9}$$

The admissible stresses are defined by the Kuhn-Tucker conditions,

$$\dot{\gamma}^\alpha\geq 0,\ \ f^\alpha\left(\sigma,\tau_c{}^\alpha\right)\leq 0,\ \ \dot{\gamma}^\alpha f^\alpha\left(\sigma,\tau_c{}^\alpha\right)=0 \tag{10}$$

which specify that the slip rate is non-negative and that plastic flow can only occur on the yield surface. The elastic predictor – plastic corrector method proposed by Cuitino and Ortiz [116] for solving the constitutive equations above is used. This method is similar to the projected Newton method when line search is avoided. The plastic work density is

$$W^p=\sum_{\alpha=1}^{N}\tau_0^\alpha\gamma^\alpha+\sum_{\alpha=1}^{N}\sum_{\beta=1}^{N}h_{\alpha\beta}\gamma^\alpha\gamma^\beta. \tag{11}$$

The heat equation accounting for both thermal generation and conduction is

$$\rho c_v\frac{\partial\theta}{\partial t}=k\nabla^2\theta+\eta\dot{W}^p, \tag{12}$$

where θ is temperature, ρ is mass density, c_v is specific heat, *k* is thermal conductivity, and η is the fraction of plastic work that is converted into heat. For the durations of the simulations carried out here (~1 μs), the characteristic distances of thermal conduction is smaller than the size of a single finite element [17], therefore the diffusive term in (12) does not have a significant role in the results reported here.

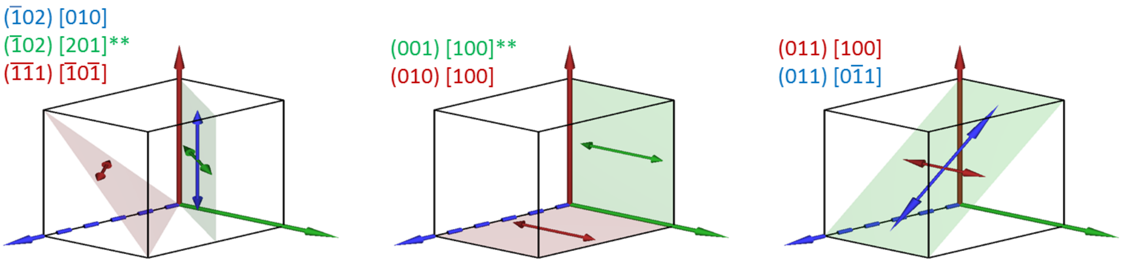

Figure 48. The seven potential slip systems of HMX crystal in the P21/c space. **The Zamiri case involves only the two slip systems labeled in green. The Barton case involves all seven potential slip systems shown here.

Table 6. Slip systems and critical resolved shear stresses for β-HMX [33]. All seven slip systems are active in the Barton case, but only the two systems labeled with an asterisk (#1 and 7) are used in the Zamiri case.

	$P2_1c$ Coordinates		Cartesian Coordinates		
α	mα	sα	mα	sα	τ_c^α
*Slip 1	$\{\bar{1}\ 0\ 2\}$	$\langle 2\ 0\ 1\rangle$	{0.660 0 -0.751}	<0.751 0 0.660>	38.73
Slip 2	$\{\bar{1}\ \bar{1}\ 1\}$	$\langle \bar{1}\ 0\ \bar{1}\rangle$	{0.845 0.500 -0.192}	<0.222 0 0.975>	72.2
Slip 3	$\{0\ 1\ 1\}$	$\langle 0\ \bar{1}\ 1\rangle$	{0 0.545 0.838}	<0.349 0.786 -0.511>	95.89
Slip 4	$\{\bar{1}\ 0\ 2\}$	$\langle 0\ 1\ 0\rangle$	{0.660 0 -0.751}	<0 1 0>	96.1
Slip 5	$\{0\ 1\ 1\}$	$\langle 1\ 0\ 0\rangle$	{0 0.545 0.838}	<1 0 0>	99.19
Slip 6	$\{0\ 1\ 0\}$	$\langle 1\ 0\ 0\rangle$	{0 1 0}	<1 0 0>	103
*Slip 7	$\{0\ 0\ 1\}$	$\langle 1\ 0\ 0\rangle$	{0 0 1}	<1 0 0>	173

5.1.4 Statistical Variation of Critical Resolved Shear Stress (CRSS)

In addition to the effect of the number and structure of slip systems, analyses are also carried out to study the effect of the variation of the critical resolved shear stress (CRSS) on the impact response of HMX. The average CRSS for each slip system, τ_0^α, is shown in Table 6. In the analyses, two scenarios are considered. The first involves the CRSSs being constant spatially and equal to the averages shown in Table 2. The second involves randomly varying the CRSS spatially throughout the microstructure in an element-by-element manner. The variation of each CRSS is relative to the average in Table 2 and follows a normal distribution, as illustrated in Figure 3. The standard deviation of the variations is 15% of the mean for each slip system to approximate the stochastic spatial variation of local strength measures. Comparing the uniform CRSS case and the case with random statistical variations of the CRSS allows the effect of stochastic variations of the material property to be delineated. The numerical implementation of the CRSS variations is achieved by assigning randomly varying CRSS values for each finite element in the microstructure.

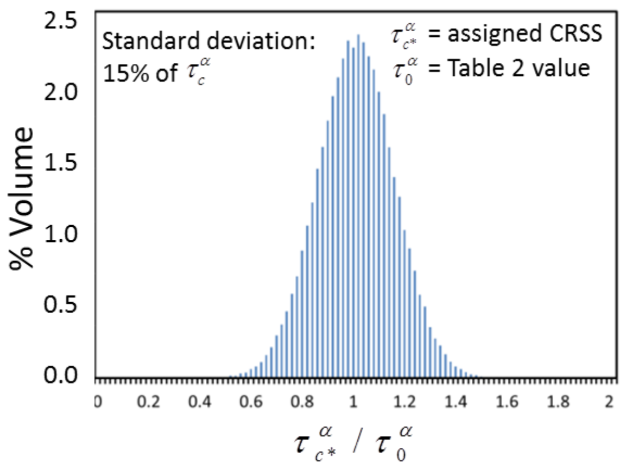

Figure 49. Statistical distribution of the spatial variations of the critical resolved shear stress (CRSS) considered. The variations follow a normal distribution about the reported mean values in Table 2.

5.2 Numerical Technique

Calculations carried out concern ensembles of β-HMX crystal grain subject to loading under planar impact. The calculations are performed using a Lagrangian finite element framework with 4-noded, linear strain tetrahedral elements. As shown in Figure 2, the specimen analyzed here has overall dimensions of 800×400×400 μm. The loading is effected by imposing an initially ramped (ramp time ~5 ns) velocity boundary condition in the longitudinal direction at the left face of the specimen. This loading condition involves the specification of the particle velocity history along the left face of the specimen. The profile imposed includes a steeply ramped region of about 5 ns followed by a constant velocity regime for the remainder of the calculation. The lateral faces of the specimen are prevented from moving transversely, therefore, the conditions in the specimen can be regarded as those of nominally uniaxial strain at the scale of the specimen size. The imposed boundary velocities range from 50 m/s to 400 m/s. Each specimen consists of 817 approximately equiaxed grains of either 100 μm or 64 μm in size (as labeled in Figure 2). In the single crystal baseline cases, all grains are crystallographically aligned in the same orientation. In the polycrystal cases, each grain has a randomly aligned crystalline orientation (creating a polycrystal with a random texture). Due to the small-strain assumption implicit in the constitutive equations, the grain orientations assigned initially do not change during the deformation. This assumption is reasonable since the magnitude of plastic strain observed is small.

5.3 Results and Discussions

In order to establish a baseline thermal response due to crystal plasticity, we have analyzed the response of single crystals of β-HMX to imposed boundary velocities in the range of 50 to 400 m/s. Each specimen is loaded in the $\{110\}$, $\{0\bar{1}1\}$, or $\{010\}$ crystal direction. For each orientation, the temperature rise is analyzed as a function of imposed velocity for both the Barton case and Zamiri case. The characteristic temperature rise for each case shown in Figure 4 is the average temperature rise behind the wave front in the three crystalline orientations. The solid line represents the average characteristic temperature of the three orientations. The error bars denote the highest and lowest characteristic temperatures among the three orientations. This figure shows that the characteristic temperature rise increases from 0.1 K at 50 m/s to 11.2 K at 400 m/s for the Barton case and from 0.14 to 4.0 K for the Zamiri case. Overall, the temperature increases are relatively low at several Kelvin, due to the homogenous nature of the samples. The low temperature increase in single crystal specimens echoes the idea that localizations or “hotspots” are necessary for high temperature rises in energetic materials. In the following sections, we will use these characteristic temperatures as baselines for comparison to evaluate the effects polycrystalline microstructure, numbers of slip systems, and spatial variations of the CRSS on the fluctuations in stress and temperature fields.

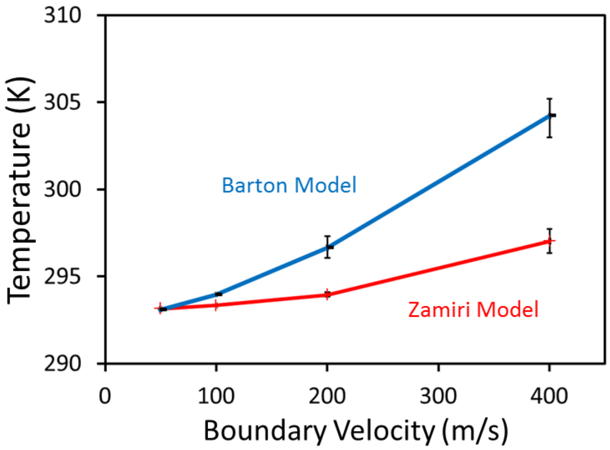

Figure 50. Characteristic temperature behind the stress wave front for single crystalline specimens of HMX with different orientations. The behaviors considered are described by the Barton model (blue) and the Zamiri model (red).

Each datapoint represents the average temperatrure in a single crystal specimen under impact along the {110}, {011}, and {010} directions.

5.3.1 Effect of Number of Slip Systems

The effect of the number of slip systems on the behavior of polycrystalline HMX is analyzed. Specifically, the two different material cases as described in Section 2.2, i.e., the Barton case with seven slip systems and the Zamiri case with two potential slip systems are used in the analysis. The calculations involve polycrystalline ensembles and imposed velocities from 50 to 400 m/s.

Figure 5 shows the evolutions of the longitudinal stress (a-c) and temperature (d-f) as the stress wave traverses a specimen of the Barton material. The imposed velocity is 200 m/s. The stress is non-uniform in the material, varying between 510 MPa and 1.65 GPa, due to the heterogeneous material microstructure. Although the stress level fluctuates spatially, the average longitudinal stress along the direction of wave propogation is approximately constant behind the stress wave front. In Figure 5(d-f), the temperature field is characterized by distinct regions of thermal fluctuations, reflecting the influences of both the non-uniform stress field and the anisotropic and heterogeneous material response. The localized nature of the stress and temperature fields is the focus of this study.

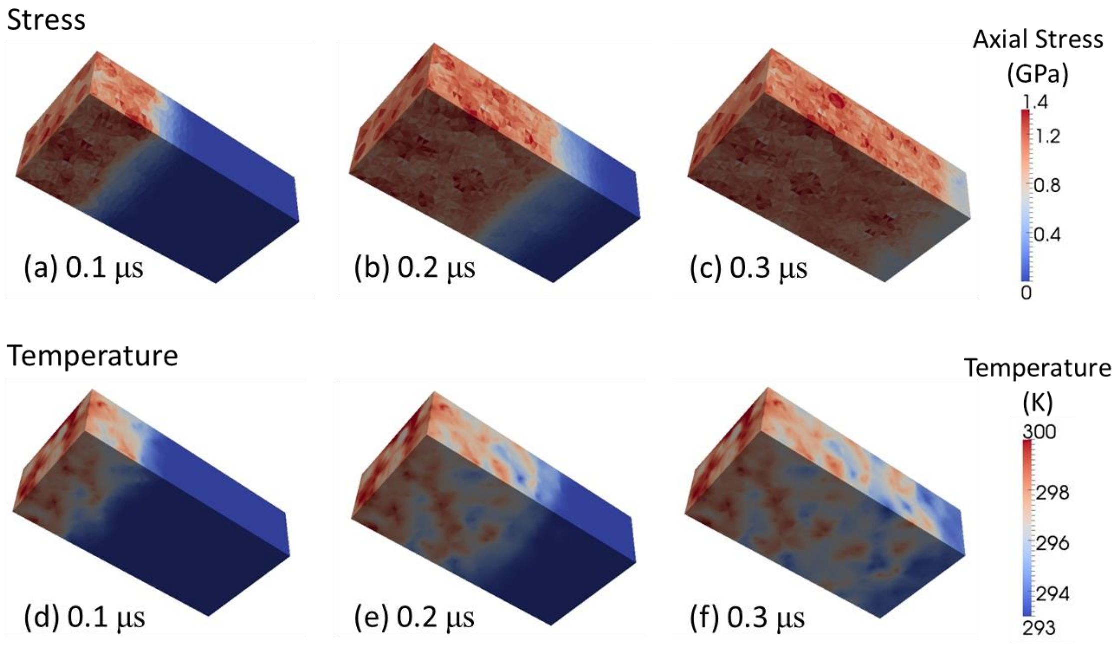

Figure 51. Distributions of longitudinal stress (a-c) and temperature (d-f) at different times in a specimen with seven slip systems. The domain has been cut along a longitudinal midplane in order to show the stress and temperature states on the interior of the specimen. The imposed boundary velocity is 200 m/s.

The mean, standard deviation, maximum, and minimum of the axial stress on planes parallel to the impact face are calculated at different distances from the impact face. Figure 6a shows the resulting values for the Barton case at an imposed velocity of 200 m/s. The black curve represents the mean stress. The blue and green curves are the mean stress ± one standard deviation and the mean stress ± two standard deviations, respectively.

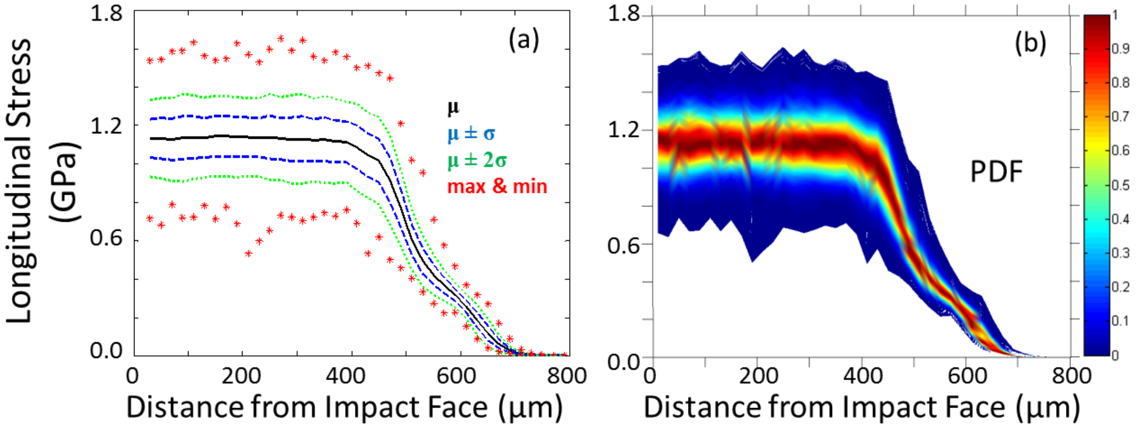

Figure 52. Distribution of stress in a sample with seven slip systems at an imposed boundary velocity of 200 m/s. (a) Lines represent the mean stress (black), mean stress plus/minus one standard deviation (blue), mean stress plus/minus two standard deviations (green), and the maximum and minimum stresses (red). (b) The color contours correspond to the probability density for the occurrence of a given stress level as a function of distance from the impact face. For every distance, a value of 1 (red) corresponds to the most probable value of stress.

The red asterisks denote the minimum and maximum stresses. Figure 6b shows the stress variation in the material in the form of a probability distribution function (PDF) as a function of distance from the impact face. At any given distance, a value of 1 (red) in the PDF represents the statistically most probable stress at that position in the specimen. The current analysis focuses on the behavior within the quasi-steady portion of the stress wave behind the wave front. In this plateau region, the mean and standard deviation of the axial stress have constant values of 1.1 GPa and 108 MPa, respectively, for this microstructure and the loading conditions. Figure 7 shows the mean longitudinal stress behind the stress wave front. This average stress is nearly linearly related to the imposed velocity for both material descriptions. The figure also shows that the mean stress is consistently higher in the Zamiri case than in the Barton case. This difference increases with imposed velocity

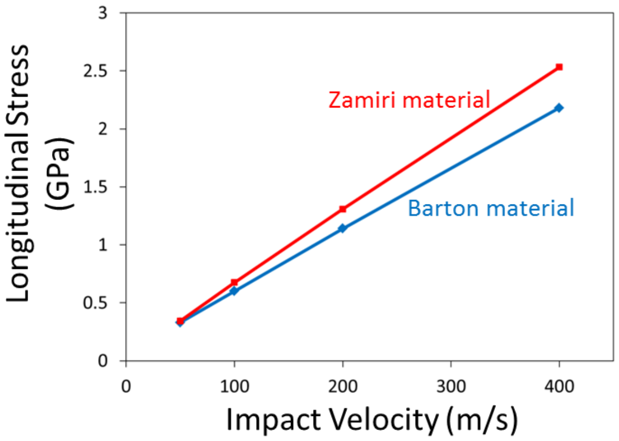

Figure 53. Plateau stress level behind the stress wave front as a function of impact velocity. The two slip system case (left) has a lower plateau stress level than the seven slip system case (right) at all impact velocities. Both increase with the impact velocity essentially linearly.

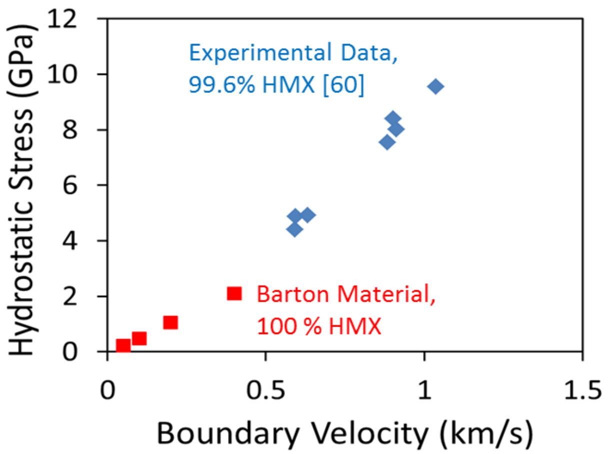

Figure 54. Comparison of calculated hydrostatic stress (red squares) for polycrystalline HMX (Barton case) and experimentally measured hydrostatic stress (blue diamonds) for solvent-pressed 99.6% dense HMX [60].

from 4.5% at 50 m/s to 16.2% at 400 m/s. Physically, this is due to the Zamiri case having limited avenues for energy dissipation via plastic slip, resulting in higher stresses due to higher fractions of elasticity in the material. The Barton case, however, has more avenues for accommodating plastic deformation through slip in more orientations, resulting in lower mean stresses. Figure 8 shows a comparison between the numerically calculated and experimentally measured [117] hydrostatic stress as a function of imposed piston velocity. The calculated value shown (red squares) is the average behind the stress wave front. The experimental data is for solvent-pressed 99.6% dense HMX [117]. The calculated stress levels are in good agreement with the experimental data.

In order to put the scatter of the stress states in perspective and quantify how the dispersion of the data changes with loading and material, the coefficient of variation (standard deviation normalized by the mean) and the normalized maximum stress (maximum stress normalized by the mean) are calculated. The coefficient of variation allows trends affecting a large percentage of the total volume of sample to be identified, and the normalized maximum provides insight into the extreme conditions in the domain. Figure 9 quantifies the dispersion of stress states in the materials by looking at the coefficient of variation of stress as a function of imposed velocity for both material cases. For all velocities, the Zamiri case displays greater variations in stress state than the Barton case. The coefficient of variation for the Zamiri case varies from a minimum of 0.118 at 50 m/s to a maximum of 0.145 at 400 m/s. The Barton case exhibited a maximum coefficient of variation of 0.113 at 100 m/s that decreases to a minimum of 0.064 at 400 m/s. This indicates a relationship between the heterogeneity in the material and the dispersion in the stress field: a higher level of heterogeneity corresponds to higher levels of expected variations in stress states. The lower bound of this phenomenon is simply the case of a homogeneous single-crystal under uniaxial loading. In such a limiting case, the stress state is uniform on cross-sections perpendicular to the loading axis. On the other hand, for polycrystals anisotropy and mismatch in orientations between the individual grains. In the Zamiri case, this effect is stronger. In the Barton case, however, the difference in response between different directions in each grain is less pronounced, leading to stress fluctuation levels that are lower than those in the Zamiri case. Another observation from Figure 9 is that the dispersion increases monotonically with imposed velocity in the Zamiri case but shows no simple trend in the Barton case. Specifically, the decrease in stress field variations at higher imposed velocities (above 100 m/s) in the Barton case is in agreement with the results by Trott et al. [12] for a mock PBX under shock loading. In contrast, the increasing levels of stress fluctuations in the Zamiri case suggest that this material representation may be missing essential dissipation mechanisms represented by the additional slip systems in the Barton case or fracture planes which are not modeled here.

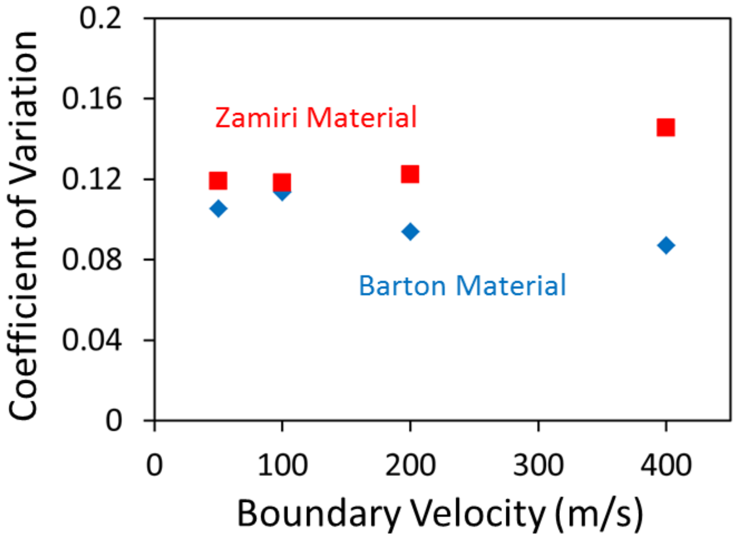

Figure 55. Dispersion of the longitudinal stress field in the quasi-steady region behind the stress wave front. As heterogeneity in the material increases due to material anisotropy, wider ranges of stress states are seen.

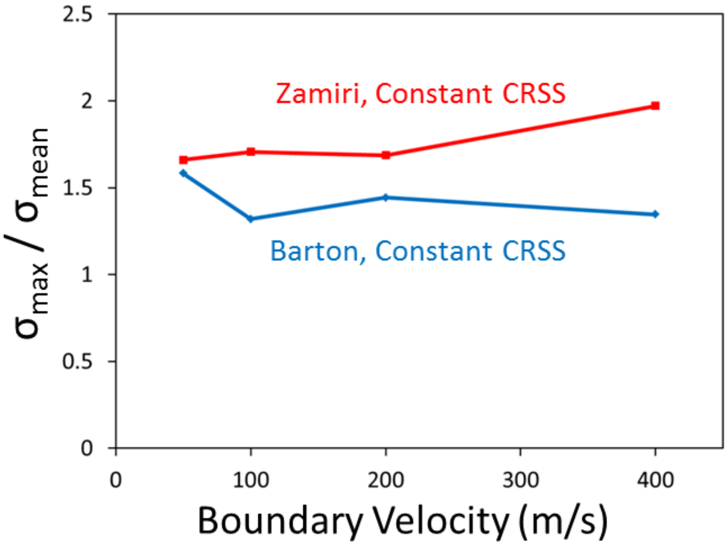

Figure 56. Maximum longitudinal stress normalized by averaged stress in the plateau region behind the stress front as a function of impact velocity for both Barton and Zamiri materials. This plot demonstrates the spread of the extreme values observed in the materials.

Figure 10 shows the normalized maximum stress for both cases as a function of imposed velocity. The maximum stress is between 1.6 and 1.9 times the bulk average stress for the Zamiri case and between 1.3 and 1.6 times the average stress for the Barton cases. The Zamiri case has greater variability in stress states for all impact velocities, as well as a wider range of stress states as indicated by the higher normalized maximum stress. The dispersion of the stress field indicates that greater anisotropy of the underlying crystal structure renders a material less capable of homogenized response. This quantitative analysis of the stress field reveals the influence of the number of slip systems on the variability of material states. Next, we analyze the effect of anisotropy on the variability of the temperature field.

Figure 11 shows the average (red) and peak (blue) temperature as functions of distance from the impact face for the Barton material case at an imposed velocity of 200 m/s. The average temperature is maximum at the impact face and decreases steadily away from the impact face. The peak temperature profile shows significant oscillations and does not follow a monotonic trend, suggesting a degree of stochasticity in the distribution of heating in the material. This observation echoes those of Refs. [32, 47, 64, 92, 118, 119]. An additional feature of Figure 11 is the plateau-like regions in the peak temperature profile. The “plateaus” are not exact flat regions of temperature. Rather, they have very similar temperatures. These regions correspond to grains (size of the regions on the order of grain size). Each grain has a specific grain orientation (dominant slip system) and the slips at different locations of a grain are similar, resulting in similar temperature levels. This is not to say temperature is uniform over any grain. It is only to say that it is possible that, for grains located and oriented in certain ways, temperature change may not be extremely non-uniform.

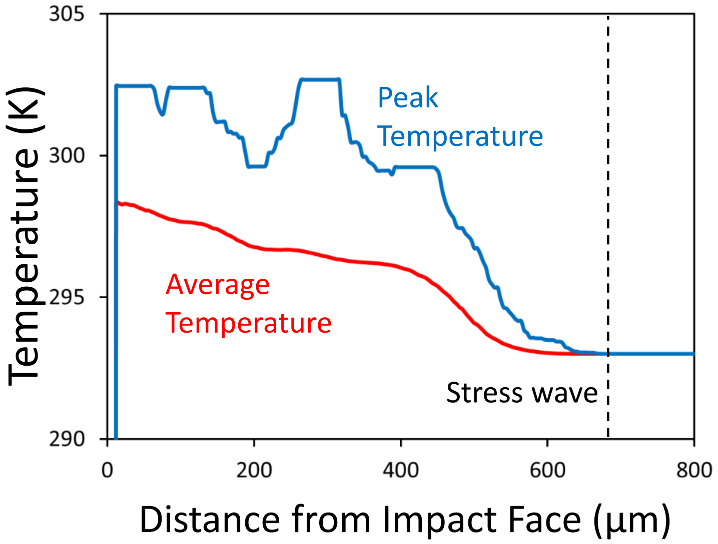

Figure 57. Peak and average temperature profiles for the Barton material at an imposed boundary velocity of 200 m/s. The average is over cross-sections normal to the loading direction.

Figure 12 summarizes the temperatures for both slip system cases with constant and variable CRSS. Figure 12a shows that the average temperature increases monotonically for both cases as imposed velocity increases and the rate of temperature increase is slightly higher at higher imposed velocities. The Barton case exhibits higher average temperatures at all imposed boundary speeds, ranging from 293.2 K at a speed of 50 m/s to 308.0 K at a speed of 400 m/s. The average temperature for the Zamiri material increases from 293.0 K at to a 50 m/s to 300.6 K at 400 m/s. The higher rate of average heating in the Barton case is due to the enhanced availability of slip systems relative to the Zamiri case. Figure 12b indicates that the peak temperatures are not strongly dependent on the number of slip systems. The peak temperatures increase from 293.4 K at 50 m/s to 325.4 K at 400 m/s for the Zamiri case and 293.6 K to 320.0 K for the Barton material. This similarity is due to both material descriptions sharing the $(001)[100]$ system, which has the highest CRSS. Therefore, the peak temperature rise in both material cases is associated with the strongest slip system which yields the highest temperature change for the same amount of slip.

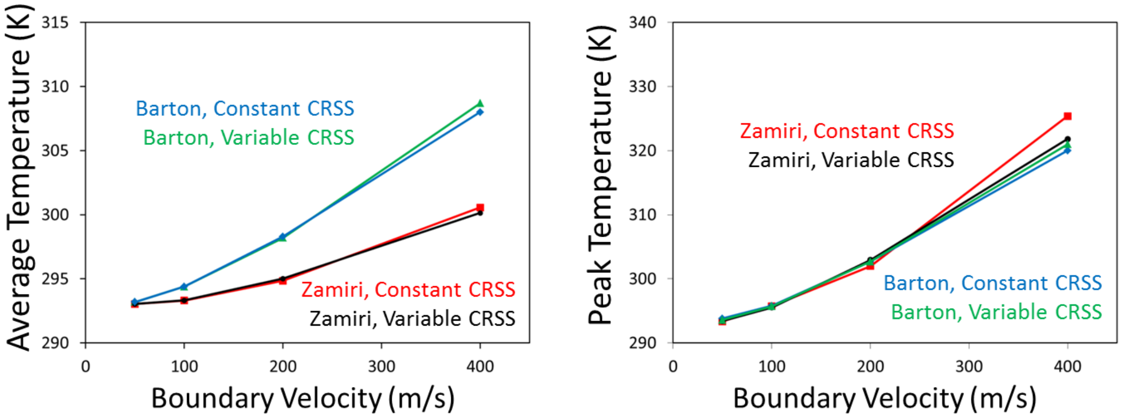

Figure 58. (a) Average temperature in the plateau region and (b) Peak specimen temperature as functions of impact velocity and CRSS.

In order to quantify the effect of the polycrystalline microstructure on the temperature rise in the specimens, we have compared the average and maximum temperature rises in the polycrystalline materials with the characteristic temperature rises for single crystals discussed earlier in Section 4. The average temperature rise in the polycrystalline specimens is 90.8% and 41.1% higher than that in the corresponding single crystal specimens for the Zamiri and Barton materials, respectively. The polycrystalline microstructure causes the maximum temperature rise to be 7.5 times higher relative to the single crystal in the Zamiri case and 1.65 times higher in the Barton case. From these results, it is clear that the resulting temperature field in the Zamiri material, which has only two available slip systems, is much more strongly affected by the polycrystalline environment than in the Barton material. For each material case, however, the effect of the polycrystalline microstructure on heating is fairly constant. Specifically, this is seen over the imposed velocity range of 100 to 400 m/s for Barton case and over 200 to 400 m/s for the Zamiri case. Data from this regime is used to characterize the effect of polycrystalline microstructure in this section and the effect of varying the CRSS in the next section.

As a measure of variability in the temperature field, the ratio between the peak temperature increase and the average temperature increase (normalized peak temperature rise) in the form of

$$\theta_n = average\left[\Delta\theta^{\max}(x) / \Delta\theta^{avg}(x)\right] \tag{13}$$

is used. Here, $\Delta\theta^{\max}(x)$ is the maximum temperature change and $\Delta\theta^{avg}(x)$ is the average temperature change at distance *x* from the impact surface. The normalized peak temperature change is shown in Figure 13. Over the range of imposed velocity from 50 to 200 m/s, the normalized peak temperature decreases from 8.01 to 4.04 for the Zamiri case and from 4.49 to 2.11 for the Barton case. So, although the Barton case exhibits overall more significant bulk heating under these loading conditions, the Zamiri case exhibits a consistently larger deviation from the uniformly heated case. This result reinforces the idea that when extreme material states are of interest and dominate material response, as is the situation in studies on the sensitivity of energetic materials, isotropic and homogeneous material properties lead to more uniform thermal and mechanical fields such as stress and temperature. The results presented here clearly indicate the effect of microstructure is more pronounced as the degree of anisotropy in the underlying crystal structure increases.

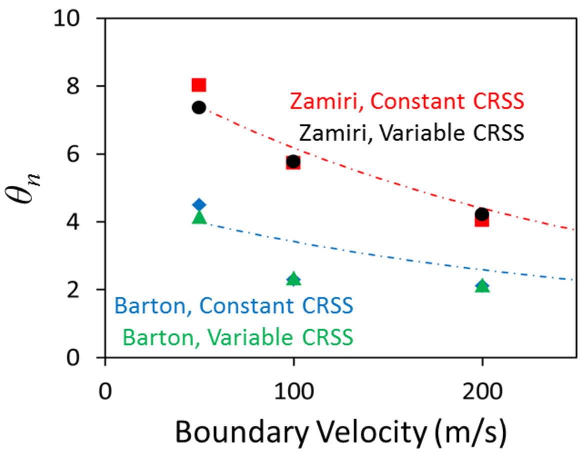

Figure 59. Peak temperature normalized by average temperature as a function of impact velocity. Four sets of simulations are presented: 1.) Zamiri material, constant CRSS (red squares), 2.) Zamiri material, variable CRSS with Gaussian distribution (black circles), 3.) Barton material, constant CRSS (blue diamonds), 4.) Barton material, variable CRSS with Gaussian distribution (green triangles). Dash lines represent prediction of Equation (13).

In order to quantify this effect, it is advantageous to develop a functional form for the normalized peak temperature rise, θ_n, that captures the evolution of θ_n as a function of the parameters studied: material anisotropy (*A*) and imposed velocity (*v*). A value of $\theta_n = 1$ corresponds to the case where the peak temperature rise is equal to the average temperature rise, indicating uniform heating along planes perpendicular to the loading direction. To choose an appropriate form for this relationship, two cases are considered: 1) in the limit of an isotropic material (defined as $A = 0$), $\theta_n = 1$; and 2) as the load intensity increases, microstructural details become less significant, i.e., as $v \to \infty$, $\theta_n \to 1$. These conditions motivate the use of a relationship in the form of

$$\theta_n(A, v) = 1 + cAe^{(-kv)}, \tag{14}$$

where *c* and *k* are constants, *v* is imposed velocity, and *A* is a scalar measure of the anisotropy of the plastic behavior of the underlying crystal structure. In order to use this relationship, a measure of material anisotropy as a function of available slip systems for both the Barton and Zamiri materials must be adopted. We have chosen to consider the anisotropy as a function of the number of available slip systems $\left(n_{ss}\right)$ and the coefficient of variation of the available CRSS $\left(c_v^{CRSS}\right)$. The value of c_v^{CRSS} is calculated by using the magnitudes of the available slip systems listed in Table 2. For the Zamiri case, the coefficient of variation of its two available slip systems is 0.63, and the coefficient of variation for the seven available systems in the Barton case is 0.39. The form of the relationship for *A* is determined by the limiting case of an isotropic material for which $A=0$. An isotropic material can be thought of as one that has an infinite number of slip systems which are uniformly distributed in all directions and have the same constant CRSS, consequently, we take $A=0$ if and only if $n_{ss}=\infty$ and $c_v^{CRSS}=0$. One form that meets the considerations is

$$A=\frac{1}{n_{ss}}+c_{\mathrm{v}}^{CRSS}. \tag{15}$$

For the analyses carried out, $A_{Barton}=0.53$ and $A_{Zamiri}=1.13$. For reference, the value for a bcc material having 48 slip systems with the same CRSS is 0.02. The normalized peak temperature rise in Figure 13 leads to *c* = 6.962 and *k* = 0.004. The dash lines in this figure show the predicted value of θ_n for both materials over the entire range of imposed velocity considered. This relationship for θ_n may be used to estimate the expected peak temperature in polycrystalline HMX.

5.3.2 Effect of Variation in CRSS

In this section, we will discuss the effect of spatially varying critical resolved shear stress (CRSS) on the material response. Figure 11 and Figure 13 compare the thermal behaviors of microstructures with constant CRSS and those microstructures with CRSS that changes from location to location in the material. The spatial variations of the CRSS follow the normal distribution, as shown in Figure 3. The two figures show that variation in CRSS has minimal effect on the average temperature, peak temperature, or the normalized peak temperature. Also, the average stress for the variable CRSS case differs from that for the constant CRSS case by less than 1.5% at all imposed velocities, with the coefficient of variation and normalized maximum stress both falling within 8.0% of the constant CRSS values as well.

To further quantify the contribution of the variation in CRSS, we have also compared the thermal response from the cases to the characteristic single crystalline cases in Figure 4. The average temperature rise is 94.4% higher than the characteristic temperature rise in the single crystals for the Zamiri material and 42.2% higher for the Barton material. These constitute a 3.8% and 2.8% change from the heating in polycrystalline microstructures with constant CRSS for the Zamiri and Barton cases, respectively. The peak temperature rise exhibits a similar trend, with the Barton material showing a peak temperature rise that is 2.65 times the rise in the single crystals and the Zamiri material showing a rise 8.4 times that in the single crystals. The contribution of variation in the CRSS to peak temperature is 1.9% for the Zamiri case and 0.3% for the Barton case.

The fact that variations in the CRSS has very little effect on the thermo-mechanical response is a strong indication that the material response in the loading regime considered is dominated by microstructural features other than the spatial variation of the CRSS.

Factors include the distribution of crystalline orientations, grain size and size distribution. Because the strongest slip system (highest CRSS) has a CRSS that is ~4.5 times that for the weakest system, varying any CRSS by as much as 50% has less influence on the mechanical response of a polycrystalline specimen than rotating grains to more/less favorable orientations for slip. In this paper, the results certainly show that the orientation of individual grains has a more significant effect on the response of the specimen than the variation of the CRSS. However, if the misorientation between the grains was limited, as in a textured specimen or a single crystal, the spatial variation of the CRSS may have a larger effect, this aspect is not analyzed here but may be considered in the future.

5.4 Conclusions

The behavior of a regularly structured polycrystalline HMX is investigated by considering perfectly bonded ensembles of single crystallites which have distinct individual crystalline orientations. The response characterization has focused on the evolution and variability of stress and temperature fields arising from impact loading. The quantification has primarily concerned the inhomogeneity in stress and temperature. It is found that crystalline anisotropy has a large effect on both the homogenized (averaged) material response and the dispersion in stress and temperature states in each specimen. The analysis is based on an implementation of the crystal plasticity models due to Barton et al. [33] and Zamiri and De [85], which contain seven and two potential slip systems, respectively. The results presented here indicate that the results based on the description of Barton et al. more closely matches previously published data [12]. Therefore, the Barton model is likely a more realistic representation of the inelastic behavior of HMX crystals in the absence of fracture or other dissipative mechanisms. The calculations carried out also show that spatial variations of the critical resolved shear stresses (CRSS) of up to 15% in a material have minimal effect on the bulk or local material response for the polycrystalline specimens analyzed.

The two key results of this chapter are (1) the determination of the magnitude of heating due to crystal plasticity and (2) the quantification of the effect of crystal anisotropy on the variability of stress and temperature states. With regard to the first point, a polycrystalline sample of HMX is shown to undergo average heating of 0.04 to 15.0 K and maximum local heating of 0.4 to 32.4 degrees K for imposed velocities up to 400 m/s. Even though the temperature rise due solely to crystal plasticity is significantly lower than that required to cause initiation, others have shown that plastic heating may be significantly exacerbated by the presence of other stress concentrators [33] or friction along crack surfaces [120] not explicitly modeled here.

Finally, the anisotropy inherent in polycrystalline microstructures has been shown to contribute significantly to the dispersion in the stress and temperature fields. This dispersion means that localized regions within microstructures experience significantly higher temperatures and stresses than those predicted by a homogenized model. These regions provide favorable locations for hotspots to form. In order to accurately account for the hotspot development, it is essential to model the fluctuations in the local stress state and temperature field due to, not only microstructural heterogeneities analyzed here, but also other processes such as friction, viscous dissipation, and pore collapse. Such studies are already being carried out [33, 70, 118, 120, 121].

CHAPTER 6: EVALUATION OF THEORETICAL ALUMINUM BONDED EXPLOSIVES

The introduction of aluminum particles to an explosive for the purpose of enhancing the blast performance was first achieved by Roth [49] in 1900. Subsequently, extensive testing of aluminized explosive formulations have been performed in order to understand the complex behavior of these materials and the effect that aluminum has on the performance. Aluminized explosives have been found to have enhanced late-time (behind the initial reaction of the primary explosive) behavior such as higher temperatures, incendiary effects, air blast, and bubble energy (when used under water) [122]. The mechanism leading to delayed effects from the aluminum is that time and energy are required to melt the oxide layer (Al_2O_3) that coats the aluminum particles as well as mass diffusion of oxidizer to unreacted aluminum. Therefore, the aluminum reacts with the products of the initial reaction, leading to an increased duration of sustained pressure [123]. Much work has also gone into determining the effect of aluminum content on the overall performance of the explosive. Experiments have shown that for aluminum content in excess of 20%, the detonation velocity of the explosive monotonically decreases with additional aluminum [124]. In spite of the decreased detonation velocity, Akhavan found that the total heat of explosion of a composition increases with aluminum content over a very wide range [18]. In addition, Gogulya et al. [125] focuses on the effect of aluminum particle size on the performance characteristics of explosive formulations. Gogulya found that the use of “ultra fine” aluminum particles (0.5 μm) lead to an increase in temperature duration and lower pressure output due to the small particles of aluminum effectively “coating” the HMX grains, thereby interrupting the development of a detonation wave front [125]. In terms of ignition sensitivity, experiments show that the aluminization of an explosive leads to desensitization in the framework of a drop-weight test [26].

This chapter outlines the potential for a new class of explosives that is based on aluminum and HMX. However, instead of using distributed aluminum particles of various sizes and morphologies, the proposed composition uses aluminum as the “binder” material. In effect, the composition of interest is a two-phase composite which is comprised of HMX particles suspended in an aluminum matrix, referred to hereafter as ABX. Because aluminum and its alloys display such a wide range of mechanical behaviors, in this chapter two ABX formulations are created, one utilizing commercially pure aluminum (AL1100) and the other an aircraft grade aluminum alloy (AL7075). While the current computational framework is not capable of evaluating the detonation performance of such a composite, the primary goal of this chapter is to quantify both the mechanical response of the ABXs to sustained impact loading and its ignition sensitivity as defined by Chapter 2.3. Once quantified, the total response of the ABX composite to impact loading is then compared to that of the PBX analyzed in detail in Chapters 3 and 4. Finally, the relative sensitivity is used as a measure of the feasibility of the ABX for potential use as an explosive formulation. It should be noted that the work of this chapter represents the first effort to computationally design a new class of energetic composite based on micromechanical CFEM simulations.

6.1 Characterization of Aluminum Alloys

6.1.1 1100 Aluminum

The first of the two aluminum types used as the binder or matrix material in an ABX formulation is commercially pure aluminum, known as AL 1100. The composition of AL 1100 is specified to contain no less than 99% aluminum. In order to adequately model the temperature and strain rate dependence of the flow stress for this material, the viscoplastic constitutive model presented in Chapter 2.2.2.3 is fit to experimental data. The quasi static stress strain behavior, including the yield stress and hardening, as well as the temperature dependence of the yield stress of this material is obtained from the data of Luthy et al. [57]. The strain rate dependence for this material is based off of the data obtained by Sil and Varma [30]. The parameter set used to describe the viscoplastic response of AL 1100 in this chapter is summarized in Table 7. The remaining material properties necessary to describe the elastic behavior of both AL 1100 and AL 7075 are included in Table 8. For the sake of distinguishing between the two ABX formulations, the ABX containing a matrix of AL 1100 is referred to for the remainder of the chapter as “weak ABX”.

Table 7. Parameters for modeling AL 1100 using a viscoplasticity model.

σ_0	ε_0	N	T_0	β
50 MPa	1.6×10^{-2}	0.3	292 K	2.7

$\bar{\varepsilon}_0$	m	$\bar{\varepsilon}_m$	a	κ
5.0×10^{-4}	70.0	8.0×10^{12}	30.0	0.32

Table 8. Elastic material properties for AL 1100 and AL 7075

Material Property	AL 1100	AL 7075
Young's Modulus	70.0 GPa	70.0 GPa
Density	2.80 g/cc	2.80 g/cc
Specific Heat	960 J/kg-K	962 J/kg-K
Poisson's Ratio	0.33	2.33

6.1.2 7075-T6 Aluminum

AL 7075-T6 is the designation for a high strength aluminum alloy. Its composition consists of 87.1 – 91.4% aluminum, 5.1 - 6.1% zinc, 2.1 – 2.9% magnesium, 1.2 – 2.0% copper, 0.18 – 0.28% chromium, less than 0.3% manganese, less than 0.4% silicon, less than 0.2% titanium, and less than 0.15% other. Because of its high strength and increased corrosion resistance, it is often used in applications such as aircraft fittings, gears, shafts, and other similar parts. Compared to the AL 1100, AL 7075 is stronger by a factor of 10 times, but exhibits a lower work hardening rate. The parameters related to the rate sensitive yield stress of the AL 7075 material are fit according to the experimental results in [60] and are summarized in Table 9. The ABX containing a matrix of AL 7075 is referred to for the remainder of the chapter as “strong ABX”.

Table 9. Parameters for modeling AL 7075 using a viscoplasticity model.

σ_0	ε_0	N	T_0	β
527 MPa	1.6×10^{-2}	0.1	292 K	2.7

$\bar{\varepsilon}_0$	m	$\bar{\varepsilon}_m$	a	κ
5×10^{-4}	125.0	8.0×10^{10}	24	0.32

6.2 Research Methodology

The calculations performed concern the mechanical response and ignition sensitivity of three distinct explosive formulations: a PBX composed of 81% HMX and 19% Estane, an ABX composed of 81% HMX and 19% AL1100, and an ABX containing 81% HMX and 19% AL7075. The calculations are performed using the 2D CFEM framework described in detail in Chapter 2 and explicitly tracks the evolution of viscoplastic deformation in the aluminum and HMX phases, viscoelastic deformation in the Estane phase, semi-arbitrary crack initiation and growth, friction between the faces of closed cracks, and thermal diffusion. The specimens used herein are 15 mm in length (direction of impact) and 3 mm in width. In order to separate the effect of small changes in the microstructural morphology from the effect of the aluminum matrix, each of the three formulations is approximated by an identical set of twenty microstructures having an HMX area fraction of 0.81 and generated using the methodology in Chapter 2.1. Effectively, the PBX and ABX microstructures are identical except that the Estane phase of the PBX specimens has been replaced by either AL1100 (weak ABX) or AL7075 (strong ABX). The mean and standard deviation of the HMX grain size distribution are 250.1 μm and 90 μm, respectively. To determine the ignition sensitivity over a range of impact scenarios, each microstructure is subjected to piston velocities ranging from 50 to 200 m/s for load durations of up to 8 μs. The boundary conditions for the CFEM analysis are shown in Figure 60. The lateral sides of the specimen are confined by a frictionless rigid wall and the far boundary of the specimen by a rigid anvil, creating a macroscopically uniaxial state of strain in the specimen.

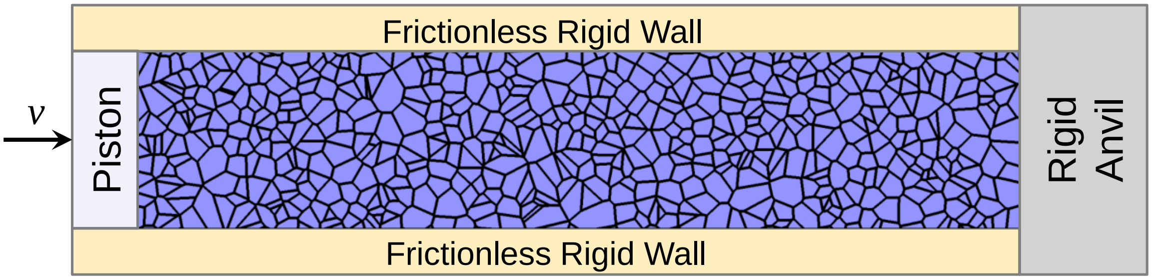

Figure 60. Loading and boundary conditions.

Following the execution of the CFEM analysis, the resulting temperature fields are analyzed for thermal runaway by applying the criticality condition derived from the work of Tarver et al. [38] described in Chapter 2.3. This analysis provides the critical load duration required for each ABX specimen to ignite. A statistical analysis of the distribution of the times to criticality based on the Weibull distribution function allows for the calculation of the mean time to criticality for the ABX. Finally, the critical energy required to ignite each

ABX will be utilized to compare the sensitivity of the two proposed ABX calculations to the PBXs analyzed in Chapters 3 and 4.

6.3 Thermo-Mechanical Response of ABXs

The first step in characterizing the total response of the ABX formulations hypothesized above is to fully describe its response to mechanical stimulus, in this case piston-driven, constant velocity impact. In this section, the mechanical, thermal, dissipative, and damage characteristics of the two ABX formulations will be quantified and explicitly compared to the corresponding PBX from Chapter 3. This provides a baseline understanding of the physical mechanisms that are occurring in the material and will set the framework for evaluating the difference in ignition sensitivity in the following section.

6.3.1 Stress Distribution

Quantification of the stress distribution includes a discussion of two measures of stress in the PBX specimens: the axial stress (often referred to as pressure in impact loading scenarios) and the von Mises equivalent stress which measures the shear stress in the material. Figure 61 shows the axial or longitudinal stress contours for the first 6 mm of specimen, as measured from the piston. From left to right are the PBX, weak ABX, and strong ABX. It is clear from the figure that very different mechanical processes are active in the two ABX specimens. The ABX specimens have a similar magnitude and distribution of axial stress states and have noticeably higher stresses throughout both the matrix and the HMX grains. Physically this is due to the difference in stiffness between the two binder systems. In the PBX, the Estane binder acts as a cushion, having very little stiffness or shear resistance (compared to the HMX grains). For the aluminum matrix, this is not the case. Instead of inserting a matrix of a soft material, the aluminum is approximately 3.3

times as stiff as the HMX grains and acts as a form of reinforcement for the composite microstructure.

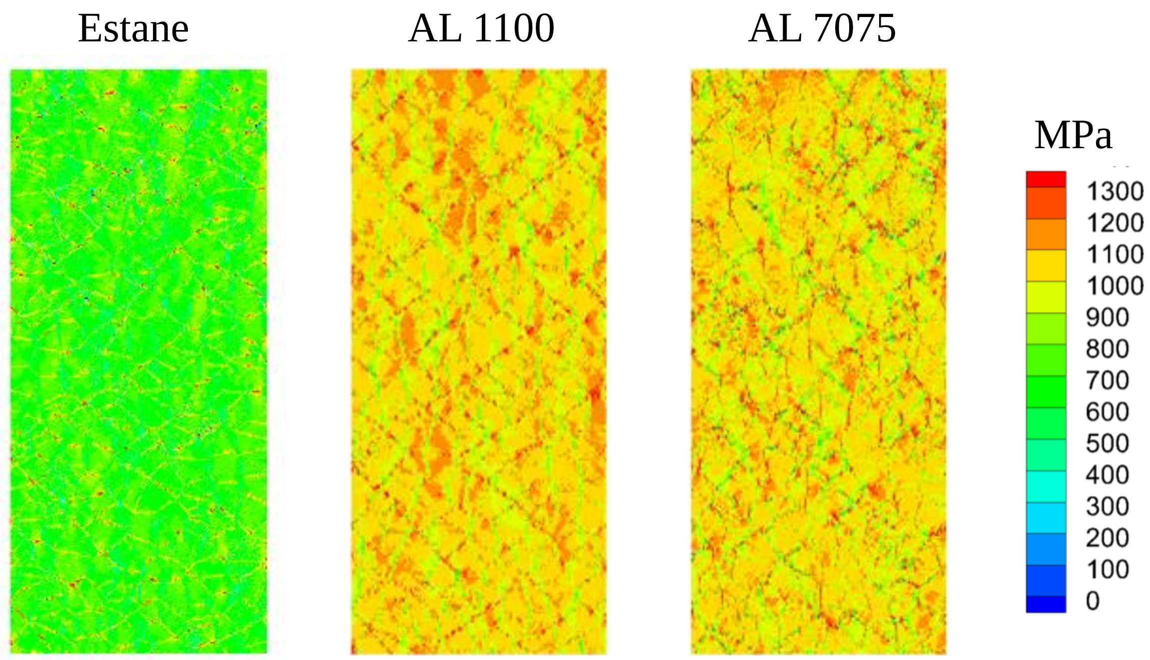

Figure 61. Longitudinal stress distribution for microstructures with Estane, AL 1100, and AL 7075 binders. Contours are taken from the 6 mm nearest the piston for a piston velocity of 200 m/s.

Figure 62 shows the axial stress as a function of distance from the piston for each of the three compositions. The first feature of note about the axial stress profiles is the marked difference in the slope of the wave front. For the PBX, the stress level rises smoothly from zero to its plateau stress with no apparent inflection points. In the ABX profiles, the stress wave front takes on added complexity due to the characteristics of the matrix material. For the weak ABX, shown in red, the stress profile shows two distinct regions of interest. The first one occurs near the foot of the profile, where the profiles of the weak and strong ABXs diverge from each other. This point corresponds to the onset of yielding in the weak pure aluminum, causing an apparent softening in the wave profile. The second feature of interest is where the weak and strong ABX profiles come back together. It is this stress level in the ABX loading history that the HMX grains begin to experience widespread, nearly homogeneous yielding throughout the material. Because the yielding in the HMX occurs at the same stress level in both scenarios. For the strong ABX specimen, only the change in inflection corresponding to ubiquitous yielding in the HMX is present because within this regime, the AL 7075 matrix is still operating primarily as an elastic material. Once the stress wave front has passed, the weak and strong ABX reach plateau stresses of 1369 MPa and 1337 MPa, respectively, corresponding to an increase in axial stress of 54% and 51% under the same imposed boundary velocity.

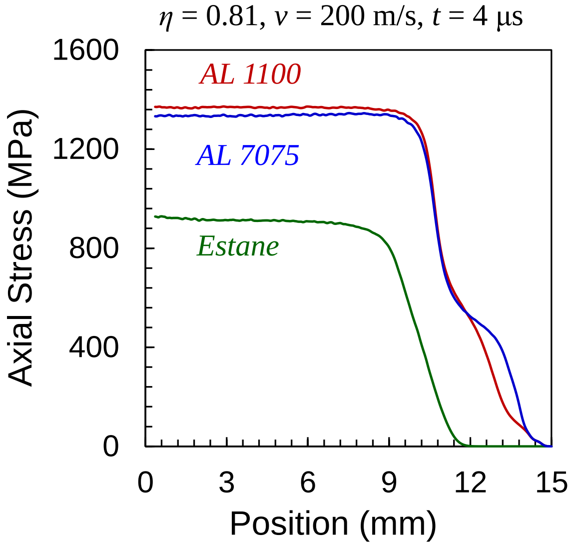

Figure 62. Axial stress as a function of distance from the piston for various binder systems.

Next, the von Mises stress distribution is considered. In mechanics, the von Mises stress is an effective measure of the shear stress in the material and is the portion of the total stress state that is directly affected by plasticity. Figure 63 shows the von Mises stress contours of the first 6 mm of specimen (as measured from the piston) for each of the three compositions under consideration. Interestingly, the von Mises stress level in the three materials is very similar in nature, however, that of the binder materials is distinct for each composition. In the PBX, the Estane binder carries von Mises stresses on the order of a few MPa only. The matrix of the weak ABX is loaded to the point that plastic deformation takes over as the dominant mechanism, leading to von Mises stresses of between 50 and 100 MPa. The matrix of the strong ABX material is very different from the other two in that it is capable of withstanding the shear stresses induced by impact loading without excessive dissipation due to either viscoelasticity or plastic dissipation. Figure 64 then serves to quantify the von Mises stress profile in the HMX phase of each of the three compositions. The figure shows that the von Mises stress profile for the HMX in the PBX formulation and in the weak ABX are very similar from the onset of loading up to the beginning of relaxation (obviously, the wave profiles are offset in time due to the difference in bulk composite wave speed), but the HMX in the PBX setting shows significantly more relaxation than both the weak ABX and strong ABX formulations. As discussed in Chapter 3, the difference in the amount of relaxation observed in the HMX phase of various compositions is due to differing amounts of fracture induced by the initial loading. The "relaxed" values of von Mises stress achieved in the weak and strong ABX specimens are 277 MPa and 238 MPa, respectively. These correspond to increases in relaxed von Mises stress over that in the PBX specimens of 29.5% for the weak ABX and 11.7% for the strong ABX.

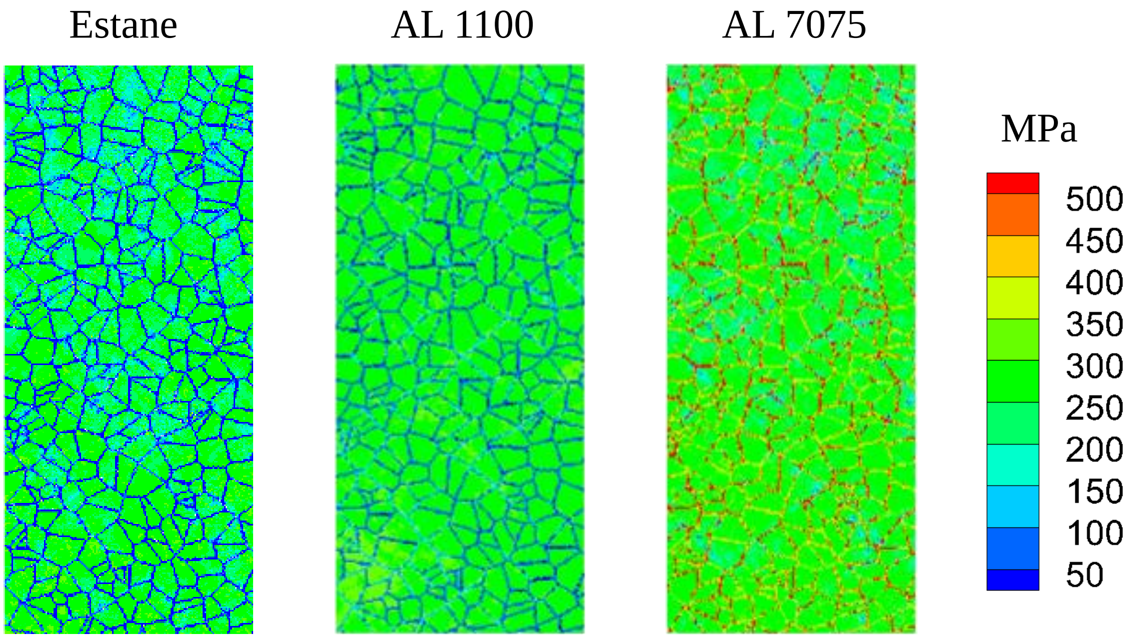

Figure 63. Von Mises stress distribution for microstructures with Estane, AL 1100, and AL 7075 binders. Contours are taken from the 6 mm nearest the piston for a piston velocity of 200 m/s.

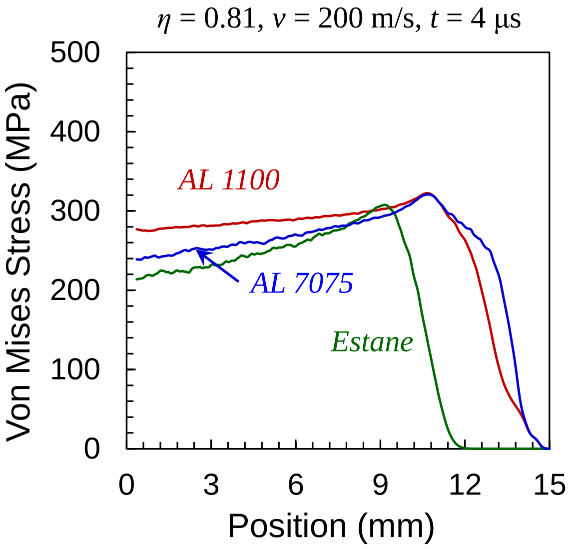

Figure 64. Von Mises stress as a function of distance from the piston for various binder systems.

6.3.2 Thermal Response to Impact

While the mechanical response of the ABX material systems is of interest in determining the mechanisms leading to ignition, the thermal response of the material actually determines if and when a specimen reaches criticality. Figure 65 shows the temperature contours for each of the three compositions. It is apparent that each of the three microstructure types have a pathway to temperature rise that is distinct from the others. In the PBX, the vast majority of the heating occurs on the extreme periphery of the grains. The heating in the PBXs concentrate on the grain boundaries because many of the grain boundaries have debonded from the surrounding binder and the grains themselves begin to crack near the edges of the grains. As a result, the region in the vicinity of the grain boundaries has both an abundance of fracture and potential friction sites, as well as more freedom for relative motion due to the proximity to the compliant binder. In the weak ABX, no widespread heating is present. In this material, all hotspots come in the form of isolated hotspots of relatively low intensity (compared to those seen in the PBX and strong ABX). In terms of location, the hotspots in the weak ABX typically occur at the junction of three or more HMX grains in a region in which the aluminum matrix is undergoing significant plastic deformation. In short, the weak ABX composition requires a combination of multiple contributing factors in order to generate a critical hotspot, a fact that likely contributes to the lower observed sensitivity in this material. The strong ABX heats in a way that is unseen in any of the other materials studied. The strong ABX heats almost exclusively along a large number of intragranular fractures that occur in this composition due to the high stiffness of the binder in the vicinity of the stress wave front. In Figure 65, these intragranular cracks are distinguished by the heated bands occurring at 45 degrees from the loading direction, regardless of the grain boundary locations. This is in sharp contrast to the heated locations in the PBX which can be clearly seen to follow the tortuous path of the complex grain boundary system. Figure 66 compares the peak temperature (average maximum temperature in the 20 specimens) as a function of distance from the piston. By comparing the peak temperature rise in each of the compositions, it provides an avenue for determining which types of localization characteristics are preferable for decreasing the sensitivity of a composite. The peak temperature rise in the soft ABX is 98 K, a 71% decrease relative to the PBX specimens, and in the strong ABX, the peak temperature rise is 172 K (49% decrease relative to the PBXs).

These results indicate that the most efficient mechanisms for generating hotspots in decreasing order are as follows. (1) Friction near a grain boundary in the presence of numerous fracture sites and adjacent to a compliant binder with low shear resistance. The high number of fracture sites provides adequate surfaces for the application of friction and the proximity to the compliant binder allows for increased relative motion. (2) Extensive network of intragranular cracking as seen in the strong ABX leads to significant heating. This mechanism is shown to lead to the generation of critical hotspots for loading intensities severe enough to fracture the grains during the time scale of the passage of the stress wave. For piston velocities incapable of generating large scale cracking in the HMX particles, the heating in the strong ABXs is not sufficient to lead to thermal runaway. (3) Friction on cracks near a grain boundary in the vicinity of a metallic binder. While the cracks near the periphery of the grains represent a potential for frictional sliding, the aluminum matrix greatly reduces the availability for relative motion between the opposing sides of the crack surface.

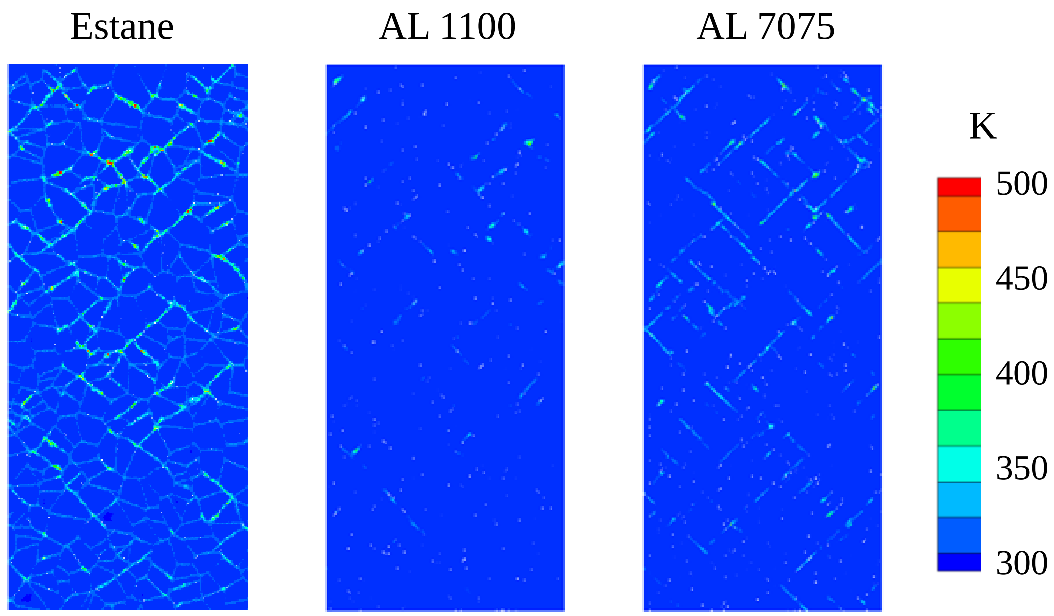

Figure 65. Temperature contours for composite systems with Estane, AL 1100, and AL 7075 as binders. Contours are taken from the 6 mm nearest the piston for a piston velocity of 200 m/s.

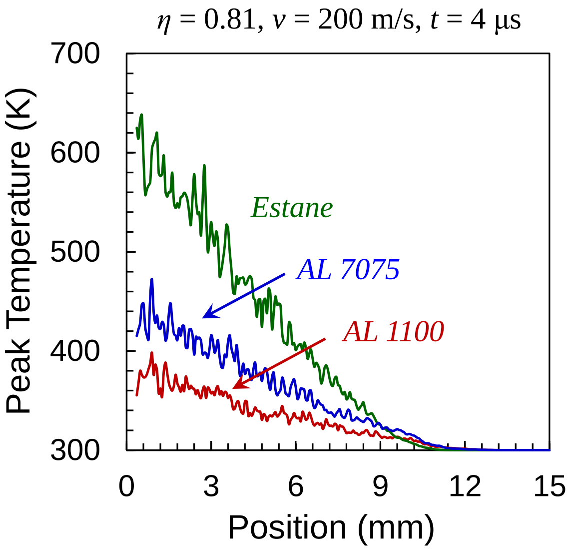

Figure 66. Peak temperature as a function of distance from the piston for various binder systems.

6.3.3 Energy Dissipation in HMX Phase of Composites

Much like the thermal response the energy partitioning in the ABX specimens is significantly different from that of the PBX. In the same manner that energy partitioning was discussed in Chapter 3, the distribution of frictional and plastic dissipation in the various compositions is described and the relative influence of the two primary dissipation modes is quantified and discussed. The frictional dissipation, shown in Figure 67, closely mirrors the spatial distribution of the temperature contour in Figure 65. The frictional dissipation in the PBX tends to conform to the grain boundaries and the strong ABX is dominated by frictional dissipation along intragranular cracks. The frictional dissipation distribution in the weak ABX contains characteristics of both. The physical explanation for the spatial dissipation pattern is the same as that discussed for the temperature field. The plastic dissipation contours for each of the three specimens is shown in Figure 69 and shows clear distinction between the 3 compositions. The plastic dissipation in the PBX is much lower in both magnitude and in terms of the area of material affected. This is due to the viscoelastic Estane material acting as a damper to relieve the stresses in the material that lead to plastic deformation. The two ABX compositions both show that plasticity is occurring in the HMX grains in all locations behind the stress wave front. The implication here is that the HMX grains are subjected to a much harsher load environment which overwhelms the yield strength of the material when the compliant, viscoelastic binder is replaced with an aluminum that is several orders of magnitude stiffer in addition to having significantly more shear carrying capacity. There is, however, an important distinction between the weak and strong ABX formulations is the plastic dissipation in the aluminum itself. In the soft ABX, plastic dissipation in the aluminum is the leading source of dissipation in the microstructure, introducing some additional compliance to the binder after the passage of the stress wave. This is not the case for the strong ABX, in which the aluminum exhibits no ubiquitous plasticity at any distance from the piston. This means that for piston velocities up to at least 200 m/s, the AL 7075 binder material in the strong ABX behaves essentially as an elastic material.

In addition to the differences in the distribution of the dissipative mechanisms in the various compositions, the magnitude of each dissipation type and the relative magnitude of the two dissipative mechanisms is dependent on the composition of the composite. In Figure 68, the frictional dissipation as a function of distance from the piston is shown for the PBX and both ABXs. From this figure, the frictional dissipation in the PBX grows much faster than in either of the ABX formulations. At 4 μs, the peak frictional dissipations in the soft and strong ABX are 0.7 and 3.0 J/mm^2, respectively, corresponding to a reduction in frictional dissipation of 91% and 61%, relative to that in the PBX. Because the frictional dissipation is growing faster than that in the ABXs, the difference between them will continue to increase with load duration, as long as the current trends hold true. In Figure 70, the plastic dissipation profiles are shown for the PBX and both ABX compositions. Interestingly, it appears that the plastic dissipation in both the PBX and the strong ABX are growing steadily with load duration, but the soft ABX very rapidly reaches a quasi-steady level of plastic dissipation that does not increase with load duration. At 4 μs, the weak and strong ABXs have peak plastic dissipations of 3.4 J/mm^2 and 4.64 J/mm^2, respectively. These levels correspond to a decrease in plastic dissipation of 7% for the soft ABX and an increase of 27% in the strong ABX, relative to the PBX. It should be noted, however, that the plastic dissipation in the three compositions grows at a different rate. This indicates that as the load duration increases, the amount of plastic dissipation in PBX will increase relative to the other two compositions, and that the plastic dissipation in the strong ABX will continue to increase relative to the soft ABX. Finally, the PBX and the ABXs show completely different trends in terms of the relative magnitude of frictional and plastic dissipation. In the PBX, the plastic dissipation is 53% smaller in magnitude at

4 μs than the frictional dissipation, a difference that will continue to increase with load duration because the frictional dissipation in the PBXs grows at a faster rate than the plastic dissipation. For both of the ABX compositions, however, the opposite trend is true. In the weak ABX, the plastic dissipation is 380% greater than the frictional dissipation. Because neither the plastic dissipation nor the frictional dissipation grow significantly with load duration, it is expected that this trend will continue to hold true for longer sustained loads. Like the weak ABX, the plastic dissipation in the strong ABX is 52% greater than the corresponding frictional dissipation. This reversal in trends is significant due to the difference in the way that friction and plasticity heat the material. Friction is by its very nature a surface based phenomenon effecting only relatively small volumes of material. Plasticity, on the other hand, is a bulk dissipative process that tends to act homogeneously of large volumes of material with only a few regions on localized effect. Therefore, it can be expected that the ABX formulations will exhibit a decrease in sensitivity in the current computational setting due to a favorable shift in the dominant dissipative mechanism from friction in the PBXs to plasticity in the ABX formulations.

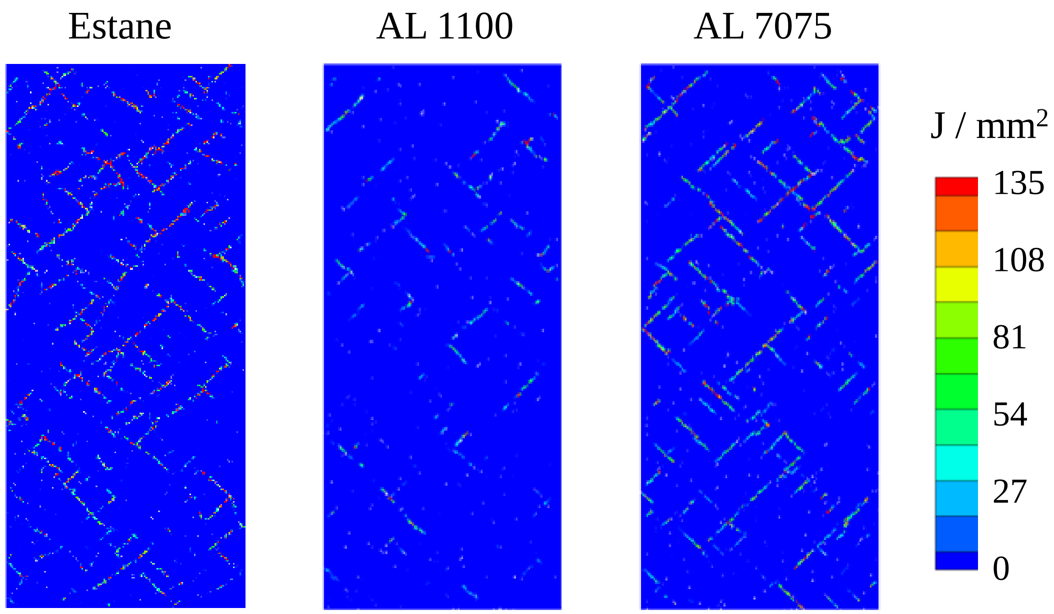

Figure 67. Frictional dissipation contours for composite systems with Estane, AL 1100, and AL 7075 as binders. Contours are taken from the 6 mm nearest the piston for a piston velocity of 200 m/s.

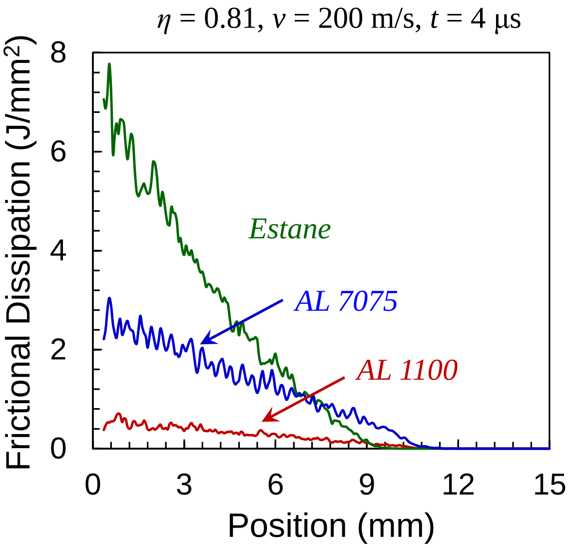

Figure 68. Frictional dissipation as a function of distance from the piston for various binder systems.

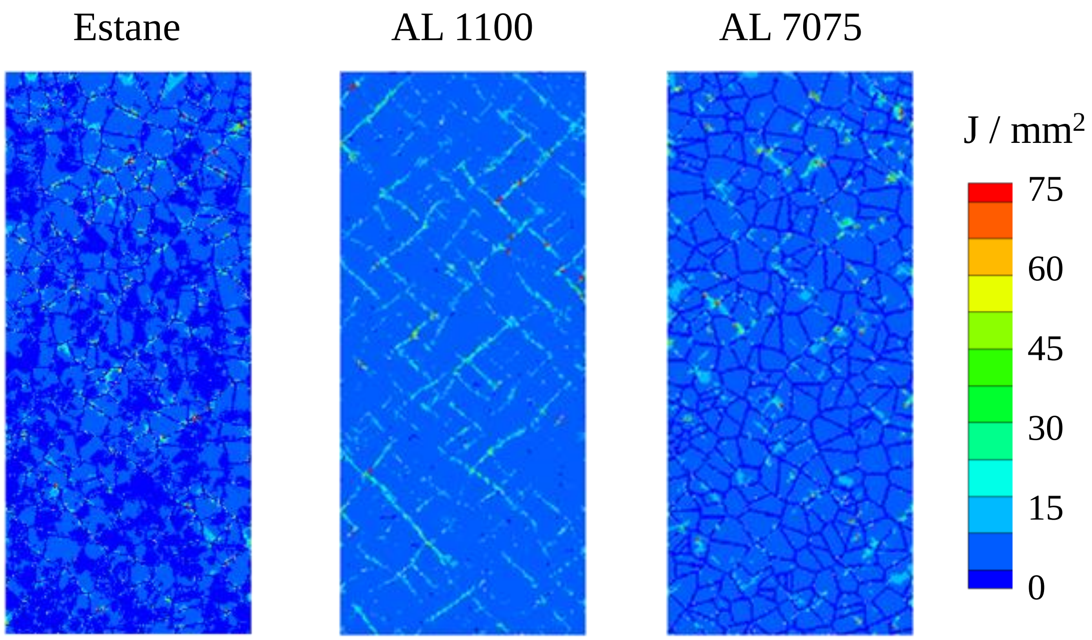

Figure 69. Plastic dissipation contours for composite systems with Estane, AL 1100, and AL 7075 as binders. Contours are taken from the 6 mm nearest the piston for a piston velocity of 200 m/s.

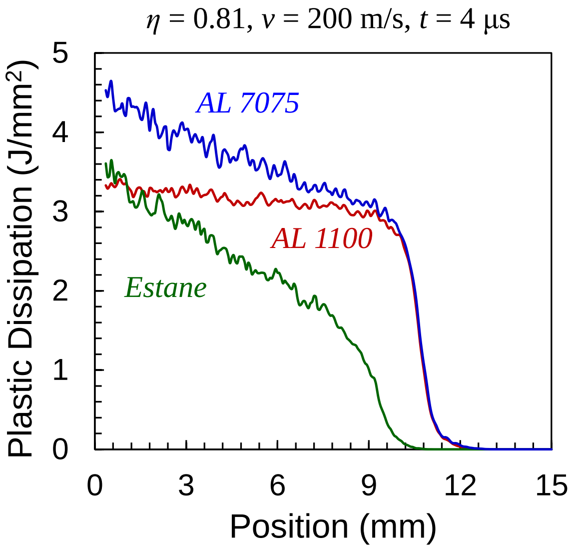

Figure 70. Plastic dissipation density as a function of distance from the piston for various binder systems.

6.3.4 Damage

In this section, the damaged induced in the HMX grains is quantified by comparing the average intragranular crack density for each of the three compositions. Figure 71 shows the HMX fracture density as a function of distance from the piston for the PBX, weak ABX, and strong ABX. Qualitatively, there is a significant difference among the three compositions. The damage density in the HMX phase of the PBX, as discussed in Chapter 3, ramps from undamaged to approximately 20 mm^{-2} in the vicinity of the stress wave front. However, for the PBXs, the damage continues to grow as a function of time. This contrasts with what is seen for the ABX specimens. The damage density profile for the weak and strong ABXs are similar in nature and are characterized by a sharp jump from undamaged to a relatively steady level of damage. Unlike the PBXs neither of the ABX compositions are characterized by damage densities that grow with load duration. The weak ABX plateaus at a fracture density of 16 mm^{-2} and the strong ABX reaches a steady fracture density of 68 mm^{-2}. For low load durations, the strong ABX exhibits the most intragranular damage of all of the compositions, but because of the continuous growth of damage in the PBX specimens, the PBX damage density grows to exceed that of both ABX formulations. The weak ABX containing commercially pure AL 1100 has the lowest amount of fracture, regardless of the load duration.

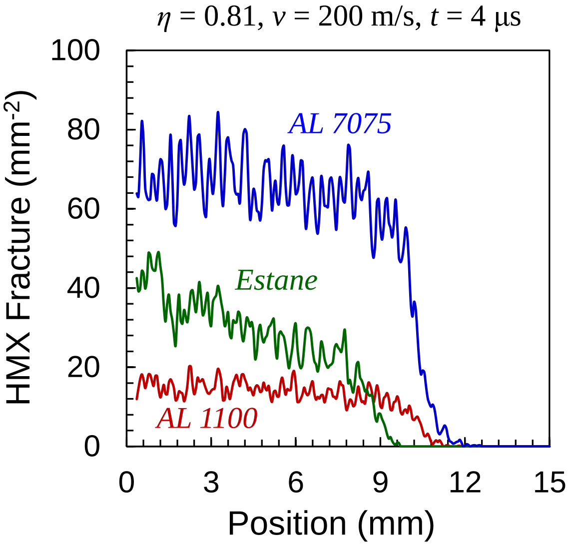

Figure 71. Damage density as a function of distance from the piston for various binder systems after 4 μs of wave propagation.

6.4 Ignition Sensitivity

With the addition of aluminum as the binding matrix holding together the ABX specimens, a significant amount of additional energy is available for reaction in the form of the aluminum itself. It is of vital interest whether that added added energy comes at the cost of increased sensitivity. To assess the sensitivity of the two proposed ABX formulations, each of the microstructures and loading conditions is subjected to the same criticality analysis technique as the PBX specimens in Chapter 4. The results show that the weak ABX specimens do not ignite for impact velocities lower than 200 m/s. At 200 m/s, the weak ABX ignites in only 30% of its specimens. For the strong ABX, there is no ignition for specimens loaded at 125 m/s or less. At 150 m/s, the strong ABX ignites 10% of the time and at 200 m/s, all specimens ignite. The critical times for the two ABX compositions are compared to those of a comparable PBX in Figure 72. It is apparent that there is a distinction in terms of both mean time to criticality and the range of critical times.

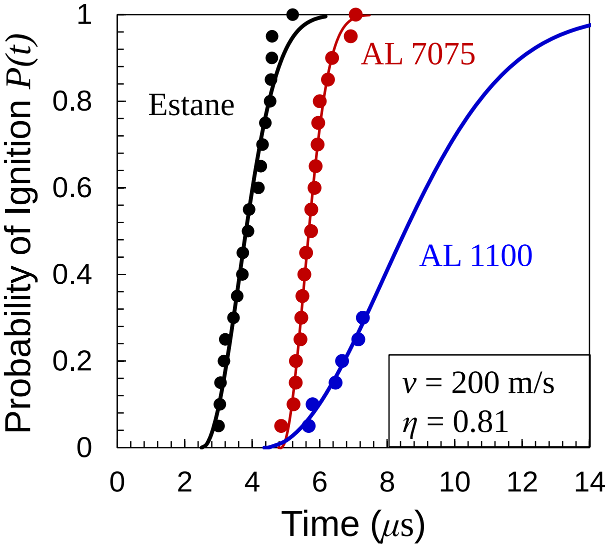

Figure 72. Weibull distribution functions for a PBX and two proposed ABX systems at 200 m/s.

In order to quantify the differences in the ignition sensitivity distributions for the three compositions, the specific values of threshold velocity (green), mean time to criticality (blue), and range of critical times (red) is presented in Figure 73. Interesting, the two ABX compositions exhibit a significant and similar increase in the threshold time required for ignition. The strong ABX shows an increase in threshold time of 2.34 μs (93%) and the weak ABX is characterized by an increase of 1.8 μs (74%). The nearness in magnitude of the threshold times for the two ABXs seems to indicate that the elastic stiffness of the binder may be a controlling factor in generating the early-time hotspot generation in these fully dense (no porosity) composites. If, as it seems, the increased stiffness of the binder controls the threshold time to criticality, it certainly does not control the range of critical times. In fact, as compared to the PBX, the strong and weak ABXs show opposing trends in terms of the range or spread of critical times. The strong ABX has a range of only 2.2 μs which is 35% lower than the range observed for the PBX specimen. This exceptionally small range of critical times (the lowest of any microstructure or loading scenario studied in this work) strongly indicates that for the strong ABX, there is a single dominant mechanism that is controlling the heating rate in all hotspots, leading to a high degree of uniformity in the observed times to criticality. The weak ABX, on the other hand, has a range of critical times of 10.75 μs, 219% larger than the corresponding PBX microstructures and the widest range of any composition tested. The marked difference between the response of the weak and strong ABXs after the ignition of the first critical hotspot indicates that there is some significant difference in the fundamental behavior leading to the development of hotspots in the two compositions. Upon inspection of the mechanical response of these two systems to the proscribed loading, the contour plot of plastic dissipation in Figure 69 stands out. It shows that the AL 7075 in the strong ABX calculations is, in fact behaving in a nearly elastic manner, exhibiting little plastic deformation, and therefore dissipating very little energy. This stands in stark contrast to the AL 1100 in the weak ABX calculations. The aluminum matrix in these calculations is seen to dissipate a large quantity of energy through the widespread plastic deformation of the AL 1100 matrix. This provides a clear indication that the amount of energy dissipated into the matrix material has a strong influence on the range of critical times.

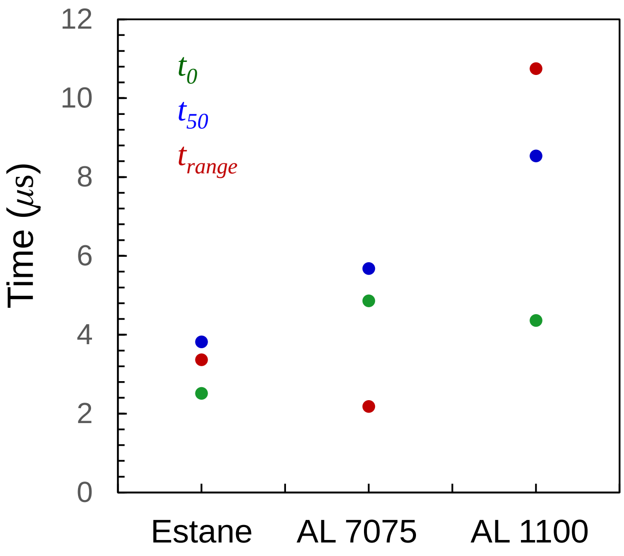

Figure 73. Variation of the Weibull parameters as a function of binder system.

In the ignition sensitivity analysis presented in Chapter 4, a modification of the $P^2\tau = \text{constant}$ relation originally introduced by Walker and Wasley [15] is presented and the relationship is fit to the elastic and plastic HMX based PBXs. Figure 74 re-presents the data from that analysis and superimposes the critical energy data points for the two proposed ABX compositions. It is clear that both of the ABX compositions are predicted by the preceding analysis to be significantly less sensitive than the associated PBX microstructures. As stated in Chapter 4, the critical energy corresponding the fit is 593 kJ/m^2. By comparison, the calculated critical energy of the strong ABX is 1519 kJ/m^2 and that of the weak ABX is 2336 kJ/m^2. These critical values indicate that the strong and weak ABX compositions require 156% and 294%, respectively, more energy than the corresponding PBX specimens to achieve ignition. This result provides strong evidence in support of the desensitization of an energetic composite by introducing a matrix system with very high toughness.

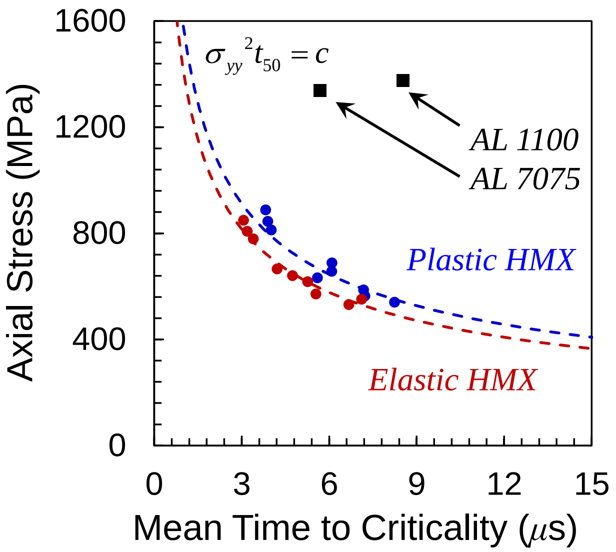

Figure 74. Comparison of the ABX sensitivity to that of the Estane based PBXs through the $\sigma_{yy}{}^2 t_{50} = c$ relationship.

6.5 Conclusions

The primary focus of this chapter has been to propose a hypothetical new class of explosive formulation that is comprised of HMX particles in an aluminum matrix and to evaluate the mechanical response and ignition sensitivity of the same.

The results show that the ABX formulations fundamentally change the mechanical response of the energetic composite to impact load, even with identical microstructural instantiations. The ABX formulations are shown to increase the level of axial stress by as much as 54%, relative to the PBX, and the von Mises stress is shown to be carried primarily by the aluminum matrix, as allowed by the yield strength of the aluminum. When the microstructures begin to heat, the significant differences among the PBX and the two ABX formulations become apparent. Each of the three formulations heats according to different controlling mechanisms. The PBX experiences heating along grain boundaries that have cracked and begin to experience a large magnitude of frictional sliding in the vicinity of the Estane binder which does not have the shear resistance to oppose the sliding. The majority of the heating in the strong ABX takes place in the form of frictional heating along the high density of intragranular cracks nucleated in the HMX grains. For the weak ABX, the only appreciable heating observed takes place in regions which combine the heating modes for PBX and the strong ABX.

The major takeaway from this chapter is the relative ignition sensitivity of the ABX formulations. Under the conditions studied (no voids, $\eta = 0.81$, and $v = 200$ m/s) the ABX formulations have been found to require 156% and 294% more input energy than an identical PBX to ignite the specimen. This result points to the feasibility of a hypothetical ABX formulation for the purpose of decreased sensitivity to low velocity impact. This recommendation is in light of the limitations of the current computational framework concerning the inability to explicitly model voids/pores or achieve shock loading, both of which could drastically change the predicted response of the proposed ABX formulations.

It should also be noted that the work of this chapter does not make any comment on the ability for this formulation to be produced, but only on whether such a composite has the potential to improve upon the mechanical behavior and ignition sensitivity of an equivalent PBX specimen.

CHAPTER 7: SUMMARY AND FUTURE DIRECTIONS

7.1 Summary

The effect of the viscoplasticity of the energetic component (HMX) on the mechanical, thermal, and ignition response of a two-phase (HMX and Estane) polymer bonded explosive (PBX) is analyzed. Specific attention is given to the high strain rate response of the composite during the first passage of a stress wave when impacted by a constant velocity piston. A methodology for computationally generating idealized microstructures with highly-controlled grain volume fraction and particle size distribution is utilized to create specimens with HMX grain fractions ranging from 0.72 to 0.90. The resulting microstructures are analyzed for impact loading from a constant velocity piston traveling at 50 to 200 m/s using a 2D cohesive finite element framework. The computational framework used employs an explicit and fully dynamic cohesive or fracture element framework to explicitly track the fracture and subsequent contact and frictional processes in the material. This framework accounts for finite deformation, thermo-mechanical coupling, semi-arbitrary crack initiation and growth, friction along crack faces, plastic heating, and thermal diffusion.

The initial focus of this work is to fully quantify the effect of the viscoplasticity of the HMX component on the behavior of the overall PBX composite. Results show that, relative to the case with the viscoplasticity turned off, the viscoplasticity of HMX causes a significant reduction in the magnitude of the von Mises equivalent stress and an increase in the hydrostatic stress in the HMX grains. PBX specimens with viscoplastic HMX show significantly less overall heating, lower peak temperatures, and lower numbers of hotspots or fractions of material experiencing localized heating relative to samples without viscoplasticity. This reduction in heating is found to be due to greatly reduced density of fracture sites. Specifically, the density of intragranular fracture is reduced by about 75%, the density of debonding sites between the HMX and binder is reduced by 35%, and the density of fracture sites within the binder is reduced by 23%. It is believed that the reduction in von Mises stress in the viscoplastic HMX acts to limit the driving forces for fracture and, once fracture occurs, contributes to lowering frictional sliding. Acting in concert with the lower fracture driving forces, the higher hydrostatic stress due to viscoplasticity further reduces the sliding friction by increasing the driving force required to initiate sliding.

The ignition sensitivity of the materials is evaluated to determine the effect, if any, of the viscoplasticity of HMX. An ignition threshold derived from chemical kinetics analysis is used to analyze the temperature distributions from the CFEM simulations and determine the load duration required to generate a hotspot of sufficient size and temperature to initiate a self-sustaining reaction or thermal runaway. The presence of one such a hotspot in a domain is said to “ignite” the specimen. A series of statistical approaches are implemented to quantify the distribution of required load durations necessary for ignition under the full range of loading conditions studied. For specimens in which ignition occurs, results show that the volume fraction of HMX has no significant effect on the load duration required to cause ignition. The viscoplasticity of HMX, however, is shown to increase the minimum loading duration required for ignition by as much as 25%, depending on the rate of loading. In addition, the mean load duration to cause ignition and the range of critical load durations are both increased by the viscoplasticity by as much as 25% and 22%, respectively. Analysis of the ignition sensitivity across the full range of load intensities yields a critical threshold velocity of 88 m/s required for ignition of a PBX due to a single pass of the stress wave. It is found that the Hugh James relation provides a poor fit for the results of the sensitivity analysis. Possible reasons for this discrepancy are discussed.

The analysis also shows a significant decrease in ignition sensitivity for microstructures containing 90% HMX by volume relative to microstructures with 72 – 81%

HMX. This reduction in sensitivity is thought to be the result of a reduction in material heterogeneity at high volume fractions of HMX grains. To test this hypothesis, a 3D crystal plasticity framework is employed to quantify the heterogeneities in stress and temperature fields due to inherent crystalline anisotropy of the HMX grains. It is found that in a densely packed polycrystalline HMX, the heterogeneities due to material anisotropy can contribute to increased stress gradients and localized temperature rise. The magnitude of heating due to crystal plasticity in a 100% dense HMX polycrystal as well as the distribution and variation in the stress and temperature fields are quantified and discussed.

Finally, the 2D CFEM framework is also used to study the response of composites with HMX grains in an aluminum binder called aluminum-bonded explosives or ABX. This investigation represents the first effort in the design of a new, novel material system guided by our computational micromechanics framework. The materials basically are formed by replacing the polymer in PBX with aluminum. This investigation focuses on assessing the advantages of such materials over PBX from a mechanical and ignition sensitivity standpoint. The results indicate that replacing the Estane matrix in PBX with an aluminum matrix can decrease the ignition sensitivity of the composite in terms of time required to ignition by as much as 295%.

7.2 Future Directions

Over the course of analyzing the mechanical response and ignition sensitivity of both PBXs and an as of yet non-existent aluminum – HMX composite material, several avenues for future research have become apparent. First and foremost, a concentrated effort to match numerical investigations to experimental configurations would allow for extensive validation of the entire computational framework through direct comparison with sensitivity experiments. The first step to accomplishing this goal is to modify and expand the range of specimen geometries, boundary confinement conditions, and loading conditions that can be reliably used within the CFEM framework. Additionally, an improvement to the numerical robustness of the computational framework will likely be necessary to investigate the types of loading events which are involved in sensitivity experiments. Take the Steven test for example. The fully confined specimen is attached to a rigid (or very stiff) anvil and a projectile is thrown into one side of the specimen. The stress wave induced by the projectile could traverse the material many times prior to ignition. It is also possible that ignition occurs as some small amount of material is crushed between the projectile and the anvil. Regardless of the computational complexity required, the validation of the model by way of experiments would be invaluable to the development of the computation capability.

The next avenue for future research can be described as minimizing the gap between numerical approximation and the material of interest. This body of research actually includes a number of enhancements. First, in order to produce finite element meshes which more faithfully capture the specified grain morphologies (either real or synthetic), the capability to implement unstructured meshing is needed. In addition, the development of an adaptive remeshing tool would allow the computational framework to actively remesh the domain in such a way that a unique, converged solution of crack nucleation and propagation becomes a possibility. Another computational advancement that would benefit the robustness and potentially the execution speed of the computational framework is the implementation of dynamically inserted (or initially rigid) cohesive finite elements. Such a method has been implemented in other numerical settings, and it completely eliminates the artificial softening that occurs due to the ubiquitous usage of finite stiffness cohesive finite elements.

Concerning the development of the proposed aluminum – HMX composite system, any further steps in the direction of developing or evaluating this material system would require collaboration with a laboratory facility having the capabilities to produce some version of this concept. Numerous technical hurdles exist that would make this task difficult including how the HMX particles would become distributed in the aluminum matrix. Because the melt temperature of aluminum is significantly hotter than the temperature required to cause reaction in the HMX grains, some cold method of mixing, combining, or pressing would be required to successfully generate samples of the ABX material.

REFERENCES

1. Switzer, L.L., et al. *Threshold studies of heated HMX-based energetic material targets using the Steven impact test*. in *AIP CONFERENCE PROCEEDINGS*. 2004. IOP INSTITUTE OF PHYSICS PUBLISHING LTD.

2. James, H. and D. Hewitt, *Critical energy criterion for the initiation of explosives by spherical projectiles.* Propellants, explosives, pyrotechnics, 1989. **14**(6): p. 223-233.

3. Chidester, S.K., C.M. Tarver, and R. Garza. *Low amplitude impact testing and analysis of pristine and aged solid high explosives*. in *Eleventh (International) Symposium on Detonation, ONR*. 1998.

4. Barua, A., *Mesoscale computational prediction and quantification of thermomechanical ignition behavior of polymer-bonded explosives (PBXs).* 2013.

5. Berghout, H., et al., *Combustion of damaged PBX 9501 explosive.* Thermochimica Acta, 2002. **384**(1): p. 261-277.

6. Dick, J.J., A.R. Martinez, and R.S. Hixson, *Plane impact response of PBX 9501 and its components below 2 GPa*, 1998, Los Alamos National Lab., NM (United States).

7. Rae, P., D. Hooks, and C. Liu. *The stress versus strain response of single β-hmx crystals in quasi-static compression*. in *Proceedings of the Thirteenth International Detonation Symposium, Office of Naval Research*. 2006.

8. Rao, P.T. and K.A. Gonthier, *Mesostructure Dependent Reactive Burn Modeling of Porous Solid Explosives.*

9. Palmer, S. and J. Field, *The Deformation and Fracture of $\ beta $-HMX.* Proceedings of the Royal Society of London. A. Mathematical and Physical Sciences, 1982. **383**(1785): p. 399-407.

10. Cady, C.M., et al., *Mechanical properties of plastic-bonded explosive binder materials as a function of strain-rate and temperature.* Polymer Engineering & Science, 2006. **46**(6): p. 812-819.

11. James, H., *An extension to the critical energy criterion used to predict shock initiation thresholds.* Propellants, explosives, pyrotechnics, 1996. **21**(1): p. 8-13.

12. Trott, W.M., et al., *Investigation of the mesoscopic scale response of low-density pressings of granular sugar under impact.* Journal of Applied Physics, 2007. **101**(2): p. 024917-024917-21.

13. De Longueville, Y., C. Fauquignon, and H. Moulard. *Initiation of several condensed explosives by a given duration shock wave*. in *Proceedings Sixth Symposium (International) on Detonation*. 1976.

14. Green, L., A. Weston, and J. Van Velkinburg, *MECHANICAL AND FRICTIONAL BEHAVIOR OF SKID TEST HEMISPHERICAL BILLETS*, 1971, California Univ., Livermore. Lawrence Livermore Lab.

15. Walker, F. and R. Wasley, *Critical energy for shock initiation of heterogeneous explosives*. 1968: University of California, Lawrence Livermore Laboratory.

16. Dick, J., et al., *Elastic–plastic wave profiles in cyclotetramethylene tetranitramine crystals.* Journal of Applied Physics, 2004. **96**(1): p. 374-379.

17. Menikoff, R. and T.D. Sewell, *Constituent properties of HMX needed for mesoscale simulations.* Combustion theory and modelling, 2002. **6**(1): p. 103-125.

18. Akhavan, J., *The chemistry of explosives*. 2011: Royal Society of Chemistry.

19. Corley, J., et al. *A combined experimental/computational approach for assessing the high strain rate response of high explosive simulants and other viscoelastic particulate composite materials*. in *AIP Conference Proceedings*. 2002. IOP INSTITUTE OF PHYSICS PUBLISHING LTD.

20. Mas, E., et al. *Applying micro-mechanics to finite element simulations of Split Hopkinson pressure bar experiments on high explosives*. in *AIP Conference Proceedings*. 2002. IOP INSTITUTE OF PHYSICS PUBLISHING LTD.

21. Baer, M.R., *Mesoscale modeling of shocks in heterogeneous reactive materials*, in *ShockWave Science and Technology Reference Library*. 2007, Springer. p. 321-356.

22. Benson, D.J. and P. Conley, *Eulerian finite-element simulations of experimentally acquired HMX microstructures.* Modelling and Simulation in Materials Science and Engineering, 1999. **7**(3): p. 333.

23. Menikoff, R. *Pore collapse and hot spots in HMX*. in *AIP Conference Proceedings*. 2004.

24. Baer, M., *Modeling heterogeneous energetic materials at the mesoscale.* Thermochimica acta, 2002. **384**(1): p. 351-367.

25. Baer, M., D. Gartling, and P. DesJardin, *Probabilistic models for reactive behaviour in heterogeneous condensed phase media.* Combustion theory and modelling, 2012. **16**(1): p. 75-106.

26. Prakash, V., et al., *Influence of aluminium on performance of HTPB-based aluminised PBXs.* Defence Science Journal, 2004. **54**(4): p. 475-482.

27. Hardin, D., J. Rimoli, and M. Zhou, *Analysis of thermomechanical response of polycrystalline HMX under impact loading through mesoscale simulations.* AIP Advances, 2014. **4**(9): p. 097136.

28. Miller, A.K. and O.D. Sherby, *A simplified phenomenological model for non-elastic deformation: Predictions of pure Aluminum behavior and incorporation of solute strengthening effects.* Acta Metallurgica, 1978. **26**(2): p. 289-304.

29. Espinosa, H.D., P.D. Zavattieri, and S.K. Dwivedi, *A finite deformation continuum\ discrete model for the description of fragmentation and damage in brittle materials.* Journal of the Mechanics and Physics of Solids, 1998. **46**(10): p. 1909-1942.

30. Sil, D. and S. Varma, *The combined effect of grain size and strain rate on the dislocation substructures and mechanical properties in pure aluminum.* Metallurgical Transactions A, 1993. **24**(5): p. 1153-1161.

31. Yan-Qing, W. and H. Feng-Lei, *A micromechanical model for predicting combined damage of particles and interface debonding in PBX explosives.* Mechanics of Materials, 2009. **41**(1): p. 27-47.

32. Panchadhara, R. and K. Gonthier, *Mesoscale analysis of volumetric and surface dissipation in granular explosive induced by uniaxial deformation waves.* Shock Waves, 2011. **21**(1): p. 43-61.

33. Barton, N.R., N.W. Winter, and J.E. Reaugh, *Defect evolution and pore collapse in crystalline energetic materials.* Modelling and Simulation in Materials Science and Engineering, 2009. **17**: p. 035003.

34. Henson, B.F., et al. *Ignition chemistry in HMX from thermal explosion to detonation*. in *AIP Conference Proceedings*. 2002.

35. Semenov, N.N., Z. Physik, 1928. **20**.

36. Frank-Kamenetskii, D., *Mechanisms of two-stage ignition.* Zh. Fiz. Khim, 1940. **14**: p. 30-35.

37. Thomas, P.H., *On the Thermal Conduction Equation for Self-Heating Materials with Surface Cooling.* Trans. Faraday Soc., 1958. **54**: p. 60-65.

38. Tarver, C.M., S.K. Chidester, and A.L. Nichols, *Critical conditions for impact-and shock-induced hot spots in solid explosives.* The Journal of Physical Chemistry, 1996. **100**(14): p. 5794-5799.

39. Honodel, C., et al. *Shock initiation of TATB formulations*. in *Proceedings Seventh Symposium (International) on Detonation*. 1981.

40. James, H., *Critical energy criterion for the shock initiation of explosives by projectile impact.* Propellants, Explosives, Pyrotechnics, 1988. **13**(2): p. 35-41.

41. James, H., *Predicting the response of explosives to attack by high-density shaped-charge jets.* Journal of Energetic Materials, 1989. **7**(4-5): p. 243-264.

42. Cook, M., P. Haskins, and H. James. *Projectile impact initiation of explosive charges*. in *9th Symposium (International) on Detonation, Portland, OR*. 1989.

43. Welle, E., et al. *Microstructural effects on the ignition behavior of HMX*. in *Journal of Physics: Conference Series*. 2014. IOP Publishing.

44. Skidmore, C., et al. *Characterization of HMX particles in PBX 9501*. in *The tenth American Physical Society topical conference on shock compression of condensed matter*. 1998. AIP Publishing.

45. Nagtegaal, J.C., D.M. Parks, and J. Rice, *On numerically accurate finite element solutions in the fully plastic range.* Computer Methods in Applied Mechanics and Engineering, 1974. **4**(2): p. 153-177.

46. Mas, E., et al. *A viscoelastic model for PBX binders*. in *AIP Conference Proceedings*. 2002. IOP INSTITUTE OF PHYSICS PUBLISHING LTD.

47. Barua, A. and M. Zhou, *A Lagrangian framework for analyzing microstructural level response of polymer-bonded explosives.* Modelling and Simulation in Materials Science and Engineering, 2011. **19**(5): p. 055001.

48. Christensen, R.M., *Theory of Viscoelasticity: An Introduction*. 2nd ed. 1982, New York: Academic Press.

49. Kaliske, M. and H. Rothert, *Formulation and implementation of three-dimensional viscoelasticity at small and finite strains.* Computational Mechanics, 1997. **19**(3): p. 228-239.

50. Sewell, T.D., et al., *A molecular dynamics simulation study of elastic properties of HMX.* The Journal of chemical physics, 2003. **119**: p. 7417.

51. Zhou, M., A. Needleman, and R.J. Clifton, *Finite element simulations of shear localization in plate impact.* Journal of the Mechanics and Physics of Solids, 1994. **42**(3): p. 423-458.

52. Povirk, G., S. Nutt, and A. Needleman, *Continuum modelling of residual stresses in metal-matrix composites.* Residual Stresses in Composites: Measurement, Modeling & Effects on Thermo-Mechanical Behavior, 1993: p. 3-23.

53. Barenblatt, G.I., *Equilibrium cracks formed during brittle fracture rectilinear cracks in plane plates.* Journal of Applied Mathematics and Mechanics, 1959. **23**(4): p. 1009-1029.

54. Dugdale, D.S., *Yielding of steel sheets containing slits.* Journal of the Mechanics and Physics of Solids, 1960. **8**(2): p. 100-104.

55. Rice, J.R., *A path independent integral and the approximate analysis of strain concentration by notches and cracks.* Journal of Applied Mechanics, 1968. **35**(2): p. 379-386.

56. Needleman, A., *Micromechanical modelling of interfacial decohesion.* Ultramicroscopy, 1992. **40**(3): p. 203-214.

57. Luthy, H., A. Miller, and O. Sherby, *The stress and temperature dependence of steady-state flow at intermediate temperatures for pure polycrystalline aluminum.* Acta Metallurgica, 1980. **28**(2): p. 169-178.

58. Young, L.J. and R.G. Easterling, *Estimation of extreme quantiles based on sensitivity tests: a comparative study.* Technometrics, 1994. **36**(1): p. 48-60.

59. Neyer, B.T., *AD-Optimality-Based Sensitivity Test.* Technometrics, 1994. **36**(1): p. 61-70.

60. Lee, W.-S., et al., *The strain rate and temperature dependence of the dynamic impact properties of 7075 aluminum alloy.* Journal of Materials Processing Technology, 2000. **100**(1): p. 116-122.

61. Camacho, G.T. and M. Ortiz, *Computational modelling of impact damage in brittle materials.* International Journal of Solids and Structures, 1996. **33**(20-22): p. 2899-2938.

62. Camanho, P. and C.G. Davila, *Mixed-Mode Decohesion Finite Elements for the Simulation of Delamination in Composite Materials*, 2002.

63. Minnaar, K. and M. Zhou. *Characterization of impact in composite laminates*. 2001. Conference.

64. Barua, A., Y. Horie, and M. Zhou, *Microstructural level response of HMX–Estane polymer-bonded explosive under effects of transient stress waves.* Proceedings of the Royal Society A: Mathematical, Physical and Engineering Science, 2012. **468**(2147): p. 3725-3744.

65. Zhai, J., V. Tomar, and M. Zhou, *Micromechanical Simulation of Dynamic Fracture Using the Cohesive Finite Element Method.* Journal of Engineering Materials and Technology, 2004. **126**(2): p. 179-191.

66. Tomar, V., J. Zhai, and M. Zhou, *Bounds for element size in a variable stiffness cohesive finite element model.* International Journal for Numerical Methods in Engineering, 2004. **61**(11): p. 1894-1920.

67. Chidester, S., L. Green, and C. Lee, *A frictional work predictive method for the initiation of solid high explosives from low-pressure impacts*, 1993, Lawrence Livermore National Lab., CA (United States).

68. Dickson, P., et al. *Frictional heating and ignition of energetic materials*. in *AIP Conference Proceedings*. 2006.

69. Dick, J., *Measurement of the shock initiation sensitivity of low density HMX.* Combustion and Flame, 1983. **54**(1): p. 121-129.

70. Barua, A., et al., *Prediction of probabilistic ignition behavior of polymer-bonded explosives from microstructural stochasticity.* Journal of Applied Physics, 2013. **113**(18): p. 184907-184907-20.

71. Nichols III, A.L. and C.M. Tarver. *A statistical hot spot reactive flow model for shock initiation and detonation of solid high explosives*. in *Twelfth International Symposium on Detonation, Office of Naval Research, San Diego, CA*. 2002.

72. Cooper, S., D. Benson, and V. Nesterenko, *A numerical exploration of the role of void geometry on void collapse and hot spot formation in ductile materials.* International Journal of Plasticity, 2000. **16**(5): p. 525-540.

73. Cawkwell, M., et al., *Shock-induced shear bands in an energetic molecular crystal: Application of shock-front absorbing boundary conditions to molecular dynamics simulations.* Physical Review B, 2008. **78**(1): p. 014107.

74. Czerski, H. and W. Proud, *Relationship between the morphology of granular cyclotrimethylene-trinitramine and its shock sensitivity.* Journal of Applied Physics, 2007. **102**(11): p. 113515-113515-8.

75. Bedrov, D., G.D. Smith, and T.D. Sewell, *Temperature-dependent shear viscosity coefficient of octahydro-1, 3, 5, 7-tetranitro-1, 3, 5, 7-tetrazocine (HMX): A molecular dynamics simulation study.* The Journal of chemical physics, 2000. **112**: p. 7203.

76. Sorescu, D.C., B.M. Rice, and D.L. Thompson, *Theoretical studies of the hydrostatic compression of RDX, HMX, HNIW, and PETN crystals.* The Journal of Physical Chemistry B, 1999. **103**(32): p. 6783-6790.

77. Sewell, T.D., *Monte Carlo calculations of the hydrostatic compression of hexahydro-1, 3, 5-trinitro-1, 3, 5-triazine and β-octahydro-1, 3, 5, 7-tetranitro-1, 3, 5, 7-tetrazocine.* Journal of Applied Physics, 1998. **83**(8): p. 4142-4145.

78. Sorescu, D.C., B.M. Rice, and D.L. Thompson, *Isothermal-isobaric molecular dynamics simulations of 1, 3, 5, 7-tetranitro-1, 3, 5, 7-tetraazacyclooctane (HMX) crystals.* The Journal of Physical Chemistry B, 1998. **102**(35): p. 6692-6695.

79. Lewis, J.P., et al., *Electronic structure calculation of the structures and energies of the three pure polymorphic forms of crystalline HMX.* The Journal of Physical Chemistry B, 2000. **104**(5): p. 1009-1013.

80. Conroy, M., et al., *First-principles anisotropic constitutive relationships in β-cyclotetramethylene tetranitramine (β-HMX).* Journal of Applied Physics, 2008. **104**(5): p. 053506-053506-6.

81. Byrd, E.F.C. and B.M. Rice, *Ab Initio Study of Compressed 1, 3, 5, 7-Tetranitro-1, 3, 5, 7-tetraazacyclooctane (HMX), Cyclotrimethylenetrinitramine (RDX), 2, 4, 6, 8, 10, 12-Hexanitrohexaazaisowurzitane (CL-20), 2, 4, 6-Trinitro-1, 3, 5-benzenetriamine (TATB), and Pentaerythritol Tetranitrate (PETN).* The Journal of Physical Chemistry C, 2007. **111**(6): p. 2787-2796.

82. Byrd, E.F.C., G.E. Scuseria, and C.F. Chabalowski, *An ab initio study of solid nitromethane, HMX, RDX, and CL20: Successes and failures of DFT.* The Journal of Physical Chemistry B, 2004. **108**(35): p. 13100-13106.

83. Dan, L., et al., *High-pressure behaviour of β-HMX crystal studied by DFT-LDA.* Chinese Physics Letters, 2008. **25**(3): p. 899.

84. Zhu, W., et al., *First-principles study of the four polymorphs of crystalline octahydro-1, 3, 5, 7-tetranitro-1, 3, 5, 7-tetrazocine.* The Journal of Physical Chemistry B, 2007. **111**(44): p. 12715-12722.

85. Zamiri, A.R. and S. De, *Modeling the Anisotropic Deformation Response of β-HMX Molecular Crystals.* Propellants, Explosives, Pyrotechnics, 2011. **36**(3): p. 247-251.

86. Zamiri, A.R. and S. De, *Deformation distribution maps of β-HMX molecular crystals.* Journal of Physics D: Applied Physics, 2010. **43**(3): p. 035404.

87. Wu, Y.Q. and F.L. Huang, *Orientation-dependent Constitutive Model with Nonlinear Elasticity for Shocked β-HMX Single Crystal.* Int. J. Nonlinear Sci. Numer. Simul., 2012. **13**(1): p. 13-24.

88. Yan-Qing, W. and H. Feng-Lei, *Thermal mechanical anisotropic constitutive model and numerical simulations for shocked β-HMX single crystals.* European Journal of Mechanics-A/Solids, 2012.

89. Cady, H.H. and L.C. Smith, *Studies on the Polymorphs of HMX*. 1962: Los Alamos Scientific Laboratory of the University of California.

90. Choi, C.S. and H.P. Boutin, *A study of the crystal structure of-cyclotetramethylene tetranitramine by neutron diffraction.* Acta Crystallographica Section B: Structural Crystallography and Crystal Chemistry, 1970. **26**(9): p. 1235-1240.

91. Soulard, L., et al. *Meso-scale analysis of deformation wave heating in metalized solid explosive*. in *EPJ Web of Conferences*. 2010. EDP Sciences.

92. Barua, A., Y. Horie, and M. Zhou, *Energy localization in HMX-Estane polymer-bonded explosives during impact loading.* Journal of Applied Physics, 2012. **111**(5): p. 054902-054902-11.

93. Bardenhagen, S. and J. Brackbill, *Dynamic stress bridging in granular material.* Journal of Applied Physics, 1998. **83**(11): p. 5732-5740.

94. Bardenhagen, S.G., et al. *Coupling grain scale and bulk mechanical response for PBXs using numerical simulations of real microstructures*. in *SHOCK COMPRESSION OF CONDENSED MATTER-2005: Proceedings of the Conference of the American Physical Society Topical Group on Shock Compression of Condensed Matter*. 2006. AIP Publishing.

95. Kanjarla, A.K., P. Van Houtte, and L. Delannay, *Assessment of plastic heterogeneity in grain interaction models using crystal plasticity finite element method.* International Journal of Plasticity, 2010. **26**(8): p. 1220-1233.

96. Musienko, A., et al., *Three-dimensional finite element simulation of a polycrystalline copper specimen.* Acta materialia, 2007. **55**(12): p. 4121-4136.

97. Evers, L., et al., *Crystal plasticity model with enhanced hardening by geometrically necessary dislocation accumulation.* Journal of the Mechanics and Physics of Solids, 2002. **50**(11): p. 2403-2424.

98. Clayton, J. and D. McDowell, *A multiscale multiplicative decomposition for elastoplasticity of polycrystals.* International Journal of Plasticity, 2003. **19**(9): p. 1401-1444.

99. Bronkhorst, C., et al., *An experimental and numerical study of the localization behavior of tantalum and stainless steel.* International Journal of Plasticity, 2006. **22**(7): p. 1304-1335.

100. Bronkhorst, C.A., et al., *Modeling the microstructural evolution of metallic polycrystalline materials under localization conditions.* Journal of the Mechanics and Physics of Solids, 2007. **55**(11): p. 2351-2383.

101. Balasubramanian, S. and L. Anand, *Plasticity of initially textured hexagonal polycrystals at high homologous temperatures: application to titanium.* Acta materialia, 2002. **50**(1): p. 133-148.

102. Hasija, V., et al., *Deformation and creep modeling in polycrystalline Ti–6Al alloys.* Acta materialia, 2003. **51**(15): p. 4533-4549.

103. Delannay, L., P.J. Jacques, and S.R. Kalidindi, *Finite element modeling of crystal plasticity with grains shaped as truncated octahedrons.* International Journal of Plasticity, 2006. **22**(10): p. 1879-1898.

104. Rimoli, J.J., E. Gürses, and M. Ortiz, *Shock-induced subgrain microstructures as possible homogenous sources of hot spots and initiation sites in energetic polycrystals.* Physical Review B, 2010. **81**(1): p. 014112.

105. Rimoli, J. and M. Ortiz, *A duality-based method for generating geometric representations of polycrystals.* International Journal for Numerical Methods in Engineering, 2011. **86**(9): p. 1069-1081.

106. Maggi, F., et al., *Nature of packs used in propellant modeling.* Physical Review E, 2008. **77**(4): p. 046107.

107. Stafford, D.S. and T.L. Jackson, *Using level sets for creating virtual random packs of non-spherical convex shapes.* Journal of Computational Physics, 2010. **229**(9): p. 3295-3315.

108. Herrmann, M., W. Engel, and N. Eisenreich, *Thermal analysis of the phases of HMX using X-ray diffraction.* Zeitschrift für Kristallographie, 1993. **204**(Part-1): p. 121-128.

109. Brill, T. and R. Karpowicz, *Solid phase transition kinetics. The role of intermolecular forces in the condensed-phase decomposition of octahydro-1, 3, 5, 7-tetranitro-1, 3, 5, 7-tetrazocine.* The Journal of Physical Chemistry, 1982. **86**(21): p. 4260-4265.

110. Henson, B., et al., *Dynamic measurement of the HMX β-δ phase transition by second harmonic generation.* Physical review letters, 1999. **82**(6): p. 1213-1216.

111. Karpowicz, R. and T. Brill, *The beta to delta transformation of HMX- Its thermal analysis and relationship to propellants.* AIAA Journal, 1982. **20**: p. 1586-1591.

112. Sheen, D., et al., *An investigation of mechanically induced lattice defects in energetic materials.* Office of Naval Research Final report, 1993(00014): p. 53.

113. Zaug, J., *Elastic Constants of Β-HMX and Tantalum, Equation of State of Supercritical Fluids and Fluid Mixtures and Thermal Transport Determinations.* Proceedings 11th Detonation Symposium, 1998.

114. Stevens, L.L. and C.J. Eckhardt, *The elastic constants and related properties of β-HMX determined by Brillouin scattering.* The Journal of chemical physics, 2005. **122**: p. 174701.

115. Vial, J., et al., *Numerical and experimental study of the plasticity of HMX during a reverse edge-on impact test.* Modelling and Simulation in Materials Science and Engineering, 2013. **21**(4): p. 045006.

116. Cuitino, A.M. and M. Ortiz, *Computational modelling of single crystals.* Modelling and Simulation in Materials Science and Engineering, 1993. **1**(3): p. 225.

117. Marsh, S.P., *LASL shock Hugoniot data*. Vol. 5. 1980: Univ of California Press.

118. Barua, A., et al., *Ignition criterion for heterogeneous energetic materials based on hotspot size-temperature threshold.* Journal of Applied Physics, 2013. **113**(6): p. 064906-064906-22.

119. Gilbert, J. and K.A. Gonthier. *Meso-scale computation of uniaxial waves in granular explosive-analysis of deformation induced ignition*. in *50th AIAA Aerospace Sciences Meeting Including the New Horizons Forum and Aerospace Exposition*. 2012.

120. Gilbert, J., S. Chakravarthy, and K.A. Gonthier, *Computational analysis of hot-spot formation by quasi-steady deformation waves in porous explosive.* Journal of Applied Physics, 2013. **113**(19): p. -.

121. Chakravarthy, S., K.A. Gonthier, and R. Panchadhara, *Analysis of mesoscale heating by piston supported waves in granular metalized explosive.* Modelling and Simulation in Materials Science and Engineering, 2013. **21**(5): p. 055016.

122. Keicher, T., et al., *Influence of aluminium/ammonium perchlorate on the performance of underwater explosives.* Propellants, Explosives, Pyrotechnics, 1999. **24**(3): p. 140-143.

123. Stromose, E. and S. Eriksen, *Performance of high explosives in underwater application, part 2: aluminised explosives.* Propell Explos Pyrotech, 1990. **15**: p. 52-53.

124. Wise, L.S., *EFFECT OF ALUMINUM ON THE RATE OF DETONATION OF TNT*, 1945, DTIC Document.

125. Gogulya, M., et al. *Detonation waves in HMX/Al mixtures (pressure and temperature measurements)*. in *Proc. of the 11th Symp.(Int.) on Detonation*. 1998.